

学位論文

Observation of gamma ray storms at the earth's surface
related to the thunderclouds and a study of their properties

(雷雲に関連した地表における γ 線増大現象の観測とその特性の研究)

平成 26 年 3 月 博士(理学) 申請

東京大学大学院理学系研究科
物理学専攻

黒田 康浩

Abstract

We observed three γ -ray bursts related to thunder clouds using the prototype of anti-neutrino detector PANDA deployed outside at Ohi Power Station. The maximum rate of the events which deposited the energy higher than 3 MeV on the detector was $(5.5 \pm 0.1 \text{ (stat.)}) \times 10^2/\text{sec}$.

To investigate the mechanism of the bursts, we made Monte Carlo simulations. We calculated bremsstrahlung γ -ray spectra from almost mono-energetic electrons projected vertically downward from the sky and investigated the detector response.

The results of the simulations indicated that the spectra of bremsstrahlung γ -rays by electrons projected from O(100) m above in the sky well describe the observed energy spectra of the bursts. It is supposed that secondary cosmic-ray electrons, which act as seed, were accelerated in electric field of thunderclouds and amplified by relativistic runaway electron avalanche.

The arrival direction of the γ -rays were also investigated by the position information of each energy deposit and Compton scattering-angle calculation. We found that γ -rays of the bursts entered into the detector from the sky and from the direction close to the zenith. The arrival direction stayed constant during the burst within our detector resolution.

We estimated the electron amplification factor in the electric field in the thunder clouds from our observation results. The estimated amplification factors are 7.5×10^2 , 8.0×10^2 and 3.5×10^2 for the three bursts.

In addition, taking advantage of the ability to detect the neutron of the prototype detector, we searched for the neutron bursts corresponding to the γ -ray bursts. Consequently, the time correlated events, the feature of which is consistent with the neutron absorption in the Gadolinium, were detected at the maximum rate of $\sim 14 \pm 5 \text{ (stat.)}/\text{sec}$.

Contents

1	Introduction	13
1.1	Energetic radiation related to thunderclouds	13
1.2	Electrical particle acceleration in thunderclouds	14
1.3	Neutron production by lightning	16
1.4	Detection with prototype PANDA detector	17
2	Recent distinct results of the observations of the γ-rays associated with thunderclouds	19
2.1	GROWTH experiment	19
2.2	Detection of source migration	20
2.3	Comprehensive observation at Aragats Space-Environmental Centre	21
3	Design of the detector and data acquisition	23
3.1	Plastic Anti-Neutrino Detector Array (PANDA)	23
3.2	Reactor monitoring and safeguards using anti-neutrino detectors	23
3.3	Electron anti-neutrino detection by inverse-beta decay	25
3.4	Design of the detector	25
3.5	Module	25
3.6	Data acquisition system	28
3.7	Transportation and Deployment	32
3.8	Energy calibration	32
3.9	Data storage and detector monitoring system	41
4	Radiation enhancements associated with thunderstorms	43
4.1	Unexpected event-rate increase in PANDA36 data	43
4.2	Source of the radiation burst	47
4.3	Energy of the bursts	48
4.4	Variation of the hit multiplicities	52
4.5	Monte Carlo analysis of γ -rays emitted by accelerated electrons	52
4.6	Arrival direction of γ -rays	62
4.6.1	Arrival direction analysis by maximum energy-deposit position	62
4.6.2	Arrival direction analysis using Compton scattering angle	68
4.7	Neutron event-rate increase	82
5	Discussion about the model of γ-ray burst related to the thunder clouds	87
6	Conclusion	91
7	Acknowledgments	93

List of Figures

1.1	The stopping power of an energetic electron in the air in the standard conditions. The blue dotted line shows the stopping power by ionization, the pink line shows the stopping power by bremsstrahlung and the red line is summation of them. In addition, electric force on electrons by 300 kV/m electric field is plotted by black dotted line.	15
1.2	Relation between energy and acceleration length of the electrons injected into the 300 kV/m electric field with kinetic energy $\sim T_1$	16
1.3	Relation between the energy of the electron accelerated in 300 kV/m electric field and energy loss of electron via bremsstrahlung. Two pink lines shows the maximum attainable energy with 200 m and 500 m acceleration.	16
2.1	Schematic views of the one of the GROWTH detectors (cited from ref. [22]) . . .	20
2.2	Photon energy spectrum observed via GROWTH detectors (cited from ref. [22]) .	20
2.3	The time differences of the radiation peak of each detector (cited from ref. [25]) .	21
2.4	ArNM enhancement simultaneous to the SEVAN detector (cited from ref. [15]) .	22
3.1	Number of anti-neutrino emitted by a fission from a reactor core (^{235}U , ^{239}Pu ; left ordinate), the cross section of the inverse beta decay (right ordinate), and the expected energy spectrum of the anti-neutrinos detected by the inverse beta decay (arbitrary unit).	24
3.2	The concept design of the PANDA anti-neutrino detector. The approximate total target size is 1 m^3	26
3.3	Lesser PANDA: A prototype of the PANDA detector, which consists of 16 modules	26
3.4	PANDA36: The prototype of the PANDA detector, which consists of 36 modules	27
3.5	PANDA64: The prototype of the PANDA detector, which consists of 64 modules	27
3.6	Structure of the PANDA module	29
3.7	Light propagation model in the plastic scintillator bar	29
3.8	Logarithm of the ratio of PMT charge measured at one end to charge at the other end of the module vs. source position. The dashed curve is a two-parameter (p and l in equation (3.6)) fit of the ratio predicted by the light attenuation model.	29
3.9	Simplified block diagram of the data acquisition system for Lesser PANDA . . .	30
3.10	Simplified block diagram of the data acquisition system for PANDA36	31
3.11	Picture of the divider	31
3.12	Circuit of the divider	31
3.13	PANDA36 and the DAQ system loaded on the van	33
3.14	The van with PANDA36 was parked just next to the reactor building.	33
3.15	The deployed position of the PANDA36 detector by Ohi Nuclear Power Plant Unit 2 reactor	33
3.16	Schematic view of the setup for the calibration of each module (PANDA64; top view)	35
3.17	Schematic view of the setup for the calibration of each module (PANDA64; side view)	35

3.18	An example (module no.1 of the PANDA64 detector) of energy spectrum in one module obtained with ^{60}Co calibration source after background subtraction, compared with the Geant4 simulation (dashed line). For both simulated and measured spectra, the error bars represent the statistical error.	36
3.19	Same as Figure 3.18but for module no.2 of the PANDA64 detector	37
3.20	Energy resolution of module 1 in the case that γ -ray deposited energy at the center of the module	37
3.21	Energy resolution of module 1 in the case that γ -ray deposited energy at 300 mm away from the center of the module	37
3.22	Energy resolution of module 2 in the case that γ -ray deposited energy at the center of the module	38
3.23	Energy resolution of module 2 in the case that γ -ray deposited energy at 300 mm away from the center of the module	38
3.24	Longitudinal position resolution of module 1 in the case that γ -ray deposited energy at the center of the module	38
3.25	Longitudinal position resolution of module 1 in the case that γ -ray deposited energy at 300 mm away from the center of the module	38
3.26	Longitudinal position resolution of module 2 in the case that γ -ray deposited energy at the center of the module	38
3.27	Longitudinal position resolution of module 2 in the case that γ -ray deposited energy at 300 mm away from the center of the module	38
3.28	Schematic diagram of the data storage and detector monitoring system	41
3.29	Temperature and humidity monitoring (example from PANDA36 data)	42
3.30	Time variation of the pedestal (example from PANDA36 data)	42
4.1	Simulated total energy deposit (E_{total}) spectrum in the PANDA36 detector of 5 MeV γ -rays isotropically incident on the detector. Trigger logic described in Section 3.6was considered.	44
4.2	Distribution of the rate of the event by PANDA36 which have $E_{\text{tot}} > 4 \text{ MeV}$. Blue dotted line is the threshold of the detection of high event rate intervals. . .	44
4.3	Temporal variation in the event rate of the burst event of 2011/12/25	45
4.4	Temporal variation in the event rate of the burst event of 2012/01/02	46
4.5	Temporal variation in the event rate of the burst event of 2012/01/05	46
4.6	Thunder Nowcast of 05:00 and 05:10, December 25th, 2011 JST. The red cross shows the location of Ohi Power Station, which stand at the southeastern coastal area of the Japan Sea. Colors on the map show the degree of the thunder activities. . .	48
4.7	Thunder Nowcast of 09:10 and 09:20, January 2th, 2012 JST.	48
4.8	Thunder Nowcast of 06:40 and 06:50, January 5th, 2012 JST.	49
4.9	Thunder Nowcast of 19:50 and 20:00, January 4th, 2012 JST. At this time, the thunder activity level above the detector was two, though increase in event rate was not observed by the PANDA36 detector as shown in Figure 4.10.	49
4.10	Temporal variation in the event rate from 19:46:20, January 4th, 2012, when the thunder clouds are assumed to be above the detector	50
4.11	Event rate distribution of $E_{\text{total}} > 4 \text{ MeV}$ when there were no bursts recorded by PANDA36	50
4.12	burst-20111225: (left) E_{total} spectrum of the burst period and the background period. (right) E_{total} spectrum of the burst period with background subtraction. The error bars show the statistical errors.	51
4.13	burst-20120102: Same as Figure 4.12	51
4.14	burst-20120105: Same as Figure 4.12	51

4.15	The event rate for each multiplicity during burst-20111225 (red plot) and corresponding background period (blue dotted line). The rate of the events with only 1 fired module is suppressed to zero because of the trigger condition of the PANDA36 detector.	53
4.16	burst-20120102: Same as Figure 4.16	53
4.17	burst-20120105: Same as Figure 4.16	53
4.18	In the first simulation, electrons are shot from height h with energy E in a $2\text{ km} \times 2\text{ km} \times 2\text{ km}$ space filled with air.	54
4.19	Number of bremsstrahlung photons which reached the ground for each height and energy of the source electrons calculated by the Monte Carlo method	54
4.20	Simulated spectrum of bremsstrahlung γ -rays emitted by 10 MeV (left), 20 MeV (middle) and 30 MeV (right) electrons shot from 100 (bottom), 600 m (middle) and 1100 m (top)	55
4.21	Simulated position distribution of bremsstrahlung γ -rays emitted by 10 MeV (left), 20 MeV (middle) and 30 MeV (right) electrons shot from 100 (bottom), 600 m (middle) and 1100 m (top). The distances of landing point of photon from point just below the projection.	55
4.22	In the second simulation, γ -rays are shot from random point in a circle above the detector. The circle is large enough to cover whole detector.	56
4.23	burst-20111225: χ^2/dof calculated by comparing observed data and bremsstrahlung photon emitted by electron shot from the sky	57
4.24	burst-20120102: Same as Figure 4.23	57
4.25	burst-20120105: Same as Figure 4.23	57
4.26	Simulated spectrum of E_{total} by electron shot from 1100 m with 16 MeV, which matches the burst-20111225 spectrum the best. For both simulated and measured spectra, the error bars show the statistical error.	58
4.27	Same as Figure 4.26, but for E_{total} by electron shot from 1100 m with 16 MeV, which matches the burst-20120102 spectrum the best	58
4.28	Same as Figure 4.26, but for E_{total} by electron shot from 400 m with 16 MeV, which matches the burst-20120102 spectrum the best	58
4.29	Simulated spectrum of E_{total} from electrons shot from 900 m with energy spectrum which matches the burst-20111225 spectrum the best. The spectrum of the electron at the shot height was divided into four bins (17 MeV, 23 MeV, 29 MeV and 35 MeV). For both simulated and measured spectra, the error bars show the statistical error	60
4.30	The same plot as Figure 4.29 but for burst-20120102 (electrons were shot from 500 m height)	60
4.31	The same plot as Figure 4.29 but for burst-20120105 (electron were shot from 100 m height)	60
4.32	(left) Estimated electron spectrum at the projection height with statistical errors (right) Fitted energy spectra showing the fraction of the contribution of each electron energy bin by colors	61
4.33	The same plot as Figure 4.32 but for burst-20120102	61
4.34	The same plot as Figure 4.32 but for burst-20120105	61
4.35	Mean free path of γ -ray in the plastic scintillator [62]	62
4.36	Simulated $E_{1\text{st}}$ distribution by γ -rays isotropically incident on the detector. Simulated energy spectrum of bremsstrahlung γ -rays of burst-20111225 calculated in Section 4.5 was used.	63
4.37	Same as Figure 4.36, but used γ -ray spectrum was bremsstrahlung spectrum of burst-20120102	63

4.38	Same as Figure 4.36, but used γ -ray spectrum was bremsstrahlung spectrum of burst-20120105	63
4.39	burst-20111225: E_{1st} distribution	64
4.40	burst-20120102: E_{1st} distribution	64
4.41	burst-20120105: E_{1st} distribution	64
4.42	Temporal variation of E_{1st} distribution around burst-20111225	65
4.43	Temporal variation of E_{1st} distribution around burst-20120102	66
4.44	Temporal variation of E_{1st} distribution around burst-20120105	67
4.45	Compton scattering	68
4.46	The cross-sections of Compton scattering for unpolarized photons	68
4.47	Restrict γ -ray incoming direction using multiple Compton cones	69
4.48	An example of the effect of γ -ray escape to the $\cos \theta'$ calculation when incident γ -ray energy is 5 MeV. We assume E_{total} to be the energy of the incident γ -ray and the red solid line shows the cases with no γ -ray escape (correct value), and the blue dotted line and pink line show the case when a 100 keV γ -ray has escaped and when a 300 keV γ -ray has escaped, respectively. The effect of γ -ray escape is large near the Compton edge.	70
4.49	The coordinate used for the arrival direction analysis	72
4.50	Simulated arrival direction distribution by γ -rays isotropically incident on the detectors. The energy spectrum of bremsstrahlung γ -rays of burst-20111225 which is calculated in Section 4.5 was used.	73
4.51	Same as Figure 4.50, but used γ -ray spectrum was the spectrum of bremsstrahlung γ -rays of burst-20120102	73
4.52	Same as Figure 4.50, but used γ -ray spectrum was the spectrum of bremsstrahlung γ -rays of burst-20120105	73
4.53	The result of arrival direction analysis to the simulated detector response to the γ -rays incoming from $(\theta, \phi) = (\pi/2, \pi/6)$	74
4.54	Same as Figure 4.53 but for γ -rays incoming from $(\theta, \phi) = (\pi/2, \pi/3)$	74
4.55	Same as Figure 4.53 but for γ -rays incoming from $(\theta, \phi) = (\pi/2, \pi/2)$	74
4.56	Same as Figure 4.53 but for γ -rays incoming from $(\theta, \phi) = (\pi/6, \pi/2)$	75
4.57	Same as Figure 4.53 but for γ -rays incoming from $(\theta, \phi) = (\pi/3, \pi/2)$	75
4.58	burst-20111225: arrival direction distribution of γ -rays. The coordinate is defined in Figure 4.49 and only the upper hemisphere of the detector is shown ($\cos \theta = 0, \phi = 1.57$ is vertically upward of the detector).	76
4.59	burst-20120102: arrival direction distribution of γ -rays	76
4.60	burst-20110105: arrival direction distribution of γ -rays	76
4.61	burst-20111225: ϕ distribution of arrival direction of incoming γ -rays during the burst. The error bars represent the statistical error.	77
4.62	burst-20111225: $\cos \theta$ distribution of arrival direction of incoming γ -rays during the burst. The error bars represent the statistical error.	77
4.63	burst-20120102: Same as Figure 4.61	77
4.64	burst-20120102: Same as Figure 4.62	77
4.65	burst-20120105: Same as Figure 4.61	77
4.66	burst-20120105: Same as Figure 4.62	77
4.67	Temporal variation of the arrival direction distribution around burst-20111225	78
4.68	Temporal variation of the arrival direction distribution around burst-20120102	79
4.69	Temporal variation of the arrival direction distribution around burst-20120105	80
4.70	Temporal variation of the ϕ distribution around burst-20111225	81
4.71	Temporal variation of the $\cos \theta$ distribution around burst-20111225	81
4.72	Temporal variation of the ϕ distribution around burst-20120102	81
4.73	Temporal variation of the $\cos \theta$ distribution around burst-20120102	81

4.74	Temporal variation of the ϕ distribution around burst-20120105	81
4.75	Temporal variation of the $\cos \theta$ distribution around burst-20120105	81
4.76	Observed distribution of intervals between triggered events and simulated intervals assuming that each event has no temporal correlation to each other. (left) The distribution shown in wide range (0-100 msec). (right) small region is magnified (0-200 μ sec).	83
4.77	burst-20120102: Same as Figure 4.76	83
4.78	burst-20120105: Same as Figure 4.76	83
4.79	Temporal variation of the number of correlated events in the burst-20111225 . .	84
4.80	Temporal variation of the number of correlated events in the burst-20120102 . .	84
4.81	Temporal variation of the number of correlated events in the burst-20120105 . .	85
4.82	The E_{total} spectra of the prompt event (left) and the delayed event (right) of the correlated event in burst-20120105. The error bars represent the statistical error. Solid lines represent the spectra by 10 MeV neutrons isotropically incident on the detector calculated by the Geant4 simulation. The simulation histograms were normalized to the total number of the real data.	85
5.1	Estimated electron amplification factors for each electron projection heights. Assuming that the energy of the projected electrons was monochromatic (16 MeV). Error bars are only statistical.	89
5.2	Same as Figure 5.1but for burst-20120102	89
5.3	Same as Figure 5.1but for burst-20120105	89

List of Tables

1.1	PANDA-prototype experiments	17
3.1	Coefficient parameters for anti-neutrino flux[56]	24
3.2	Parameters determined by the calibration procedure (PANDA36)	39
3.3	Parameters determined by the calibration procedure (PANDA36)	40
4.1	Three radiation burst events. The peak event rate for each burst with the statistical errors are shown.	44
4.2	The meanings of thunder activity levels	47
4.3	List of the burst periods	49
4.4	Fraction of events whose first and second scatterings occur in one module calculated by Monte Carlo method. The errors are only statistical.	70
4.5	The selection criteria of the events for $\cos \theta'$ calculation	70
4.6	Selection criteria for neutrons	82
5.1	Ratio of bremsstrahlung photons which reached the ground with the energy higher than 3 MeV calculated by the Monte Carlo simulation. The errors are statistical.	87
5.2	The estimated electron flux of the three bursts. The errors are statistical.	88
6.1	Features of the three γ -ray bursts	92

Chapter 1

Introduction

1.1 Energetic radiation related to thunderclouds

In the early 1920's, C.T.R. Wilson suggested that strong electric fields in thunderclouds might accelerate free electrons naturally present in the atmosphere to high energies thereby generating bremsstrahlung as the electrons are slowed by collisions with air molecules[1]. Since then, radiation associated with thunderstorms attracted the interest as natural particle-acceleration process and many experiments and observations have been attempted to detect these radiations in various environments.

In 1966, at the University of Arizona's lighting research facility placed atop Mount Lemon (altitude 2800 m), an increase in the cosmic-ray component was found to accompany thunderstorms[2]. Typical count increase and its duration was 5% and roughly 10 minutes respectively. The EAS-TOP array at Campo Imperatore (National Gran Sasso Laboratories; altitude 2005 m) observed thunderstorms affect the counting rate of air showers[3, 4]. Excesses in the air shower count rate lasted ~ 10 – 20 minutes with maximum amplitudes of 10–15% [5]. Observation with high-mountain detectors were also made at the Mount Norikura Cosmic Ray Observatory (altitude 2770 m)[6, 7, 8], the top of Mount Fuji (altitude 3776 m)[9], the Lebedev Physics Institute mountain cosmic ray station which is situated on a pass in Tien-Shan mountains at a height of 3340 m above sea level[10, 11], summit of South Baldy Peak (altitude 3288 m) in the Magdalena mountains[12, 13], the Carpet air shower array (Baksan Valley, North Caucasus; altitude 1700 m)[14], Aragats Space Environmental Center (3200 m altitude)[15, 16, 17] and the Yangbajing Cosmic Ray Observatory (altitude 4300 m) in Tibet [18].

Winter thunderclouds, which frequently visit the southeastern coastal area of the Japan Sea were reported to be related to γ -ray flux on low ground. Japanese groups found that a radiation monitoring post in nuclear power plants signaled an increase of environmental γ -ray dose which seemed to originate from winter lightning activity[19][20]. The Gamma-Ray Observation of Winter Thunderclouds (GROWTH) experiment detected γ -ray emissions lasting for ~ 40 sec prior to lightning discharges [21, 22, 23]. The observation provided the clear evidence that strong electric fields in thunderclouds can continuously accelerate electrons beyond 10 MeV. GROWTH experiment also confirmed that the emission area was considerably smaller for γ -rays with energy over 10 MeV than lower-energy γ -rays [24]. Recently, an experiment at Fugen of the Japan Atomic Energy Agency (JAEA) detected the source of the radiation in thundercloud moving across locations [25].

Detecting radiation inside thunderclouds were also attempted. Significant radiation flux increases were detected for time intervals of several seconds, which returned to background levels within 0.1 seconds of a lightning flash initiation have been observed with detectors on-board an airplane [26, 27]. As well, the experiment using a free balloon detected the radiation increase and suggested that the production mechanism for the γ -rays were related to the storm electric field and not necessarily to lightning discharge processes [28, 29].

Surprisingly, upward γ -rays from the earth's atmosphere were observed by the orbiting gamma observatories at 400-600 km above the Earth's surface. Very short (a few milliseconds) bursts of high-energy γ -rays called Terrestrial Gamma Flashes (TGF) were discovered with the Burst and Transit Source Experiment (BATSE) instrument on the Compton Gamma Ray Observatory[30]. The spectrum of TGFs was well explained by bremsstrahlung emission from electrons accelerated to high energies by the relativistic runaway electron avalanche (RREA) process[31]. The TGFs were also observed with the Reuven Ramaty High Energy Solar Spectroscopic Imager (RHESSI)[32, 33], Astro-rivelatore Gamma a Immagini Leggero (AGILE)[34, 35] and the Gamma-ray Burst Monitor (GBM) on the Fermi Gamma-ray Space Telescope[36, 37]. These results strongly confirmed the correlations of TGFs with thunderstorms.

There were two types of emissions observed: ones last for about tens of minutes and do not appear to clearly coincide with lightning processes, and the others have typical duration of tens of milliseconds or less and often associated with lightning discharges. Former long-duration bursts have remained less understood than short bursts. There is no adequate explanation for radiation process keeps operating for such a long duration. To investigate the phenomenon, more samples with high statistics are needed.

1.2 Electrical particle acceleration in thunderclouds

γ -ray dose enhancements as we mentioned in the previous section are interpreted to be due to bremsstrahlung from electrons accelerated in the electric field in the thunderclouds. Gurevich *et al.* [31, 38] developed the runaway electron model to explain the electron acceleration in the moderate electric field of the thunderclouds. The electrons can cause an avalanche multiplication process called relativistic runaway electron avalanche (RREA). As the minimum electric field required for RREA is an order of magnitude lower than the conventional breakdown thresholds, RREA has been suggested as the background mechanism for lightning initiation, TGFs and prolonged γ -ray enhancement under the thunderclouds.

The stopping power of an energetic electron in the air is described by following equation [39]:

$$\left| -\frac{dE_e}{dx} \right|_{\text{ion}} = \rho \frac{1}{2} K \frac{Z}{A} \frac{1}{\beta^2} \left[\ln \frac{m_e c^2 \beta^2 \gamma^2 \{m_e c^2 (\gamma - 1)/2\}}{I^2} + (1 - \beta^2) - \frac{2\gamma - 1}{\gamma^2} \ln 2 + \frac{1}{8} \left(\frac{\gamma - 1}{\gamma} \right)^2 - \delta \right]. \quad (1.1)$$

Here $\beta = v_e/c$, $\gamma = 1/\sqrt{1 - \beta^2}$, $K = 4\pi N_A r_e^2 m_e c^2$, v_e is the velocity of the electron, c is the light speed, N_A is Avogadro's number, $r_e = e^2/4\pi\epsilon_0 m_e c^2$ is the classical electron radius, Z is the mean atomic number of the air, A is the mean atomic mass, m_e is the electron mass, I is the mean excitation energy of the air and δ is the density effect correction to the ionization energy loss.

At high energies, energy loss by bremsstrahlung becomes important. The approximate cross section is [39]

$$\frac{d\sigma}{dk} = \frac{A}{X_0 N_A k} \left(\frac{4}{3} - \frac{4}{3} y + y^2 \right), \quad (1.2)$$

where X_0 is the radiation length of the air and $y = k/E_e$ is the fraction of the electron's energy transferred to the radiated photon. The stopping power is calculated as

$$\left| \frac{dE_e}{dx} \right|_{\text{brems}} = \int_0^{E_e} k \frac{\rho N_A}{A} \frac{d\sigma}{dk} dk = \rho \frac{E_e}{X_0}. \quad (1.3)$$

Energy loss of electrons per unit path length by ionization and bremsstrahlung in the dry air under standard conditions (STP) is shown in Figure 1.1. In non-relativistic region, the

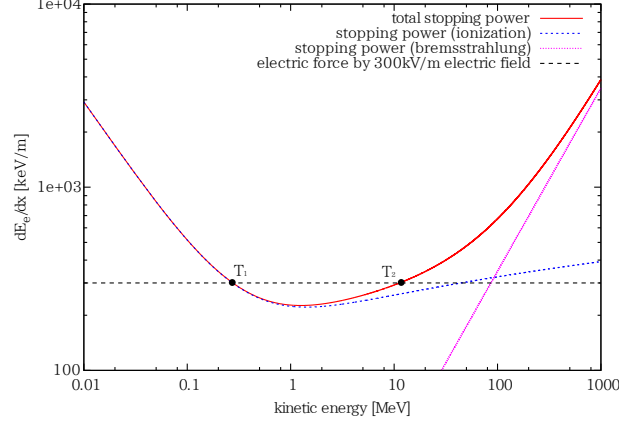


Figure 1.1: The stopping power of an energetic electron in the air in the standard conditions. The blue dotted line shows the stopping power by ionization, the pink line shows the stopping power by bremsstrahlung and the red line is summation of them. In addition, electric force on electrons by 300 kV/m electric field is plotted by black dotted line.

stopping power decreases with an increase of the electron velocity. In the relativistic region, however, it begins increasing. Consequently, the stopping power has a minimum value. It is $|dE_e/dx|_{\min} = 230 \text{ keV/m}$ (at electron energy $T_e = 1.25 \text{ MeV}$) for dry air at STP.

When the electron is accelerated by the electric field which is larger than $|dE_e/dx|_{\min}/e$, the balance equation

$$eE - \left| \frac{dE_e}{dx} \right|_{(\text{ion+brems})} = 0 \quad (1.4)$$

has two roots, which are shown in Figure 1.1 as $T_1 = 0.28 \text{ MeV}$ and $T_2 = 11.26 \text{ MeV}$ in kinetic energy. The first (non-relativistic) root T_1 is unstable. An electron slows down when kinetic energy of the electron T_e is smaller than T_1 and accelerates if $T_e > T_1$. On the other hand, the second (relativistic) root is stable since an electron with $T_e > T_2$ slows down and an electron with $T_e < T_2$ accelerates.

Consequently, some seed electrons which have energy larger than T_1 tend to develop into the equilibrium state T_2 . Energy development of electrons injected into the 300 kV/m electric field with kinetic energy $\sim T_1$ and direction parallel to the electric field is

$$T_e(x) = \int_0^x \left(eE - \left| \frac{dE_e}{dx} \right|_{(\text{ion+brems})} \right) dx, \quad (1.5)$$

which is plotted in Figure 1.2. The low-energy electrons are accelerated in short path length to some extent and electrons with energy near T_2 need long distance to get more energy.

The electrons in the equilibrium state has enough energy to knock on electrons during moving through in the air. A part of the knocked-on electrons which have energy larger than T_1 are accelerated by the electric field to the equilibrium state. The number of those “runaway” electrons increases exponentially with this process[31].

Torii *et al.* [40], with numerical calculations for a simplified model of thundercloud electric field, suggested that the electromagnetic avalanche can be produced with the relatively strong electric field, which accompanies tripole winter thunderclouds. If energetic seed electrons are provided continuously, for example, by cosmic rays, a significant flux of relativistic runaway electrons in their lower parts is capable of producing intensive secondary bremsstrahlung which can reach the Earth’s surface to account for the on-ground dose increases. Characteristics of those on-ground flux of radiation were calculated by Babich *et al.* [41].

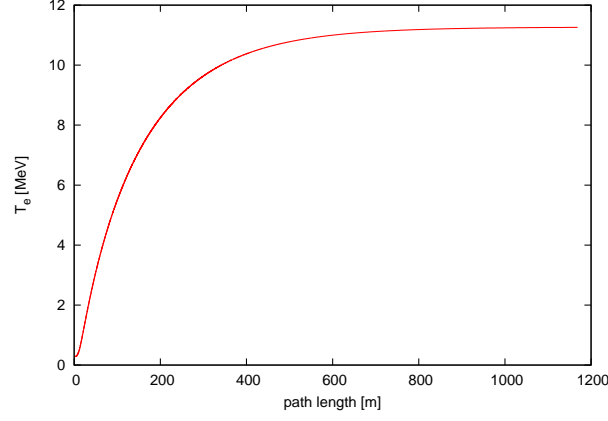


Figure 1.2: Relation between energy and acceleration length of the electrons injected into the 300 kV/m electric field with kinetic energy $\sim T_1$.

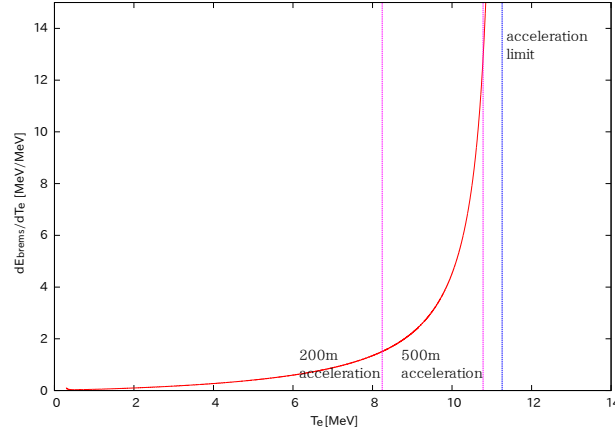


Figure 1.3: Relation between the energy of the electron accelerated in 300 kV/m electric field and energy loss of electron via bremsstrahlung. Two pink lines shows the maximum attainable energy with 200 m and 500 m acceleration.

The bremsstrahlung energy loss in each kinetic energy of the electrons accelerated by 300 kV/m field in the air (Figure 1.3) is

$$dE_{\text{brems}}(T_e) = \left| \frac{dE_e}{dx} \right|_{\text{brems}} dx = \left| \frac{dE_e}{dx} \right|_{\text{brems}} \left(eE - \left| \frac{dE_e}{dx} \right|_{(\text{ion}+\text{brems})} \right)^{-1} dT_e. \quad (1.6)$$

The figure shows that when the acceleration region in the thunder cloud is long enough a large amount of bremsstrahlung mainly comes from high energy electrons near the acceleration limit, which corresponds to the equilibrium energy T_2 .

1.3 Neutron production by lightning

Along with γ -ray production associated with thunderstorms, neutron generation in lightning flashes attracted attention. The generation of neutrons provide information about the lightning discharge. Moreover, it may have a significant effect on ^{14}C dating through the neutron capture reaction $n(^{14}\text{N}, ^{14}\text{C})^1\text{H}$.

Table 1.1: PANDA-prototype experiments

generation of the prototype	term of measurement	site	intent
Lesser PANDA (16 modules: ~ 160 kg target)	March 4th, 2011 - May 16th 2011	Unit 3 of the Hamaoka Nuclear Power Plant (Chubu Electric Power Co., Inc)	background measurement at the reactor site [51]
PANDA36 (36 modules: ~ 360 kg target)	November 18th, 2011 - January 18th, 2012	Unit 2 of Ohi Power Station (Kansai Electric Power Co., Inc)	to measure the difference of the neutrino flux associated with the reactor shut down[52]
PANDA64 (64 modules: ~ 640 kg target)	February 2013 - July 2013 (intermittent)	Hongo Campus of the University of Tokyo	detector commissioning and the background measurement

Libby and Leukens [42] have first suggested that neutrons are generated in lightning flashes. The first direct measurement [43] yielded null results. The positive result was first reported by Shah [44] in 1985. They observed statistically significant enhancements in the neutron flux in correlation with lightnings.

The mechanism of neutron generation by the lightning plasma is not well understood. Initially, Libby and Leukens assumed that the neutrons are produced through the fusion of deuterium contained in the atmospheric water vapor: ${}^2\text{H}({}^2\text{H}, n){}^3\text{He}$. It was, however, shown that the fusion cannot occur to any relevant or measurable degree under the electrical condition present in thunderstorms [45]. The photonuclear reactions (γ, n) caused by γ -rays generated by bremsstrahlung of the accelerated electrons can be the origin of the neutron enhancements as the detected γ ray spectrum extends above the photonuclear reaction threshold for nitrogen ($\sim 10.5\text{MeV}$) [46]. The mechanism of neutron production is still a matter of research.

Recently, the neutron bursts associated with thunderstorms were repeatedly observed in various experiments. The experiments are performed with detectors at Mumbai (sea level) [47], Aragats (altitude 3200 m) [15], the city of Saõ Jos  dos Campos (about 600 m above sea level) [48], Tien Shan (altitude 3340 m) [49] and the Tuimaada Valley near Yakutsk (about 100 m above sea level) [50]

1.4 Detection with prototype PANDA detector

As we will describe in detail in Chapter 3, our research group have developed prototypes of a reactor neutrino detector PANDA, which stands for Plastic Anti-Neutrino Detector Array. We have originally targeted at presenting the feasibility of reactor monitoring using neutrinos with a small, tonne-size detector. We planned to install the PANDA detector outside of the reactor building and surveil the reactor operating status via detecting and analyzing the anti-electron neutrinos produced in the reactor core.

From 2011 to 2013, we have made commissioning of the detector and attempted neutrino detection. We deployed our prototype detectors on various sites and measured the neutrino flux and the background spectrum. They are listed in Table 1.1.

We found that there were intensive increases of γ -ray flux correlated with the winter thunder-

storm activity in measurement at Ohi Power Station. In this paper, we report the investigated properties of these burst events taking advantage of the features of the PANDA detector including high statistics, direction sensitivity and ability to distinguish particles.

Chapter 2

Recent distinct results of the observations of the γ -rays associated with thunderclouds

2.1 GROWTH experiment

Radiation-monitoring posts installed in nuclear power plants in the coastal area of Sea of Japan have frequently detected prolonged radiation bursts associated with winter thunderstorms. In order to investigate details of the bursts such as the particle species, arrival direction and energy spectrum, a Japanese group have been operating the Gamma-Ray Observations of Winter Thunderclouds (GROWTH) experiment since 20 December 2006 [21, 22, 23, 24].

GROWTH experiment took place at Kashiwazaki-Kariwa nuclear power plant, which is located in the coastal area of Sea of Japan in Niigata prefecture. Thunder activity is very high in winters there. They used two independent and complementary detectors.

One detector used two cylindrical NaI(Tl) scintillators (a diameter and a height of both 7.62 cm), which are individually surrounded by well-shaped $\text{Bi}_4\text{Ge}_3\text{O}_{12}$ (BGO) scintillators (Figure 2.1). The BGO scintillators shielded the central NaI up to a solid angle of $0.6 \times 4\pi$ so that the NaI scintillators had a higher sensitivity toward the sky direction. A 0.5 cm thick plastic scintillator was placed above the two NaI scintillators to distinguish charged particles. The other detector consisted of spherical NaI(Tl) and CsI(Tl) scintillators (diameter of 7.62 cm each). These scintillators had omnidirectional sensitivity.

In addition to those radiation detectors, they deployed light sensors and an electric field sensor to detect lightnings.

They have reported that intense burst of γ -rays lasted for ~ 1 minute was detected in winter season of 2007 [21, 22], 2008 [23] and 2010 [24]. The detected photon spectrum extends up to 10 MeV, suggesting that the strong electric field in the thunderclouds can continuously accelerate electrons beyond 10 MeV. They utilized Monte-Carlo simulations to conclude that the observed photons can be interpreted as being radiated from a source located at a distance of 290-560 m and 110-690 m [23] above the detector.

In recent study, they have reported the first observation of 3–30 MeV prolonged γ -ray emission [24]. Since high energy > 10 MeV photons are emitted in a narrow cone and undergo less Compton scatterings than lower energy photons, the area of the > 10 MeV γ -rays almost equals that of the whole acceleration region. They inferred that the size of the area was about 180 m, which was smaller than the region of a positively-charged layer located at the base of the electrically active phase of the winter thunderclouds.

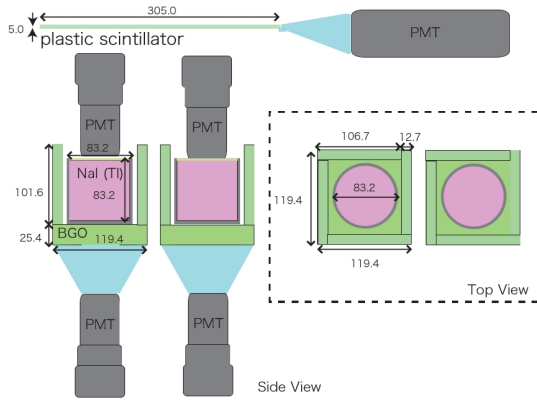


FIG. 1 (color). Schematic views of the two main sensors and the plastic scintillator of detector-A—photomultiplier (PMT). Numbers represent scales in millimeter.

Figure 2.1: Schematic views of the one of the GROWTH detectors (cited from ref. [22])

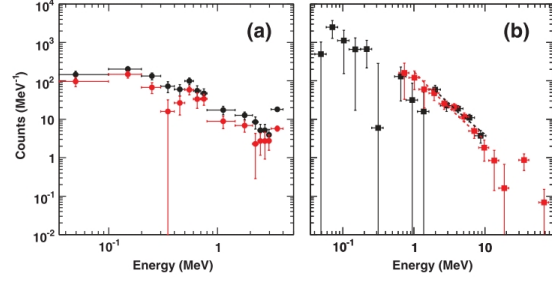


FIG. 4 (color). Background-subtracted photon energy spectra accumulated over the 36 sec. All horizontal and vertical axes show the photon energy and the counts per each energy bin, respectively. Error bars are statistical 1σ . (a) Spectra from detector-A. Black and red circles show data of the main NaI counters (summed over the two units), without and with the BGO anticoincidence. (b) Spectra from detector-B. Black and red squares are from NaI and CsI counters, respectively. Black and red dashed lines show predictions of the best-fit incident power-law model, determined over the energy range where the dashed lines are drawn.

Figure 2.2: Photon energy spectrum observed via GROWTH detectors (cited from ref. [22])

2.2 Detection of source migration

Torii *et al.* [25] investigated location and behavior of the source of the energetic radiations associated with winter thunderclouds.

Their observation were conducted from December 2009 to February 2010 at Fugen, Tsuruga Power Station and their vicinities on the tip of the Tsuruga Peninsula facing the Sea of Japan. They deployed three cylindrical NaI detectors (diameter and a height of about 1.0×10 cm), at observation points distant from each other. They also installed electric field-mills to monitor the variations in atmospheric electric field.

In addition, they took advantage of data of seven environmental radiation monitors (ERMs) using NaI detectors to investigate the behavior of the radiation source during thunder storm activities. Also the data of composite weather radar echos (2km height) and vertical radar echo profiles recorded by Japan Meteorological Agency was used.

They observed a significant increase of energetic radiation on 7 January 2010. The time differences of the radiation peak of each detector and monitor are shown in Figure 2.3. The correlation between latitudinal distance and time difference suggested that the area of enhanced radiation moves from north to south with the speed of about 7.1 m/s. The composite weather radar echoes at 2km height showed a movement of intense echoes from north to south around the tip of the Tsuruga Peninsula when the enhancement of energetic radiation is observed.

Assuming that the emission of the radiations from the source is isotropic and constant in time, they estimated that the shape of the radiation source was a downward hemispherical surface with a radius of 700 m and it was centered at 1000 m altitude. And the source was moving to the south at the speed of about 7 m/s.

They concluded that the intensive long burst of the energetic radiation is generated mainly below the charged region of the thunderclouds and the migration of its source is accompanied with the thundercloud movement.

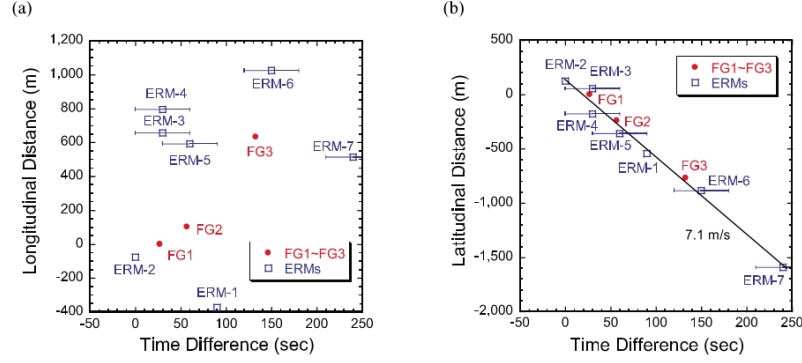


Figure 3. The correlation between the time of the radiation peak and (a) the longitudinal and (b) the latitudinal locations of observation point. The time at ERM-2 and location at FG1 are set to be zero.

Figure 2.3: The time differences of the radiation peak of each detector (cited from ref. [25])

2.3 Comprehensive observation at Aragats Space-Environmental Centre

The Aragats Space Environmental Centre (ASEC) facilities continuously measure fluxes of neutral and charged secondary cosmic ray incidents on the Earth's surface [53, 54]. Chilingarian *et al.* reported that the facilities detected enhancements in the electron, γ -ray and neutron fluxes correlated with thunderstorm activities.

The particle detectors of the ASEC were located in Yerevan (1000 m altitude) and on slopes of Mt. Aragats at altitudes 2000 and 3200 m. The thunderstorm activity on Aragat is extremely strong in May–June, and its clouds are sometimes 100–200 m above the station. ASEC has comprehensive set of detectors; Aragats Solar Neutron Telescope (ASNT), Aragats Neutron Monitor (ArNM), SEVAN (Space Environmental Viewing and Analysis Network) particle detectors and surface arrays consist of the plastic scintillators.

They detected large enhancements of the electrons and γ -rays supposed to be multiplied by the RREA process [15, 16, 17]. The electron energy spectrum extended to ~ 30 MeV and that of γ -ray continued till ~ 50 MeV.

It is remarkable that they reported the enhancements of the neutrons were detected by the ArNM [15]. In radiation enhancement event on September 19, 2009, the ArNM, whose sensitivity to electrons, muons and γ -rays are ignorable, showed enhancement simultaneous to the other detectors (Figure 2.4).

Their observation provided the collateral evidence for existence of the long-lasting electron-photon avalanches developing in the atmosphere during thunderstorms and the photonuclear mechanism for neutron production.

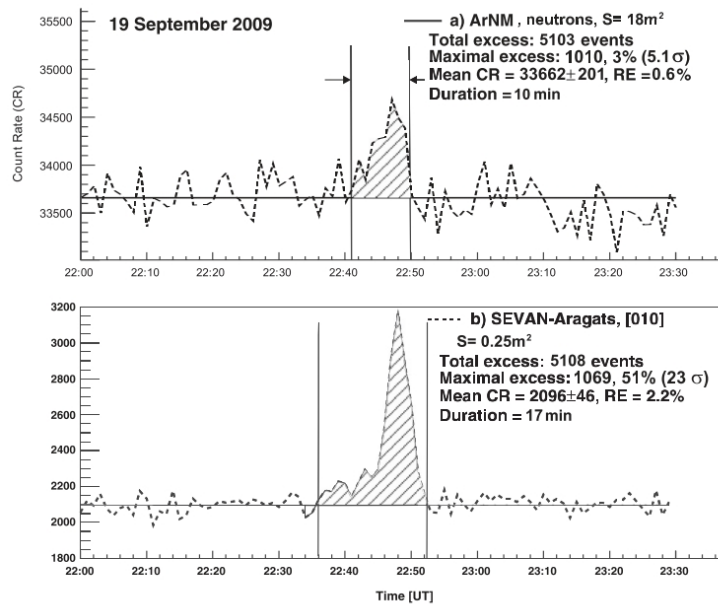


FIG. 8. One-minute time series of the particle flux detected by the SEVAN and ArNM detectors (a) 1-minute time series of ArNM. (b) 1-minute time series of SEVAN (010 combination). The additional particles are demonstrated by the dashed areas.

Figure 2.4: ArNM enhancement simultaneous to the SEVAN detector (cited from ref. [15])

Chapter 3

Design of the detector and data acquisition

3.1 Plastic Anti-Neutrino Detector Array (PANDA)

To investigate γ -ray storms related to the thunderclouds, we took advantage of the data acquired through a measurement of the reactor neutrinos and test runs of our reactor neutrino detector. The measurements were carried out outside the buildings using prototypes of the reactor neutrino detector, “PANDA”, which stands for Plastic Anti-Neutrino Detector Array. The original aim of the PANDA detector was to demonstrate that the reactor monitoring using anti-neutrino detection technique is feasible using relatively small detectors.

Our prototype detectors consist of stacked modules, which are based on 10-kg plastic scintillator bars. The number of modules were increased according to the stage of development. Sixteen modules were used for the first prototype “Lesser PANDA”, and subsequently thirty-six modules and sixty-four modules were used for the second prototype “PANDA36” and the third prototype “PANDA64” respectively.

Although we did not use all features of the prototypes of the PANDA detector to investigate γ -rays related to the thunderclouds, we describe the design and the data acquisition system of the PANDA detector making mention to the original intent and the properties as the anti-neutrino detector in this chapter.

3.2 Reactor monitoring and safeguards using anti-neutrino detectors

The International Atomic Energy Agency uses an ensemble of procedures and technologies, collectively referred to as the Safeguards Regime, to detect diversion of fissile materials from civil nuclear fuel cycle facilities into weapons programs. Recent years, IAEA recommends investigation of near-field anti-neutrino monitoring capabilities for providing reactors for the safeguard regime. Reactor monitoring by anti-neutrinos have the advantage that there is no need to intrude into the reactor buildings because of the highly penetrating power of anti-neutrinos. And the subject institutions or states of the investigation can hardly fake the anti-neutrino spectrum since anti-neutrinos are difficult to be created without reactor or accelerators.

Anti-Neutrinos are produced by the decay of the fission products in the reactor cores. Reactors are the most intense man-controlled sources of neutrinos. With an average energy of about 200 MeV released per fission and about 6 neutrinos produced along the β -decay chain of the fission products, a total flux of $2 \times 10^{20} \nu/\text{s}$ is emitted by a 1 GW_{th} power plant. Since unstable fission products are neutron-rich nuclei, all β -decays are of β^- type and the neutrino flux is actually of pure electron anti-neutrinos ($\bar{\nu}_e$). A prediction of its production rate and

Table 3.1: Coefficient parameters for anti-neutrino flux[56]

isotope	α_1	α_2	α_3	α_4	α_5	α_6
^{235}U	3.217	-3.111	1.395	-3.690E-1	4.445E-2	-2.053E-3
^{238}U	4.833E-1	1.927E-1	-1.283E-1	-6.762E-3	2.233E-3	-1.536E-4
^{239}Pu	6.413	-7.432	3.535	-8.820E-1	1.025E-1	-4.550E-3
^{241}Pu	3.251	-3.204	1.428	-3.675E-1	4.254E-2	-1.896E-3

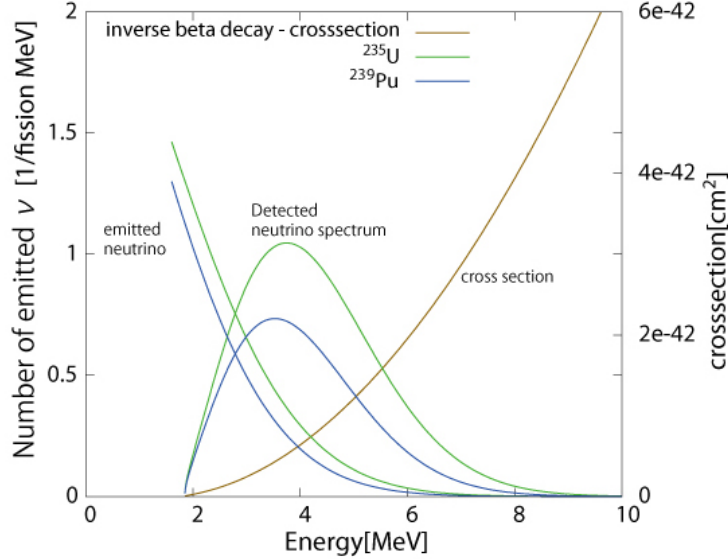


Figure 3.1: Number of anti-neutrino emitted by a fission from a reactor core (^{235}U , ^{239}Pu ; left ordinate), the cross section of the inverse beta decay (right ordinate), and the expected energy spectrum of the anti-neutrinos detected by the inverse beta decay (arbitrary unit).

spectrum associated with the fission of ^{235}U , ^{238}U , ^{239}Pu and ^{241}Pu exists[55] and was recently revisited[56][57].

An approximate formula for the anti-neutrino energy spectra per fission from element k is provided using an exponential of a polynomial[56]:

$$S_k(E_\nu) = \exp \left(\sum_{p=1}^6 \alpha_{p,k} E_\nu^{p-1} \right). \quad (3.1)$$

In this equation, $S_k(E_\nu)$ is the energy spectra in $\text{MeV}^{-1}\text{fission}^{-1}$, and E_ν is the energy of the anti-neutrino in MeV. The coefficient parameters $\alpha_{p,k}$ for each isotope is shown in Table 3.1. The predicted energy spectra is shown in Figure 3.1.

The measurements of the anti-neutrino detection rate provide information about the thermal power of a reactor and its fuel composition (Figure 3.1). But one cannot independently separate the effect of these two parameters on the detection rate. For example, independent information about the reactor power history would be needed to investigate the fuel evolution. Measurement of the anti-neutrino energy spectrum may allow for the independent estimation of the reactor power and its fuel components.

3.3 Electron anti-neutrino detection by inverse-beta decay

With the PANDA detector and in many other experiments detecting reactor neutrinos, anti-neutrinos are detected via the inverse beta decay process:

$$\bar{\nu}_e + p \rightarrow e^+ + n \quad (3.2)$$

and following reactions:

$$e^+ + e^- \rightarrow 2\gamma, \quad (3.3)$$

$$n + {}^{155}\text{Gd} \rightarrow {}^{156}\text{Gd}^* \rightarrow {}^{156}\text{Gd} + \gamma\text{'s}, \quad (3.4)$$

$$n + {}^{157}\text{Gd} \rightarrow {}^{158}\text{Gd}^* \rightarrow {}^{158}\text{Gd} + \gamma\text{'s}. \quad (3.5)$$

Here the anti-neutrino $\bar{\nu}_e$ interacts with the proton p which presents in the plastic scintillator. The neutron n and the positron e^+ are detected by delayed coincidence, providing a dual signature allowing strong rejection of the much more frequent singles backgrounds due to natural radioactivity or cosmogenic neutrons.

The positron deposits energy via Bethe-Bloch ionization as it slows in the scintillator, and upon annihilation with an electron, it emits two γ -rays which can deposit additional energy of up to 1.022 MeV. On the other hand the neutron carries away a few keV of energy from the anti-neutrino interaction and is detected by capture in a Gd on the film with an energy release of ≈ 8 MeV via a γ -ray cascade. Reaction (3.2) has an energy-dependent cross section and a neutrino energy threshold of 1.806 MeV. The cross section and the expected energy spectrum of the anti-neutrinos detected by the inverse beta decay are shown in Figure 3.1

3.4 Design of the detector

IAEA proposed the development of the compact detector within a standard 12 meters ISO container (approximately 25,000 kg net load) and the aboveground deployment as medium term (5 – 8 year time frame) goals[58]. Corresponding to these requirements, we proposed the PANDA detector whose concept design is shown in Figure 3.2. The detector consists of one hundred identical modules, which is described in Section 3.5. As it has fine segmented structure, it becomes possible to use the event topology information to tag anti-neutrino events and to discriminate them from background.

The fine segmentation of the detector also gives the capability to identify and reject passing tracks such as cosmic ray muons. Passing muons are characterized by series of hits distributed along a line in the detector. Therefore, the PANDA detector does not need additional veto counters surrounding the whole detector.

As preliminary steps before building the full-size PANDA detector, a smaller prototype “Lesser PANDA” with 16 modules (Figure 3.3), “PANDA36” with 36 modules (Figure 3.4) and “PANDA64” with 64 modules (Figure 3.5) were constructed and were tested. It is notable that we measured the reactor neutrinos for about two months at Ohi Power Station in Fukui by PANDA36, and marginally observed the difference of anti-neutrino flux before and after the shutdown of the reactor[52].

3.5 Module

The modules of the PANDA detector were made of plastic scintillator bars (10cm \times 10cm \times 100cm) wrapped with aluminized Mylar films and gadolinium (Gd) coated Mylar films (4.9 mg of Gd per cm²). Each bar was connected to acrylic light guides and photomultipliers on both ends (Figure 3.6). The plastic scintillators were REXON RP-408 or ELJEN EJ-200 and the Gd coated films were manufactured by Ask Sanshin Engineering with their neutron shielding paint. Hamamatsu H6410 (R329-02) PMTs were used for light detection.

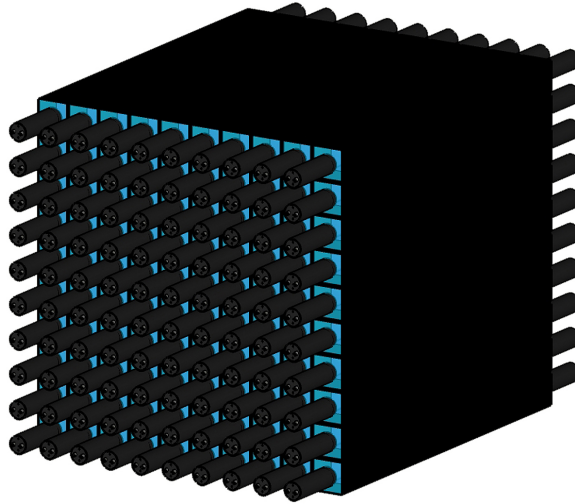


Figure 3.2: The concept design of the PANDA anti-neutrino detector. The approximate total target size is 1 m^3 .



Figure 3.3: Lesser PANDA: A prototype of the PANDA detector, which consists of 16 modules



Figure 3.4: PANDA36: The prototype of the PANDA detector, which consists of 36 modules



Figure 3.5: PANDA64: The prototype of the PANDA detector, which consists of 64 modules

The light intensity ratio seen by each PMT pair allows one to estimate the position of the hit along the module. Assuming the fraction p of the light is attenuated in the plastic scintillator exponentially as a function of distance from the point of emission to the PMT and the other $(1 - p)$ propagates practically without attenuation by repeating total internal reflection at the surface (Figure 3.7), the hit position and the light intensity are related through a simple equation:

$$L_{\text{PMT}} = L_{\text{emitted}}((1 - p) + p \exp(-x/l)). \quad (3.6)$$

In this equation, L_{emitted} and L_{PMT} are the light intensity emitted by the scintillator and getting into the PMT, l is the attenuation length of scintillation light, and x is the distance of the hit position from the PMT. Figure 3.8 shows that the above relation (3.6) fits the data well. Using the position of the hit and the charge outputs from each PMT, one can estimate the energy deposit of the hit. The position and energy resolutions which depend on the deposited energy were about 45 cm and 100 keV for 500 keV hit (16 cm and 300 keV for 4 MeV hit) on the center respectively.

3.6 Data acquisition system

Figure 3.9 shows the simplified block diagram of the data acquisition system for the Lesser PANDA detector. Each PMT signal was divided into two: about 28% of the original charge was sent to CAEN V792 multi-event Charge-to-Digital-Converters (QDCs) and the other 72% was passed to Technoland Corporation N-TM 405 leading edge discriminators.

In the DAQ system of the Lesser PANDA detector, gates for the QDCs were produced by the following trigger logic. A hit multiplicity was counted by a REPIC RPN-130 multiplicity logic module and a logic pulse was sent to a gate generator whenever four or more PMTs fired in coincidence with one another giving typical trigger rate of 2.7 kHz. Non-retriggerable logic pulses of 400 ns duration were produced here. The coincidence width of the multiplicity logic was 80 ns. Corresponding to each trigger, the charge outputs of all PMTs were recorded by the QDCs. Meanwhile the trigger timing was recorded by a custom-made time stamper.

The time stamper of the Lesser PANDA detector was implemented on a Xilinx Spartan-6 FPGA running at 50-MHz clock. The trigger timing information allows one to calculate the interval between a pair of events. The time stamper also recorded the timing of the busy signals from QDCs which was used to calculate the dead time of the measurements. These timing information was stored in a cache memory on the FPGA once and sent to a hard disk drive sequentially via USB 2.0 (Universal Serial Bus 2.0). The data transfer speed of USB 2.0 is high enough to run without dead time due to the time stamper at trigger rate of 2.7 kHz.

Figure 3.10 shows the data acquisition system for the PANDA36 detector. The DAQ system of PANDA64 has almost the same structure.

Division ratio of the dividers was changed from 28 : 72 of the Lesser PANDA DAQ system to 15 : 85; 15% of the original charge was sent to the QDCs and 85% was passed to CAEN V895 leading edge discriminators. The picture of the divider for PANDA36 and PANDA64 is shown in Figure 3.11. The divider was constructed from Aluminum C-channel and 3 connectors (1 BNC connector for the PMT and 2 QLA connectors for the QDC and the discriminator). We connected the dividers to PMTs output directly. Schematic diagram of the circuit was shown in Figure 3.12.

In the DAQ system of PANDA36 and PANDA64, a hit multiplicity was counted and gate pulses of 400 ns duration were generated by logic implemented on CAEN V1495 general purpose VME board, which has customizable FPGA unit (Altera Cyclone EP1C20). The FPGA unit was running at 40-MHz clock for the PANDA36 detector and at 80-MHz clock for the PANDA64 detector. The logic counted the number of pairs of fired PMTs seeing the same scintillator. Whenever the number of the pairs was greater than or equal to the predefined number (two for the PANDA36 detector and one for the PANDA64 detector), the logic invoked the gate pulses.

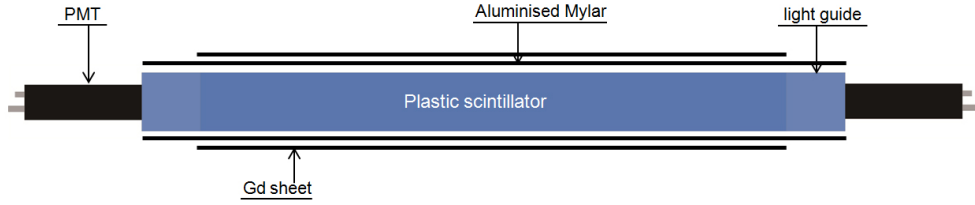


Figure 3.6: Structure of the PANDA module

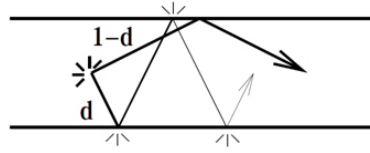


Figure 3.7: Light propagation model in the plastic scintillator bar

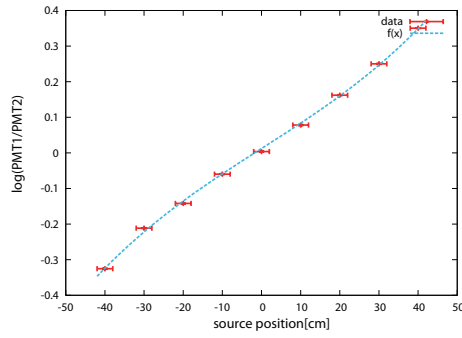


Figure 3.8: Logarithm of the ratio of PMT charge measured at one end to charge at the other end of the module vs. source position. The dashed curve is a two-parameter (p and l in equation (3.6)) fit of the ratio predicted by the light attenuation model.

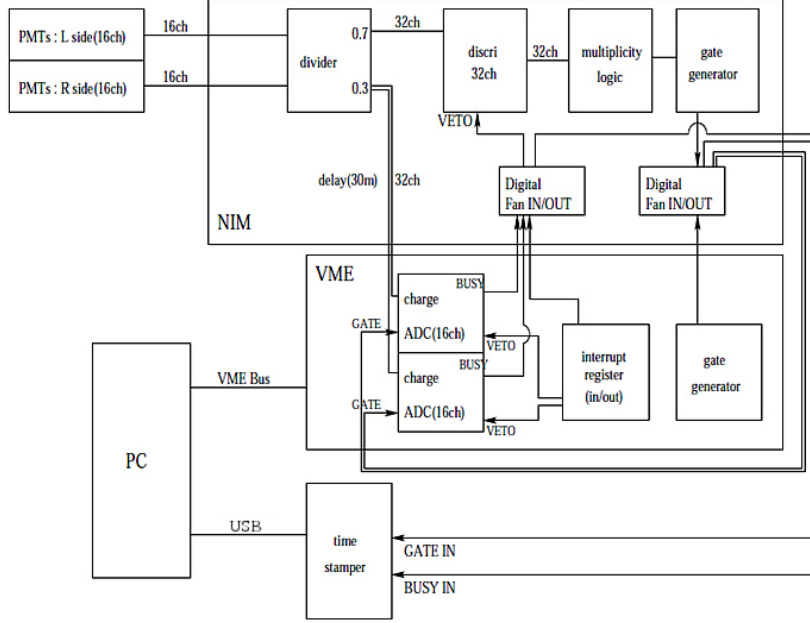


Figure 3.9: Simplified block diagram of the data acquisition system for Lesser PANDA

The timing of the gate pulses and busy signals from the QDCs were recorded by the same FPGA. The DAQ system became simpler by implementing the multiplicity logic, gate generator and time stamper on one board. The timing information was stored in a cache memory on the FPGA once and sent to the PC via VME bus. The data transfer speed of VME bus is also high enough to run without dead time due to the time stamper at the typical trigger rate (2.0 kHz for PANDA36 and 9.5 kHz for PANDA64).

Both the time stamper and the QDCs recorded the number of gate pulses so that we could combine these data to know the time of each event. We used these time stamps to select neutrino events by delayed coincidence method offline.

We set up periodic pauses of the data acquisition to assure the synchronism of the data from all the QDCs and the time stamper was retained. During the pauses, the data acquisition system counted the number of the collected data and when any mismatches among the QDCs or the time stamper were found, the system discarded all the data after the previous synchronization process. Due to the conversion times of the QDCs (about $5.5\mu\text{s}$ - $7.5\mu\text{s}$) and synchronization process, the DAQ systems had about 3.5%, 3.1% and 7.6% dead time with the typical trigger rate for the Lesser PANDA detector, the PANDA36 detector and the PANDA64 detector respectively. The QDCs have 32 event buffer memories and they incur little dead time as long as the read out system can sustain the data rate.

The amount of data transferred from QDCs to the PC was small enough for the Lesser PANDA detector and the PANDA36 detector ($\sim 400\text{ kB/s}$ and $\sim 800\text{ kB/s}$ respectively). The PANDA64 detector, however, has the 128 PMTs and the increased trigger rate. Consequently the amount of the data transferred could not be ignored with respect to the data transfer rate of the VME bus. We reduced the transferred data quantity by taking advantage of zero suppression feature of the CAEN V792 multi-event QDC. If the digital data converted from the analog signal was lower than the preset threshold, the data would be deleted and never be transferred via VME bus. The zero-suppression threshold was determined dynamically by measuring the fluctuation width of the pedestal. The pedestal peak was fitted by a Gaussian function and $u + 3\sigma$ was used as the threshold; where u is the center of the peak and σ is the standard deviation of the function. As a result, the maximum event rate which can be managed by the DAQ system of

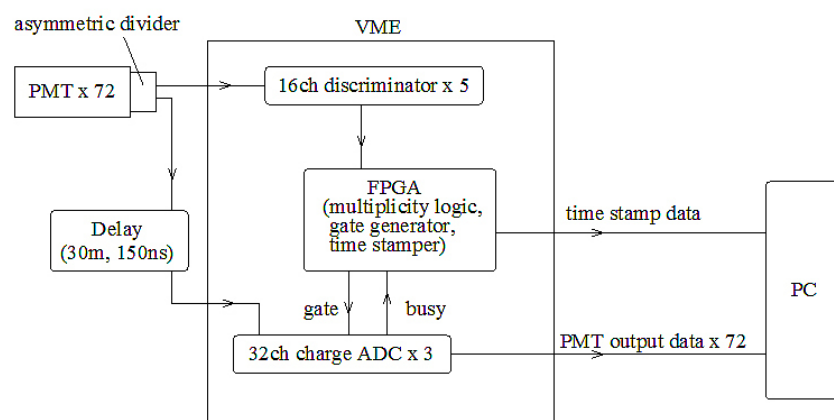


Figure 3.10: Simplified block diagram of the data acquisition system for PANDA36



Figure 3.11: Picture of the divider

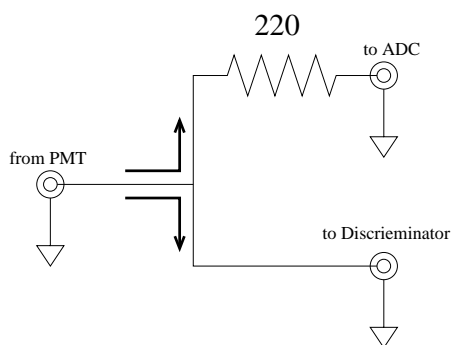


Figure 3.12: Circuit of the divider

PANDA64 became about 20 kHz and it was enough larger than the typical trigger rate.

3.7 Transportation and Deployment

The Lesser PANDA detector and the DAQ system were loaded on a 2-ton dry van (Figure 3.13). and was transported to the Hamaoka Nuclear Power Plant of Chubu Electric Power Co., Inc on March 3rd, 2011. The van was parked just next to the Unit 3 building of the plant and the measurement was carried out as the detector was on the van.

There were three operational reactors in this station; all of them were boiling-water reactors and have maximum thermal (electric) power of $3.3-3.9 \text{ GW}_{\text{th}}$ ($1.1-1.4 \text{ GW}_{\text{e}}$) each. The detector was located at a distance of 39.8 m from the Unit 3 ($3.3 \text{ GW}_{\text{th}}$) reactor core. The measurement was continued for 68 days. The Unit 3 reactor was under scheduled inspection and was not in operation then. We were waiting for the reactor to start up but it did not because of the 2011 off the Pacific coast of Tohoku Earthquake.

The PANDA36 detector was also loaded on and transported by a 2-ton dry van. The detector was deployed at Unit 2 of Ohi Power Station of Kansai Electric Power Co., Inc on November 18th, 2011.

There were four operational reactors in this station; all of them were pressurized-water reactors and have maximum thermal (electric) power of $3.4 \text{ GW}_{\text{th}}$ ($1.2 \text{ GW}_{\text{th}}$) each. The detector was located by the reactor building of the Unit 2 ($3.4 \text{ GW}_{\text{th}}$) at a distance of 35.9 m from the reactor core (Figure 3.15). We continued the measurement for 62 days; of which first 28 days were the reactor on period and the other 33 days after reactor shutdown on 16th December were the reactor off period.

The PANDA64 detector was loaded on 20 ft ISO container. The container was installed next to the Faculty of Science Building 1 in Hongo Campus of the University of Tokyo. We made a background measurement for 9 days without shieldings and for 126 days with $\sim 24 \text{ cm}$ thick water shieldings surrounding the detector.

3.8 Energy calibration

Energy calibration of the detector was carried out using a ^{60}Co γ -ray source temporarily placed at three different positions: the very center of each module or the points near the edges of each plastic scintillator. Calibration constants were evaluated for each module separately. Figure 3.16 and Figure 3.17 show the schematic view of the setup for the calibration of each module.

Multiple Compton scattering of the γ -rays with energies of 1.17 MeV and 1.33 MeV in the detector or in the surrounding materials and statistical and electronic fluctuation of the output signals produce a broad spectral feature in the measured energy spectrum. To compare with the measured energy spectrum, we performed a Monte Carlo simulation of γ -ray transports in the detector using Geant4[59].

The calibration procedure was as follows: we determined the values of the pedestals; took data with a ^{60}Co source; fitted the broad spectral feature by Compton scattering of ^{60}Co γ -rays of the simulation to the three data at the same time taking into account the light attenuation described in Section 3.5.

We assumed the light intensity seen by each PMT consists of total reflection component and partial reflection component as mentioned before in relation (3.6). And we also assumed the resolution σ of L_{PMT} in relation (3.6) was

$$\sigma = \sqrt{a^2 L_{\text{PMT}} + b^2} \quad (3.7)$$

In this equation, a and b are resolution parameters. Finally, the spectrum of L_{PMT} was converted to the QDC output value using two parameters, the conversion factor from the energy scale (keV) to the QDC scale (ch) and pedestal position on the QDC scale.



Figure 3.13: PANDA36 and the DAQ system loaded on the van



Figure 3.14: The van with PANDA36 was parked just next to the reactor building.

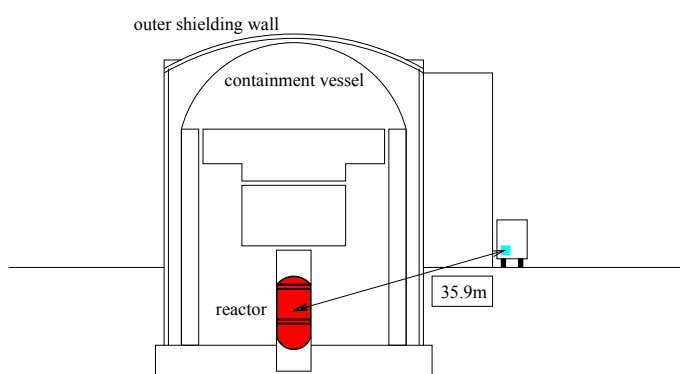


Figure 3.15: The deployed position of the PANDA36 detector by Ohi Nuclear Power Plant Unit 2 reactor

First, we fitted, by the least chi-square method, the Gaussian function to data which was taken by random timing gate signals. The b parameter of each QDC channel was estimated by the result of this fit. Next, we fitted the simulated QDC values of each PMT for three ^{60}Co source positions to the measured calibration data. This fitting calculation determined the parameter l and p of the module in relation (3.6), a , b and conversion factor of each PMTs and vertical scale of each measurement data. We adjusted the fit range to include the position of the Compton edge of γ -ray emitted by ^{60}Co . Example of the fit is shown in Figure 3.18 and Figure 3.19.

Since our discussion will be based on the data taken by the PANDA36 detector in Chapter 4 and later, determined calibration parameters for the PANDA36 detector are shown in Table 3.2–3.3. The energy and longitudinal position resolutions of modules are determined by parameters a, b, p and l and the position of the energy deposit in the module. We show some typical examples of the energy and position resolutions in Figure 3.20–3.23 and Figure 3.24–3.27.

When the detector was in operation, relative gain drift of each module was corrected using γ -rays arising from natural radioactivity (Lesser PANDA) or cosmic muons (PANDA36 and PANDA64). The background γ -ray or muon spectrum was taken just after the first calibration as a reference and each data set was compared to it.

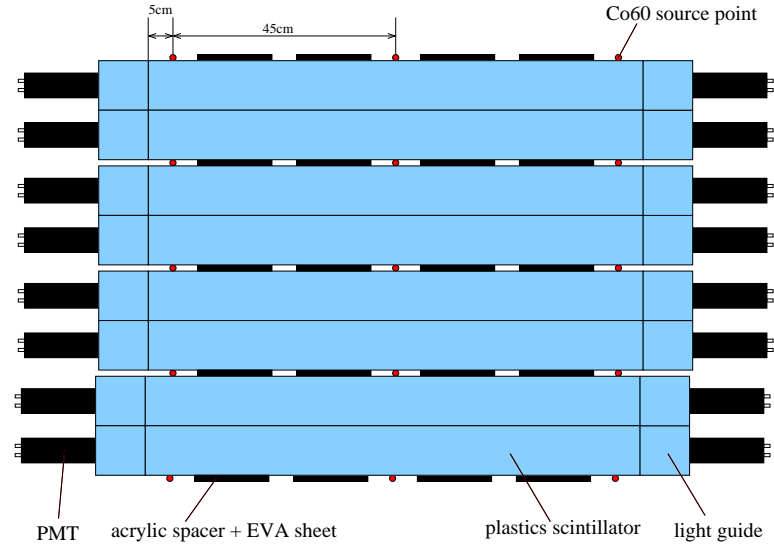


Figure 3.16: Schematic view of the setup for the calibration of each module (PANDA64; top view)

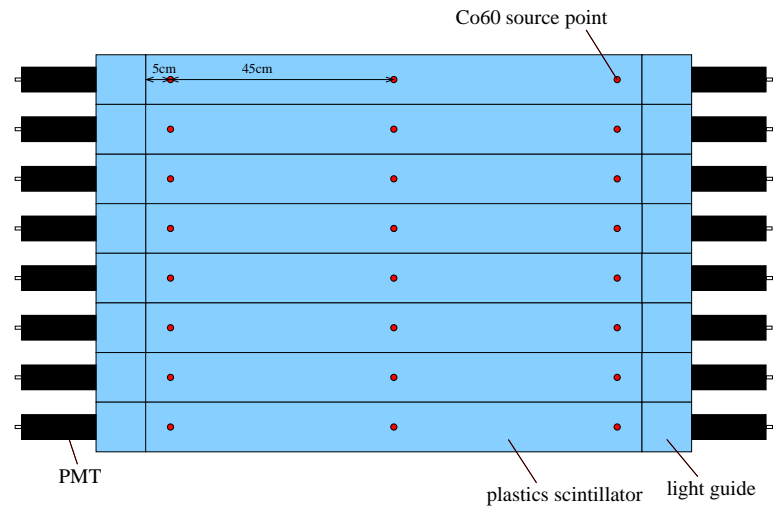


Figure 3.17: Schematic view of the setup for the calibration of each module (PANDA64; side view)

module-1 : χ^2/dof :1.18057

width_left:4.83286,a_left:3.07188,b_left:5.87239 : width_right:4.75089,a_right:3.1155,b_right:5.829 : p:0.668051 l:582.019

heights(source:L):9.91948,heights(source:C):8.45569,heights(source:R):8.92249

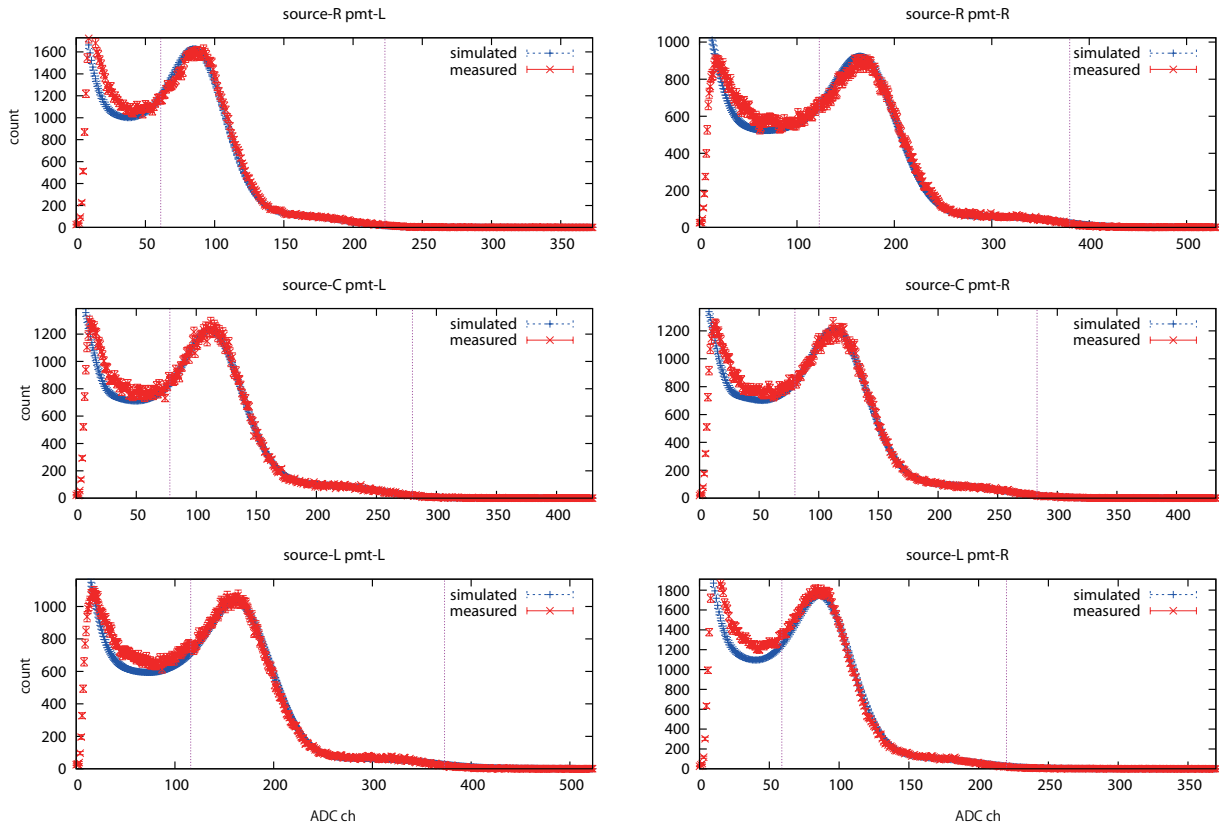


Figure 3.18: An example (module no.1 of the PANDA64 detector) of energy spectrum in one module obtained with ^{60}Co calibration source after background subtraction, compared with the Geant4 simulation (dashed line). For both simulated and measured spectra, the error bars represent the statistical error.

module-2 : chi2/dof:1.04723

width_left:3.93827,a_left:3.18635,b_left:5.16055 : width_right:3.64271,a_right:3.14748,b_right:5.37949 : p:0.707633 l:576.667

heights(source:L):10.4322,heights(source:C):8.74229,heights(source:R):9.49793

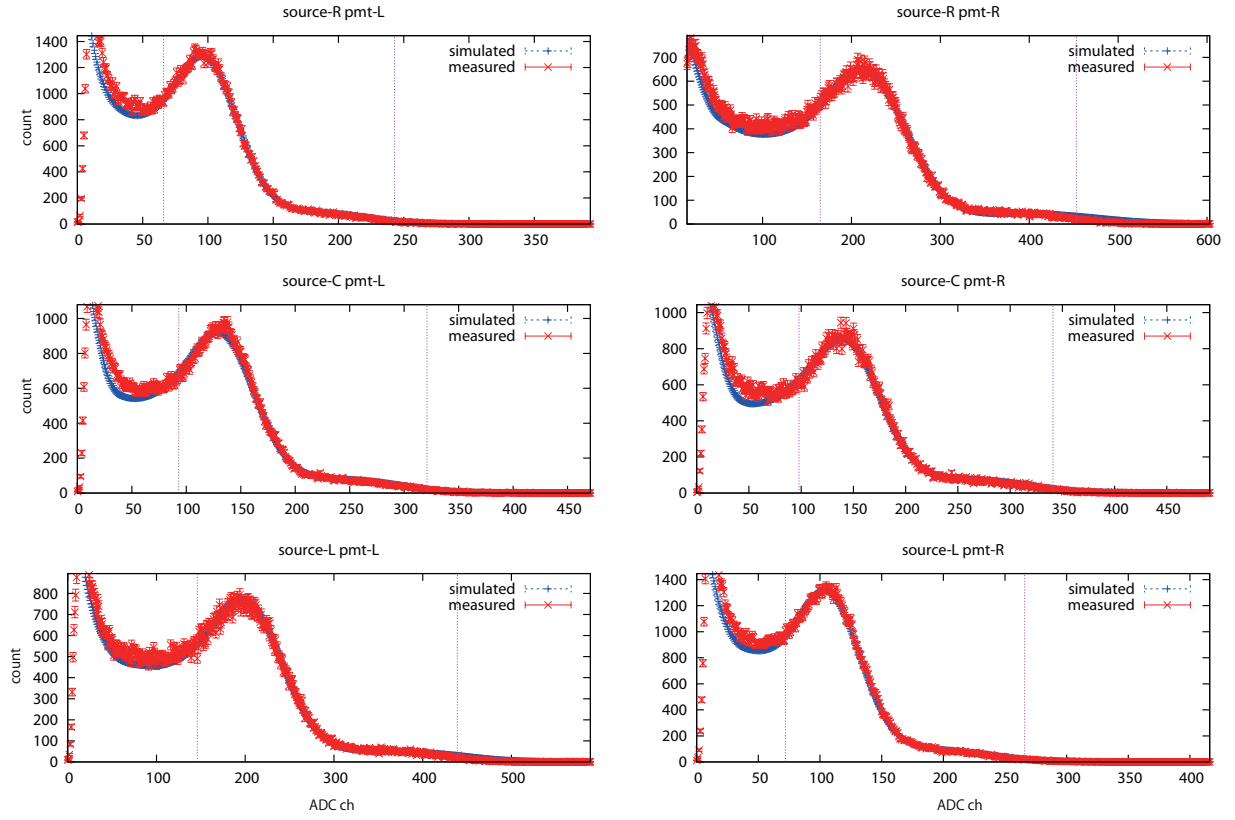


Figure 3.19: Same as Figure 3.18 but for module no.2 of the PANDA64 detector

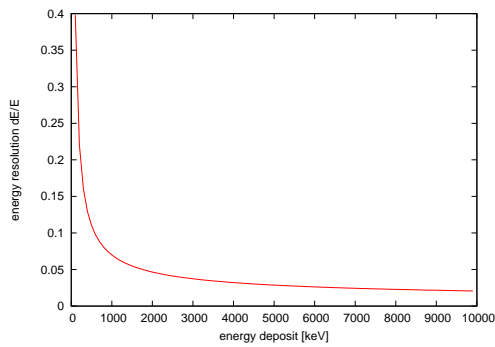


Figure 3.20: Energy resolution of module 1 in the case that γ -ray deposited energy at the center of the module

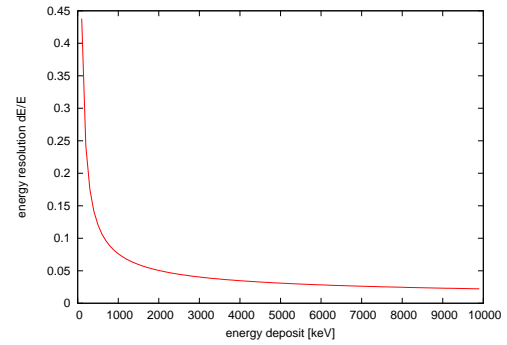


Figure 3.21: Energy resolution of module 1 in the case that γ -ray deposited energy at 300 mm away from the center of the module

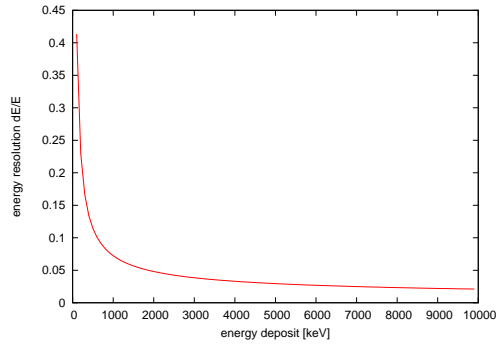


Figure 3.22: Energy resolution of module 2 in the case that γ -ray deposited energy at the center of the module

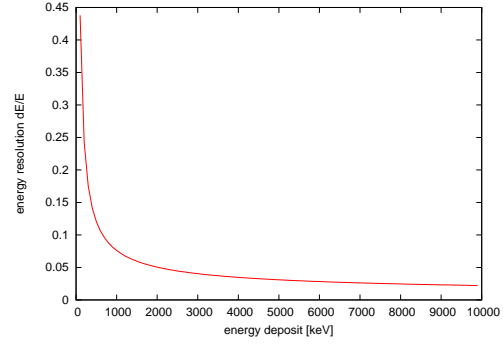


Figure 3.23: Energy resolution of module 2 in the case that γ -ray deposited energy at 300 mm away from the center of the module

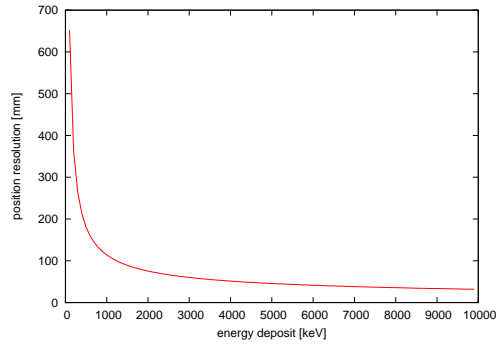


Figure 3.24: Longitudinal position resolution of module 1 in the case that γ -ray deposited energy at the center of the module

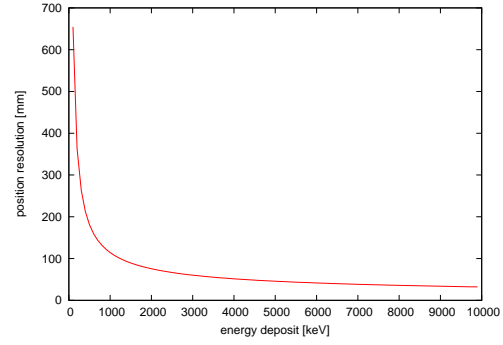


Figure 3.25: Longitudinal position resolution of module 1 in the case that γ -ray deposited energy at 300 mm away from the center of the module

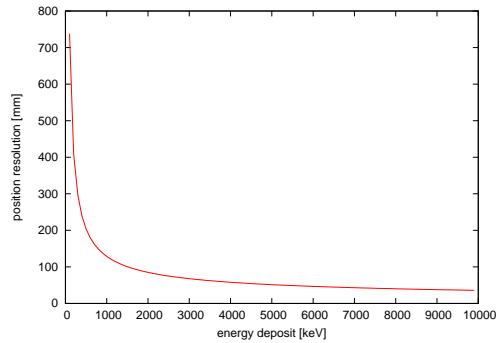


Figure 3.26: Longitudinal position resolution of module 2 in the case that γ -ray deposited energy at the center of the module

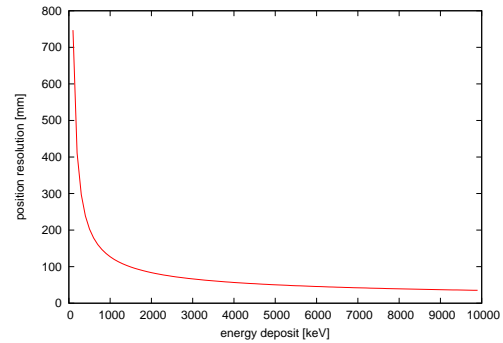


Figure 3.27: Longitudinal position resolution of module 2 in the case that γ -ray deposited energy at 300 mm away from the center of the module

Table 3.2: Parameters determined by the calibration procedure (PANDA36)

ch	side	conversion factor[keV/ch]	a[$\sqrt{\text{keV}}$]	b[keV]	p	δp	l[mm]	δl [mm]
1	L	6.51	2.23	31.3	0.646	0.0042	730	11.9
1	R	6.73	2.07	31.8	0.646	0.0042	730	11.9
2	L	6.54	2.22	36.8	0.589	0.0032	644	10.4
2	R	6.64	2.25	28.8	0.589	0.0032	644	10.4
3	L	5.72	1.85	27.8	0.666	0.0018	519	5.1
3	R	5.54	1.97	22.6	0.666	0.0018	519	5.1
4	L	7.15	2.22	38.8	0.654	0.0053	822	14.8
4	R	7.23	2.18	34.2	0.654	0.0053	822	14.8
5	L	6.34	2.20	33.1	0.721	0.0061	837	15.3
5	R	6.51	2.30	26.7	0.721	0.0061	837	15.3
6	L	6.42	2.28	36.9	0.700	0.0060	862	15.8
6	R	6.62	2.10	26.5	0.700	0.0060	862	15.8
7	L	6.76	2.18	36.6	0.692	0.0066	875	17.6
7	R	6.59	2.30	28.6	0.692	0.0066	875	17.6
8	L	6.55	1.87	44.2	0.634	0.0041	706	11.6
8	R	6.49	2.26	29.2	0.634	0.0041	706	11.6
9	L	5.87	1.89	26.8	0.713	0.0031	636	7.7
9	R	5.93	1.89	24.6	0.713	0.0031	636	7.7
10	L	6.08	1.88	36.9	0.644	0.0021	551	6.3
10	R	6.16	1.92	23.2	0.644	0.0021	551	6.3
11	L	5.71	1.89	26.1	0.693	0.0031	644	8.1
11	R	5.75	1.92	25.2	0.693	0.0031	644	8.1
12	L	6.51	1.99	41.7	0.698	0.0053	825	13.8
12	R	6.59	2.07	25.1	0.698	0.0053	825	13.8
13	L	5.99	1.93	28.9	0.654	0.0024	588	6.8
13	R	5.89	1.89	33.9	0.654	0.0024	588	6.8
14	L	6.16	2.04	34.5	0.700	0.0050	758	12.7
14	R	6.03	2.06	31.2	0.700	0.0050	758	12.7
15	L	5.90	1.87	32.3	0.664	0.0026	586	7.3
15	R	5.91	2.03	26.4	0.664	0.0026	586	7.3
16	L	6.60	2.11	35.8	0.648	0.0038	674	10.9
16	R	6.62	1.93	34.7	0.648	0.0038	674	10.9
17	L	6.19	1.92	32.0	0.682	0.0031	634	8.3
17	R	6.13	1.91	24.4	0.682	0.0031	634	8.3
18	L	6.42	2.10	30.3	0.669	0.0045	758	12.4
18	R	6.59	1.99	33.6	0.669	0.0045	758	12.4

Table 3.3: Parameters determined by the calibration procedure (PANDA36)

ch	side	conversion factor[keV/ch]	a[$\sqrt{\text{keV}}$]	b[keV]	p	δp	l[mm]	δl [mm]
19	L	5.81	2.00	27.0	0.660	0.0029	621	8.2
19	R	5.99	2.17	24.5	0.660	0.0029	621	8.2
20	L	6.08	2.07	29.7	0.678	0.0025	587	6.9
20	R	5.57	1.86	23.6	0.678	0.0025	587	6.9
21	L	6.50	1.99	28.9	0.724	0.0059	831	14.8
21	R	6.16	1.97	24.3	0.724	0.0059	831	14.8
22	L	5.94	1.93	28.1	0.705	0.0043	741	11.0
22	R	6.18	1.99	25.1	0.705	0.0043	741	11.0
23	L	6.42	2.16	30.5	0.728	0.0058	841	14.3
23	R	6.56	2.14	27.5	0.728	0.0058	841	14.3
24	L	4.52	1.48	21.9	0.898	0.0033	714	6.5
24	R	4.42	1.43	17.8	0.898	0.0033	714	6.5
25	L	6.04	1.75	27.5	0.674	0.0029	639	8.3
25	R	6.04	1.87	21.1	0.674	0.0029	639	8.3
26	L	6.34	1.97	27.8	0.752	0.0060	864	14.6
26	R	6.63	2.10	26.5	0.752	0.0060	864	14.6
27	L	5.63	1.97	23.2	0.782	0.0059	805	13.5
27	R	5.88	1.96	22.4	0.782	0.0059	805	13.5
28	L	7.09	1.96	33.0	0.616	0.0051	781	15.1
28	R	7.06	2.13	25.8	0.616	0.0051	781	15.1
29	L	6.07	1.94	27.6	0.703	0.0037	693	9.3
29	R	5.92	2.11	21.9	0.703	0.0037	693	9.3
30	L	7.04	2.10	29.6	0.639	0.0053	777	15.4
30	R	6.73	2.02	26.0	0.639	0.0053	777	15.4
31	L	12.58	2.13	54.1	0.733	0.0119	1083	31.5
31	R	6.94	2.54	29.2	0.733	0.0119	1083	31.5
32	L	8.52	2.02	36.2	0.690	0.0046	758	11.9
32	R	5.95	2.19	25.3	0.690	0.0046	758	11.9
33	L	6.71	2.20	29.2	0.666	0.0053	841	14.4
33	R	8.25	2.20	34.4	0.666	0.0053	841	14.4
34	L	6.79	1.89	31.1	0.695	0.0039	732	10.1
34	R	5.91	2.00	24.8	0.695	0.0039	732	10.1
35	L	6.82	2.14	32.3	0.669	0.0063	880	17.5
35	R	9.13	2.07	31.7	0.669	0.0063	880	17.5
36	L	6.24	1.92	27.9	0.687	0.0034	654	8.8
36	R	8.71	2.09	34.0	0.687	0.0034	654	8.8

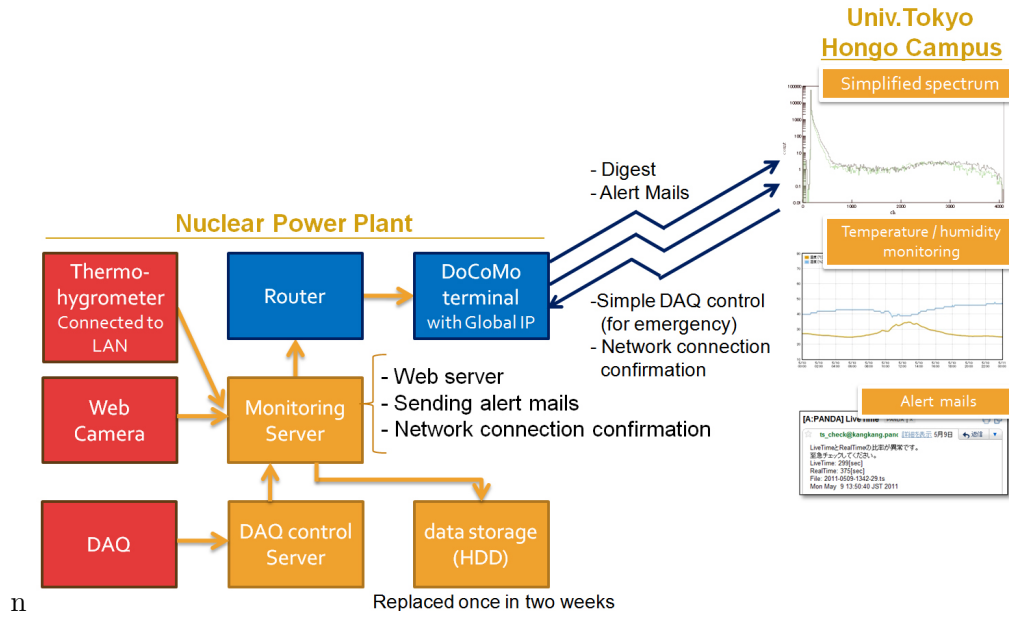


Figure 3.28: Schematic diagram of the data storage and detector monitoring system

3.9 Data storage and detector monitoring system

Figure 3.28 shows the schematic diagram of the data storage and detector monitoring system. There were two servers for DAQ control and monitoring. The data collected by the DAQ system were stored in the DAQ control server. The stored data were then transferred to the other server responsible for the detector monitoring. The monitoring server made the digest information from the data and checked it. The monitoring server had a function to switch off the high voltage supply in any emergent situation. It also collected the information from a thermo-hygrometer (TR-72W; T&D Corporation) and a web camera (CS-WMV04N; Planex Communications Inc.) which were connected to a local area network (LAN) in the van.

The monitoring server checked a number of parameters related to the measurement. In particular, temperature and humidity were important because the van was parked outside the building and subjected to large change in the temperature and the humidity. Each equipment in the van had the requirement for the operating environment and we should check the temperature and humidity were in the required range. Even if the temperature was in the operating range, the QDCs outputs were affected by the temperature. For example, the monitored temperature and humidity are shown in Figure 3.29 and the monitored pedestals are shown in Figure 3.30. Correlated daily modulation can be seen in the temperature and the pedestal values.

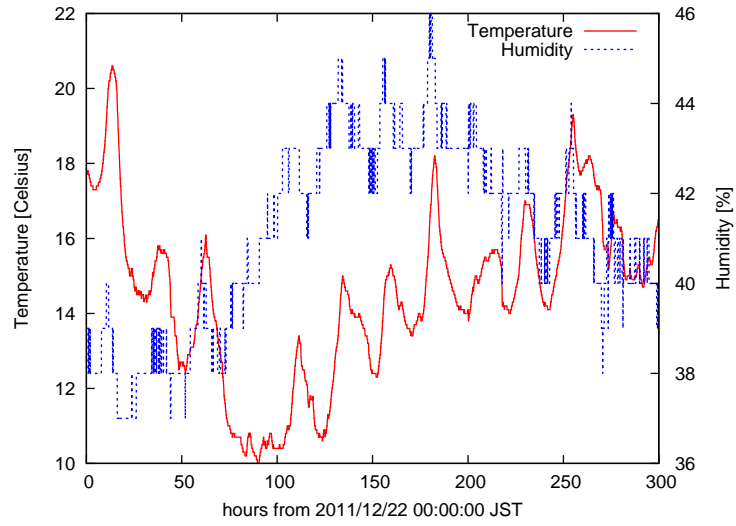


Figure 3.29: Temperature and humidity monitoring (example from PANDA36 data)

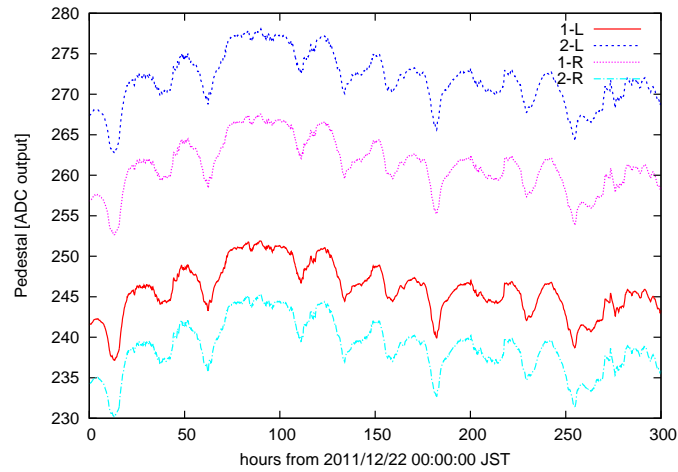


Figure 3.30: Time variation of the pedestal (example from PANDA36 data)

Chapter 4

Radiation enhancements associated with thunderstorms

4.1 Unexpected event-rate increase in PANDA36 data

In the data acquired by the PANDA36 detector through the neutrino detection experiment at Ohi Power Station ($35^{\circ}32'32''\text{N}$, $135^{\circ}39'14''\text{E}$ and about 10 m above the sea level), we found some unexpected increases of event rate. It seems that trigger rate got twice or higher for a few minutes for the events with total energy deposit larger than 3 MeV independently of the reactor operation. To investigate this phenomenon systematically and thoroughly, we checked all the data taken by PANDA36.

First, we simulated the response of the detector to 5 MeV γ -rays isotropically incident on the detector. 5 MeV was chosen because we wanted to omit the effect from ordinary environmental γ -rays (the maximum energy of 2.6 MeV from ^{208}Tl) including fall outs of radioactive radon daughters.

Figure 4.1 shows the simulated response of the PANDA36 detector to 5 MeV γ -rays. The result suggested that the increased amount of 5 MeV γ -rays interacting with the detector infallibly affect the rate of events with total energy deposit on the detector (E_{total}) greater than 4 MeV.

We divided all the observed data into 10 second intervals and calculated rate of events with $E_{\text{total}} > 4\text{ MeV}$ for each interval. The distribution of the rate is shown in Figure 4.2. We searched for and investigated intervals which exceeds threshold denoted by the blue dotted lines in the figure. The threshold was set at 140/sec which is 5 standard deviations away from the average event rate. Intervals which match the following conditions were discarded:

- The door of the van or the container had been opened within two hours. It causes intense temperature change
- No enhancement in adjacent intervals
- Enhancement disappeared after nearest pedestal measurement which means the event-rate increase is due to the drift of the pedestals

As a result, we found three radiation bursts during PANDA36 observation. The date and time, duration and peak event rate are shown in Table 4.1. Temporal variation in the event rate of four energy ranges during the bursts are shown in Figure 4.3–Figure 4.5

Although similar analyses were done with the data taken by Lesser PANDA and PANDA64 in the observations listed in Table 1.1, there was no other excess of event rate.

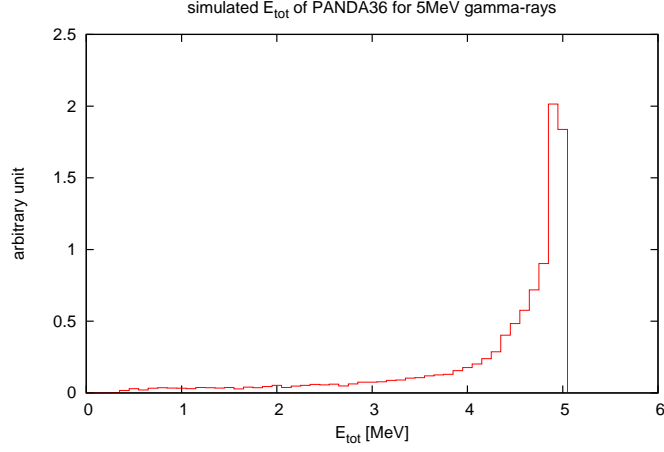


Figure 4.1: Simulated total energy deposit (E_{total}) spectrum in the PANDA36 detector of 5 MeV γ -rays isotropically incident on the detector. Trigger logic described in Section 3.6 was considered.

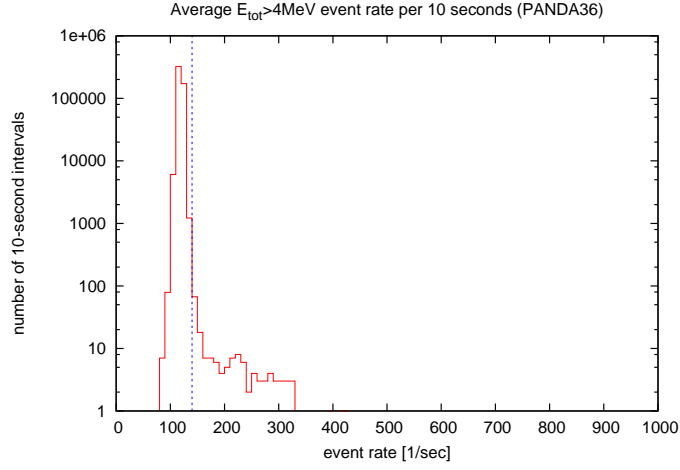


Figure 4.2: Distribution of the rate of the event by PANDA36 which have $E_{\text{tot}} > 4$ MeV. Blue dotted line is the threshold of the detection of high event rate intervals.

Table 4.1: Three radiation burst events. The peak event rate for each burst with the statistical errors are shown.

detector	date and time of the burst	peak event rate ($E_{\text{tot}} > 3$ MeV) [1/sec]
PANDA36	2011 12/25 05:07 JST	$(2.3 \pm 0.1) \times 10^2$
PANDA36	2012 01/02 09:19 JST	$(5.1 \pm 0.1) \times 10^2$
PANDA36	2012 01/05 06:46 JST	$(5.5 \pm 0.1) \times 10^2$

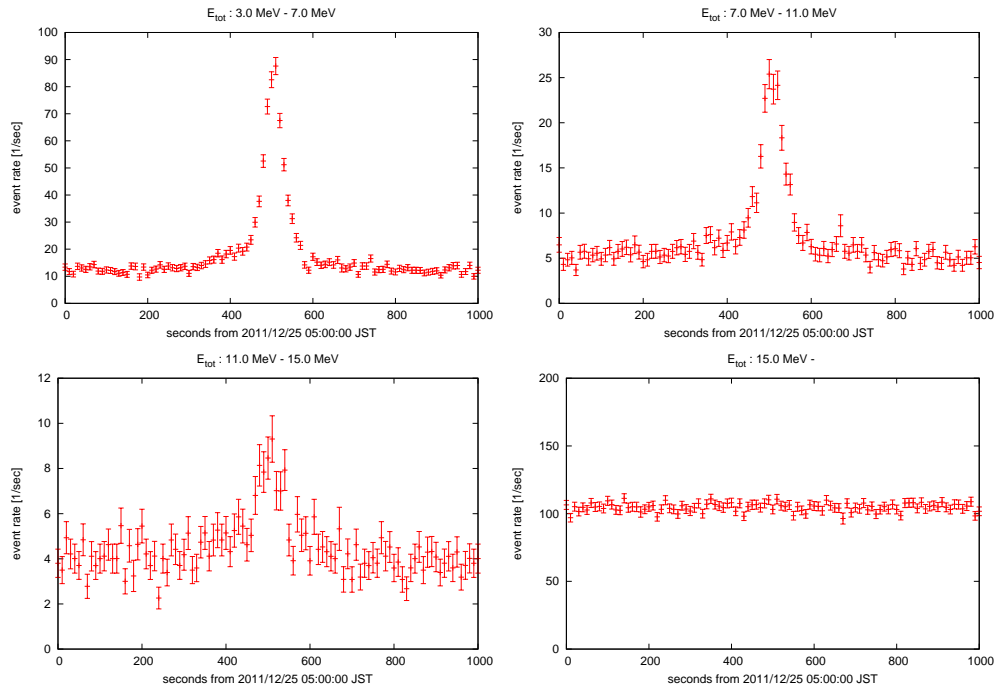


Figure 4.3: Temporal variation in the event rate of the burst event of 2011/12/25

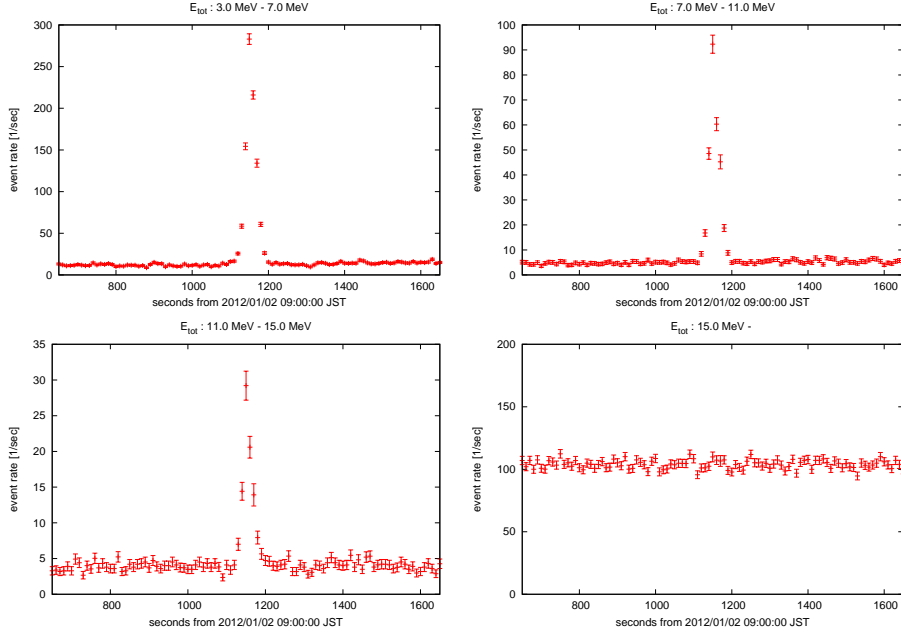


Figure 4.4: Temporal variation in the event rate of the burst event of 2012/01/02

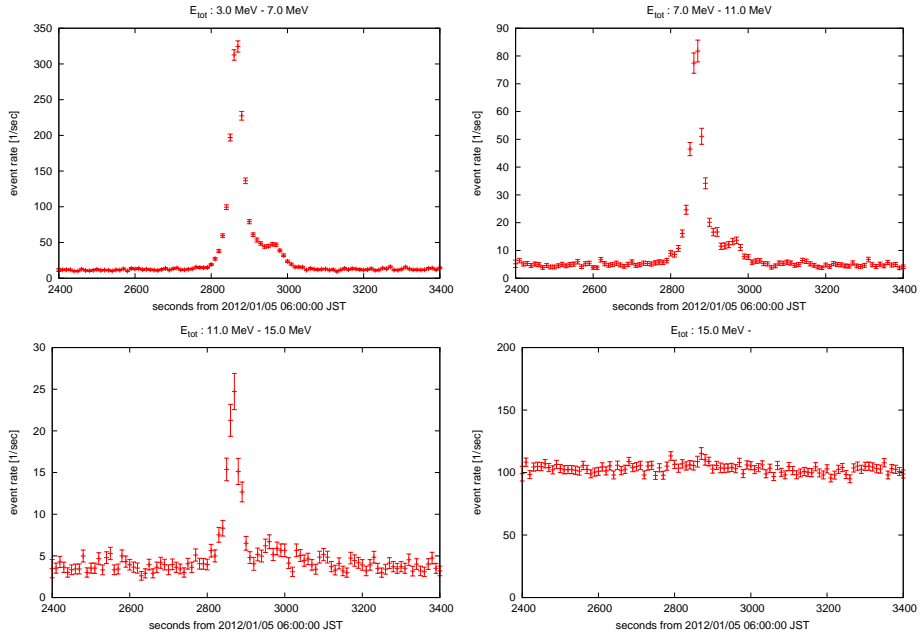


Figure 4.5: Temporal variation in the event rate of the burst event of 2012/01/05

Table 4.2: The meanings of thunder activity levels

level	meaning
0 (no activity)	lightning strike is unlikely to take place
1	There is some lightning strike probability
2	One can see electrical light or hear rolls of thunder. There is high probability of lightning strikes
3	There are some lightning strikes
4	There are many lightning strikes

4.2 Source of the radiation burst

Source candidates of the radiation bursts found in Section 4.1 are followings:

1. cosmic sources such as cosmic gamma-ray bursts or solar flares
2. radio isotopes
3. thunderstorms

There was no record of observed cosmic gamma-ray burst (GRB) data by satellite experiments [60] when the PANDA36 detector observed the radiation bursts. If any cosmic events including cosmic GRBs caused the radiation bursts at sea-level, the effect of the events were hardly limited to the local region but it could be observed on global scale. We therefore investigated the logs of air dose-rate monitors provided by Division for Environment, Health and Safety, the University of Tokyo. The monitors were installed in the Hongo Campus and the Komaba Campus of the University of Tokyo (both are more than 350 km away from Ohi Power Station). There was no air dose rate increase which corresponds to the radiation bursts observed by PANDA36.

Next, natural or artificial radio isotopes are unlikely to be the source of the bursts since the energy spectra of the bursts (we will show them in Section 4.3) extends over 10 MeV, which are too large to be emitted by nuclear energy-level transition. Moreover, the broad feature of the spectrum denies the direct contribution of radio-isotopes which emit γ -rays with specific energies.

At last, we considered the association between thunderclouds and the radiation bursts. Although we did not install any electric-field monitor or light and sound sensors by ourselves, we can know brief information about thunder activity around the PANDA36 detector via “Thunder Nowcast” provided by Japan Meteorological Agency. Thunder Nowcast provides the thunder activity information analyzed from lightning discharges detected by Lightning Detection Network System (LIDEN) and radar observations for every ~ 1 km grid [61]. The degree of thunder activity is represented by five levels. The meaning of each level is listed in Table 4.2.

Figure 4.6–4.8 are the Thunder Nowcast data around Ohi Power Station at almost the same time that the radiation bursts have been observed. The data show that there were more than one grid whose thunder activity level of 3 or higher around the experimental site for all three bursts. Consequently, we concluded that the radiation bursts we observed by the PANDA36 detector were related to thunderstorms and were presumably bremsstrahlung γ -rays emitted through the RREA mechanism described in Section 1.2.

High thunder activity is, however, not the sufficient condition for radiation burst. We searched through the Thunder Nowcast data corresponding to Lesser PANDA, PANDA36 and PANDA64 experiments to find data which have thunder activity level larger than two in 20×20 grids around the detector. As a result, there were 8, 22 and 18 time-consecutive data sets which meet the condition for Lesser PANDA, PANDA36 and PANDA64 respectively; nevertheless radiation bursts are observed only three times which we show in Section 4.1. For example,

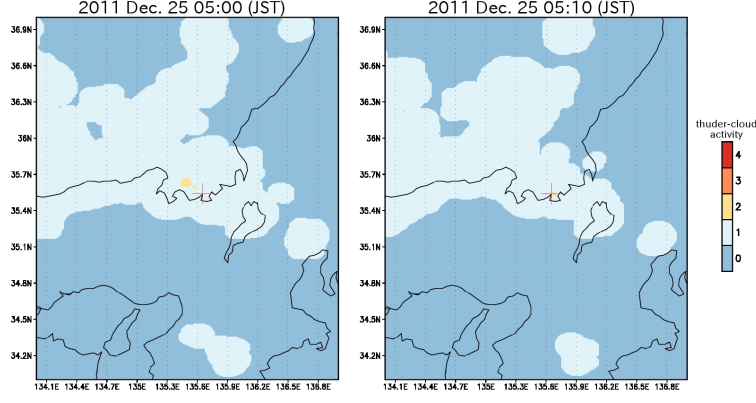


Figure 4.6: Thunder Nowcast of 05:00 and 05:10, December 25th, 2011 JST. The red cross shows the location of Ohi Power Station, which stand at the southeastern coastal area of the Japan Sea. Colors on the map show the degree of the thunder activities.

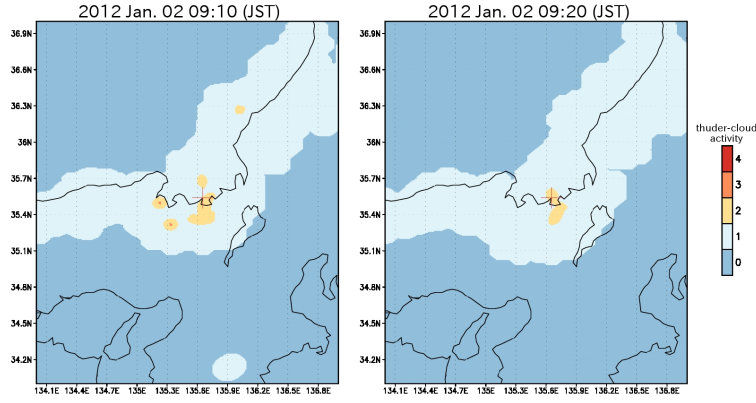


Figure 4.7: Thunder Nowcast of 09:10 and 09:20, January 2th, 2012 JST.

the Thunder Nowcast data of 19:50 and 20:00, January 4th, 2012 JST is shown in Figure 4.9, in which we can see high thunder-activity region around the experimental site. Corresponding event rate variation are shown Figure 4.10, which have no increase.

4.3 Energy of the bursts

Figure 4.11 shows typical event rate distribution of $E_{\text{total}} > 4 \text{ MeV}$ when there were no bursts recorded by PANDA36. It well fits the Gaussian distribution with average 118.5/sec and standard deviation $\sigma = 3.79/\text{sec}$. We chose 10 seconds intervals whose event rates are greater than $118.5/\text{sec} + 5\sigma = 137/\text{sec}$ around the bursts found in Section 4.1 and defined them as burst periods. The list of the burst periods are shown in Table 4.3. We call each of the burst period by name defined in Table 4.3 in the following description.

E_{total} spectra in burst periods, background and background subtracted spectra are shown in Figure 4.12–4.14. Here each background spectrum is based on summation of 10 minutes data 13 minutes before the burst period and 10 minutes data 3 minutes after the burst period. Each spectrum was normalized by live time. All three bursts have energy spectra extending to about 15 MeV. And we see from Figure 4.3–4.5 in Section 4.1 that there is no difference in the temporal structure among three (3.0–7.0 MeV, 7.0–11.0 MeV, 11.0–15.0 MeV) energy ranges.

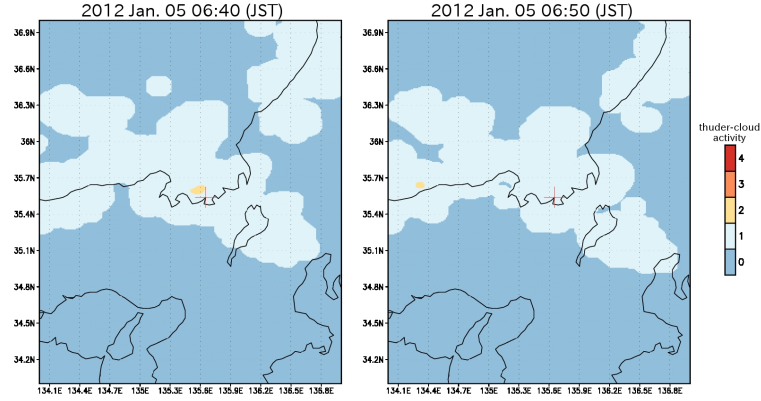


Figure 4.8: Thunder Nowcast of 06:40 and 06:50, January 5th, 2012 JST.

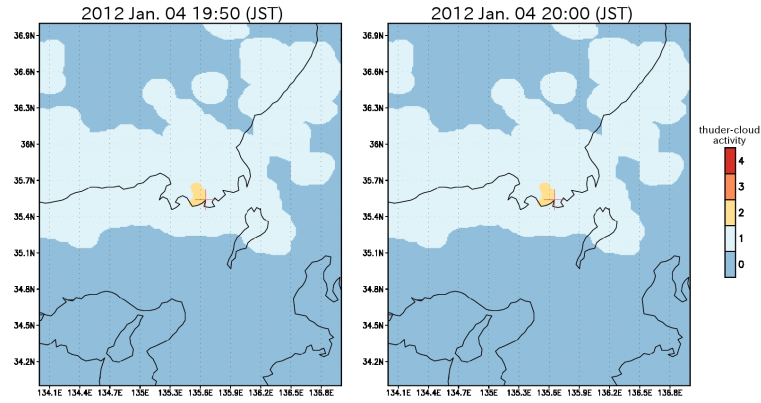


Figure 4.9: Thunder Nowcast of 19:50 and 20:00, January 4th, 2012 JST. At this time, the thunder activity level above the detector was two, though increase in event rate was not observed by the PANDA36 detector as shown in Figure 4.10.

Table 4.3: List of the burst periods

burst name	date time(JST)	duration [sec]
burst-20111225	Dec. 25, 2011 5:7:40-5:9:10	90
burst-20120102	Jan. 2, 2012 9:18:50-9:19:50	60
burst-20120105	Jan. 5, 2012 6:47:00-6:50:00	180

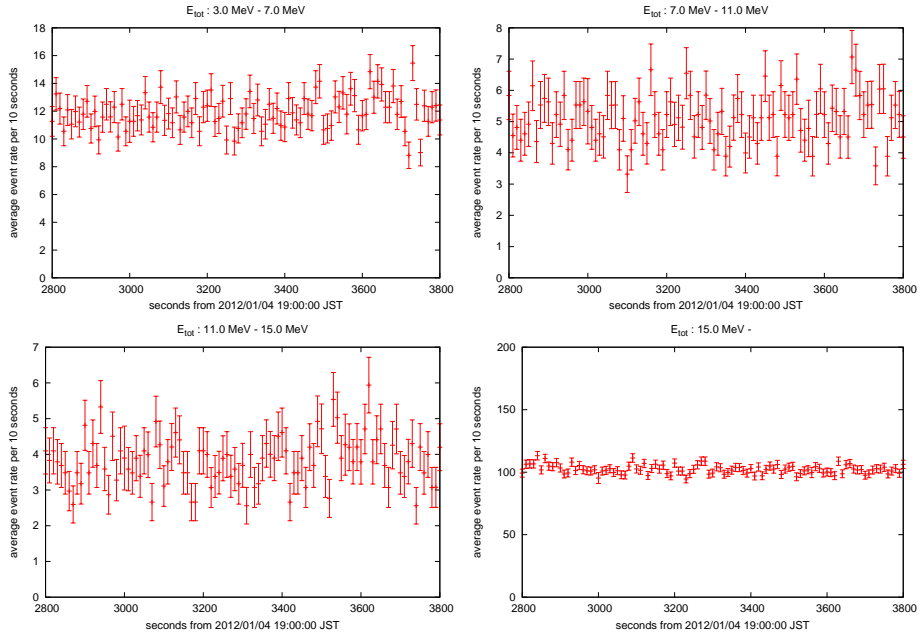


Figure 4.10: Temporal variation in the event rate from 19:46:20, January 4th, 2012, when the thunder clouds are assumed to be above the detector

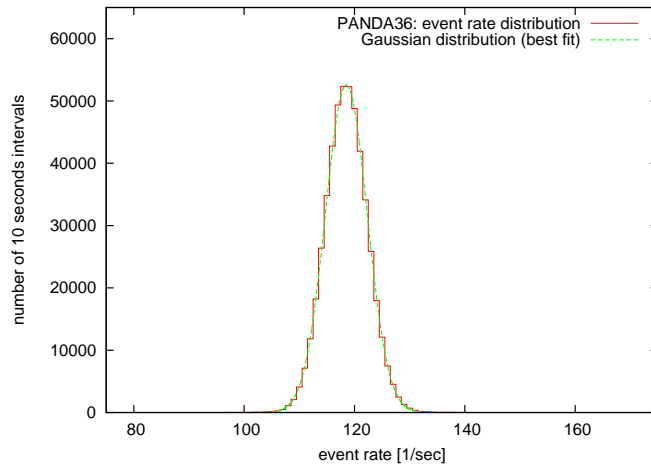


Figure 4.11: Event rate distribution of $E_{\text{total}} > 4 \text{ MeV}$ when there were no bursts recorded by PANDA36

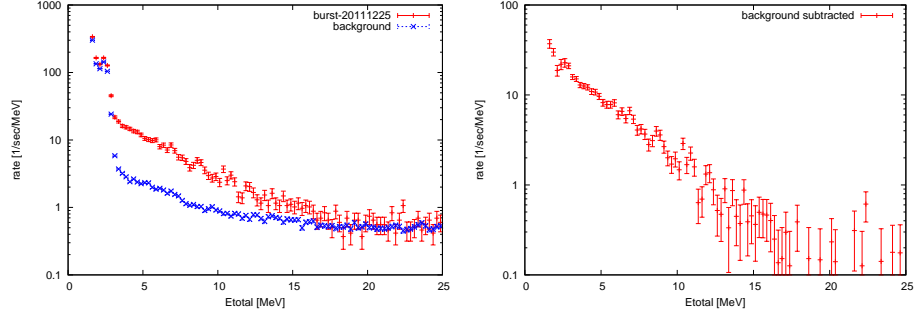


Figure 4.12: burst-20111225: (left) E_{total} spectrum of the burst period and the background period. (right) E_{total} spectrum of the burst period with background subtraction. The error bars show the statistical errors.

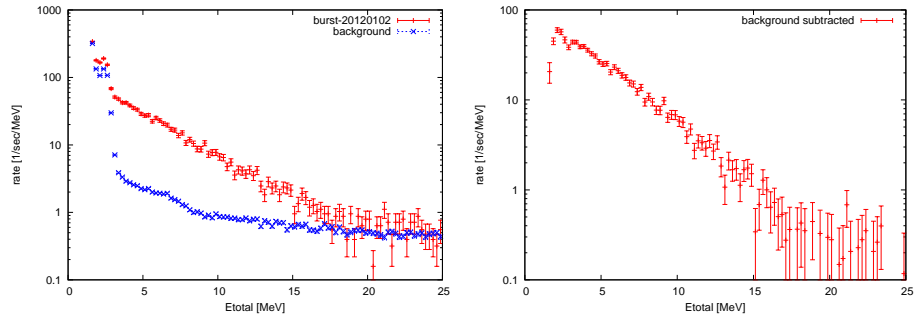


Figure 4.13: burst-20120102: Same as Figure 4.12

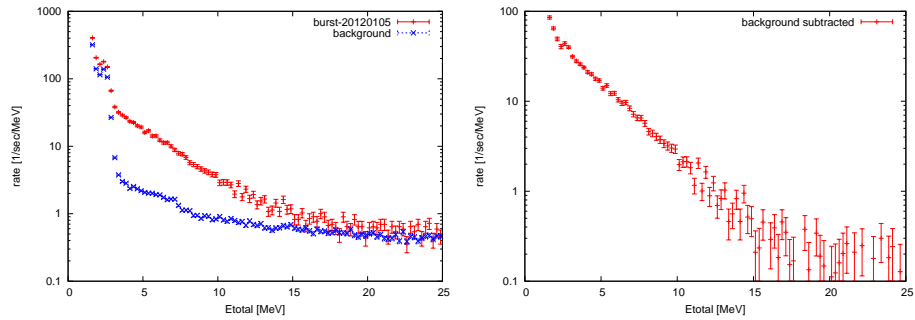


Figure 4.14: burst-20120105: Same as Figure 4.12

4.4 Variation of the hit multiplicities

We investigated the variation of the number of fired modules (hit multiplicities). The number of modules which had energy deposit more than 150 keV were counted for each triggered event in the burst periods and the background periods. The result is shown in Figure 4.15–4.17.

While the rate of high-multiplicity events which are due to high-energy muon does not change, the rate of low-multiplicity events largely increases during the bursts. The fact also indicates that main component of the bursts are γ -rays.

4.5 Monte Carlo analysis of γ -rays emitted by accelerated electrons

We performed Monte Carlo simulations to estimate the energy and the height of the bremsstrahlung source electrons. The simulations were made by Geant4 toolkit [59], which is widely used Monte Carlo toolkit for particle transport simulations.

First, we assumed, for simplicity, that the radiation bursts we observed were bremsstrahlung γ -rays from mono-energetic electrons. As we have shown in Figure 1.2 and 1.3 in Section 1.2, when the acceleration region in the thunder cloud is long enough, accelerated electrons reach the energy of acceleration limit quickly, and bremsstrahlung is dominantly emitted by those high energy electrons. Consequently, it is a good approximation to assume that the bremsstrahlung γ -rays are emitted by mono-energetic electrons.

At first, electrons were projected vertically downward from height h with energy E in a $2\text{ km} \times 2\text{ km} \times 2\text{ km}$ space filled with air (Figure 4.18). Height h was changed from 100 m to 1500 m with a step of 100 m and energy E was changed from 10 MeV to 36 MeV with a step of 2 MeV. Then we have number, spectrum and position distribution of photons at ground level. At this time, we assumed that the air was under STP condition and uniform. Decrease of pressure by height is negligible for the present rough estimation because the pressure at 1,500-m altitude is about 0.84 of 0 m.

Figure 4.19 shows the number of γ -ray photons reached the ground per one electron shot. Considering the accuracy of the particle track simulation and actual observation, photons which had energy larger than 1.5 MeV were counted. The number of photons at the ground level decreases exponentially with source height.

The spectra at the ground level of photons emitted by 10 MeV, 20 MeV and 30 MeV electrons projected downward from 100 m, 600 m and 1100 m altitude are shown in Figure 4.20. And the distances of landing point from point just below the projection is plotted in Figure 4.21.

As a next step, we calculated the detector response to those γ -rays by second Monte Carlo simulations by Geant4. The PANDA36 detector and supporting materials are included in the simulation geometry. Building walls and land surface were ignored since those have little impact when we consider the γ -rays from the sky. γ -rays were shot downward from random point just above the PANDA36 detector (Figure 4.22) with energy spectra obtained from the previous simulations. Particle tracks and energy deposits in the detector and the resolution of each module are considered in this simulation.

The results were compared to the background subtracted energy spectrum of each burst shown in Figure 4.12–4.14. χ^2/dof for each burst are calculated using energy bins from 3 MeV to 30 MeV. In calculating χ^2 , the number of events in a bin of all the energy spectra, the burst, the background and the simulation, is required to be not less than ten. The bins are otherwise not used in the calculation because of the low statistics. The event rate of each simulation result was left free to minimize χ^2/dof so that the χ^2/dof represent the parameter goodness in term of shape of the spectrum.

χ^2/dof for each electron energy (E_e) and projection height (h) is shown in Figure 4.23–4.25. It gets minimum at $E_e = 16\text{ MeV}$, $h = 1100\text{ m}$ for burst-20111225 ($\chi^2/\text{dof} = 0.96$) and burst-

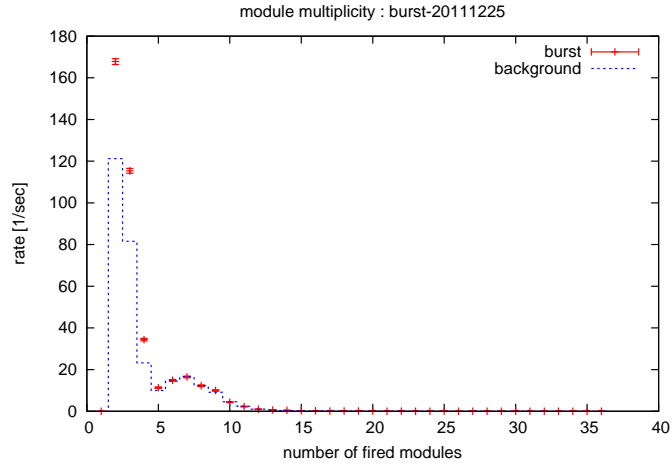


Figure 4.15: The event rate for each multiplicity during burst-20111225 (red plot) and corresponding background period (blue dotted line). The rate of the events with only 1 fired module is suppressed to zero because of the trigger condition of the PANDA36 detector.

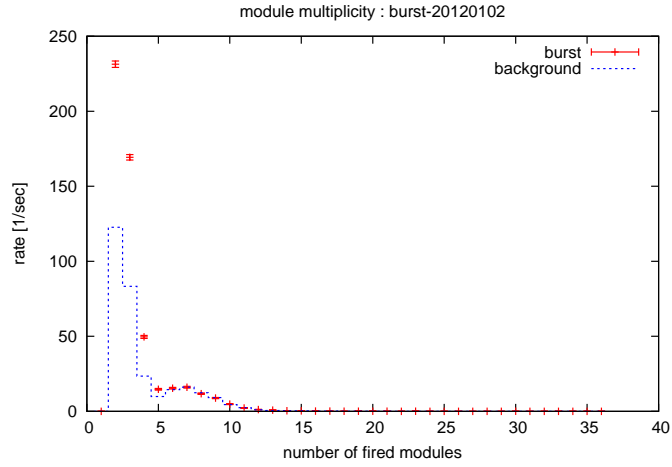


Figure 4.16: burst-20120102: Same as Figure 4.16

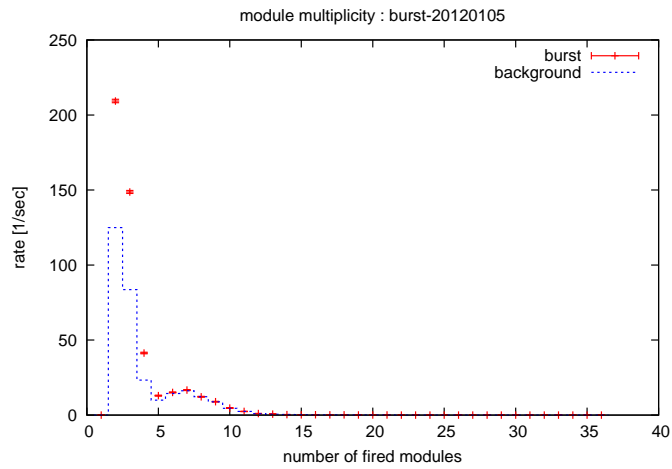


Figure 4.17: burst-20120105: Same as Figure 4.16

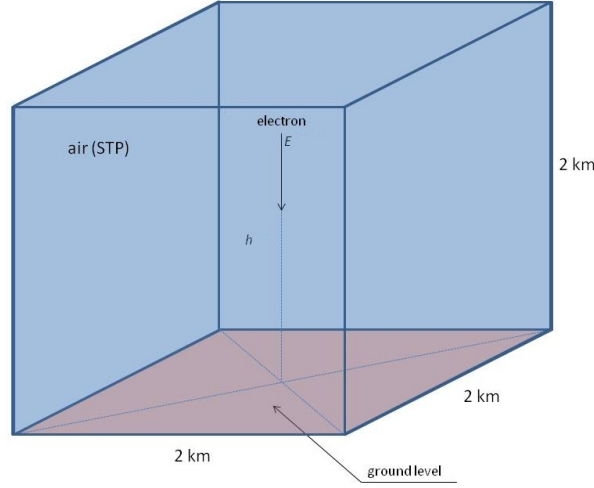


Figure 4.18: In the first simulation, electrons are shot from height h with energy E in a $2\text{ km} \times 2\text{ km} \times 2\text{ km}$ space filled with air.

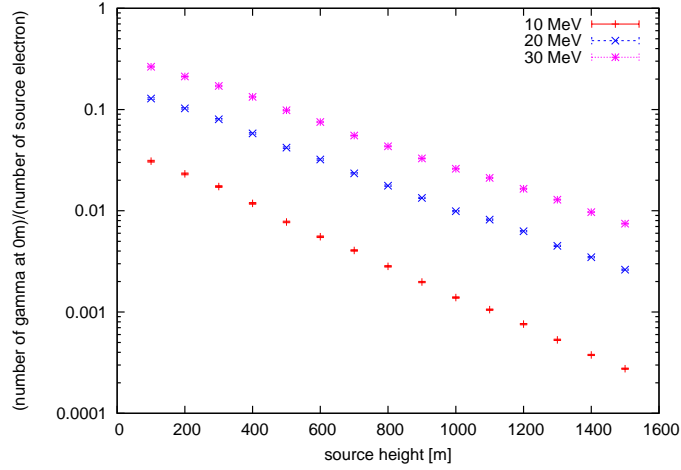


Figure 4.19: Number of bremsstrahlung photons which reached the ground for each height and energy of the source electrons calculated by the Monte Carlo method

20120102 ($\chi^2/\text{dof} = 0.87$). It gets minimum at $E_e = 16\text{ MeV}$, $h = 400\text{ m}$ for burst-20120105 ($\chi^2/\text{dof} = 0.82$). The simulation spectra at minimum χ^2/dof are shown in Figure 4.26–4.28. The simulations well reproduce the measured energy spectra in the energy region up to 13 MeV . In the high energy region above 13 MeV , the agreement between the simulations and the measurements look rather poor, but it might be due to the low statistics of the simulations, the burst events and the background events. We will come back to this point later again. As you can see in the χ^2/dof plots, small χ^2/dof regions have long shapes in the height direction. So we could estimate the energy of the accelerated electrons by the simulations but the heights are left with some ambiguities.

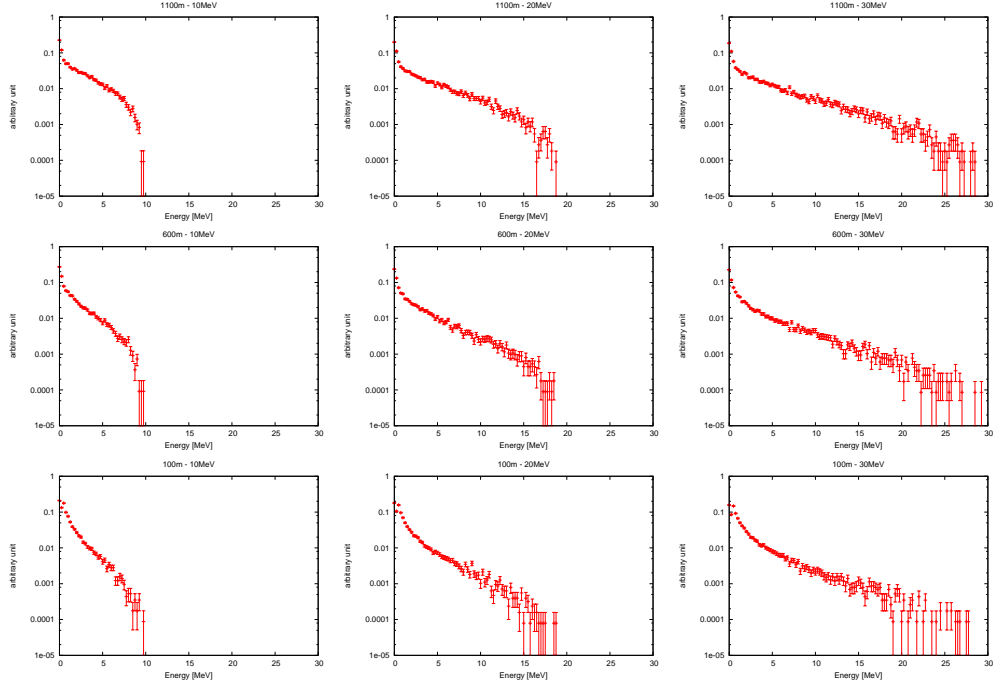


Figure 4.20: Simulated spectrum of bremsstrahlung γ -rays emitted by 10 MeV (left), 20 MeV (middle) and 30 MeV (right) electrons shot from 100 (bottom), 600 m (middle) and 1100 m (top)

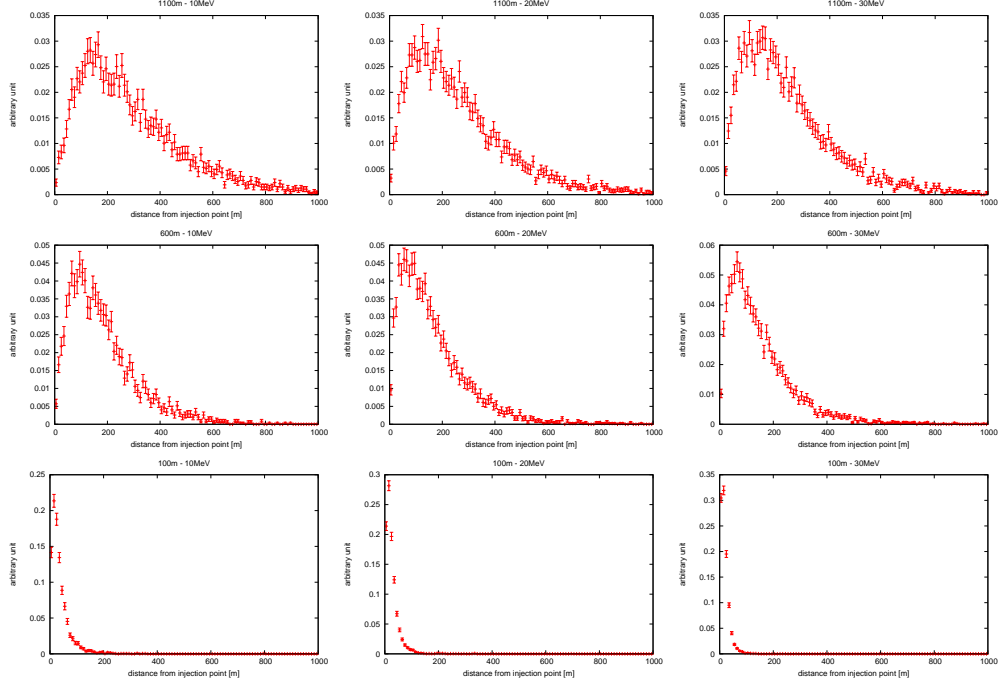


Figure 4.21: Simulated position distribution of bremsstrahlung γ -rays emitted by 10 MeV (left), 20 MeV (middle) and 30 MeV (right) electrons shot from 100 (bottom), 600 m (middle) and 1100 m (top). The distances of landing point of photon from point just below the projection.

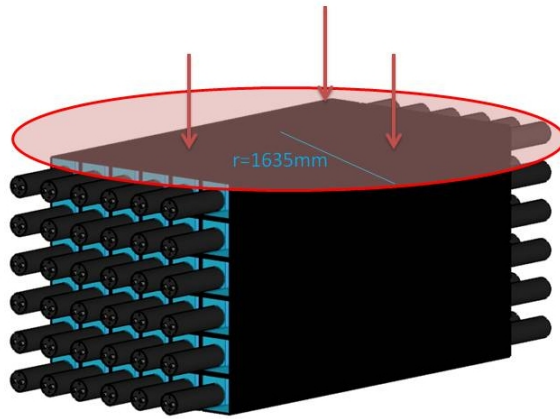


Figure 4.22: In the second simulation, γ -rays are shot from random point in a circle above the detector. The circle is large enough to cover whole detector.

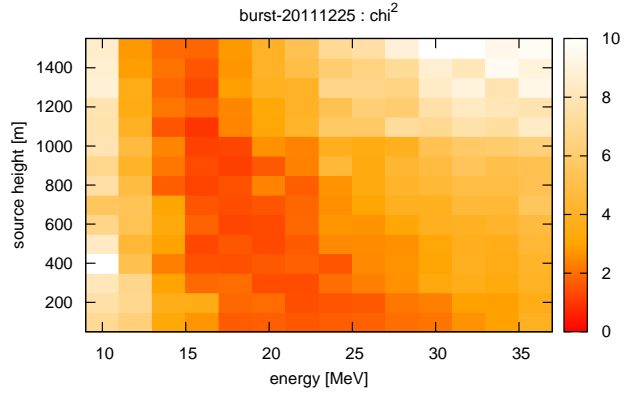


Figure 4.23: burst-20111225: χ^2/dof calculated by comparing observed data and bremsstrahlung photon emitted by electron shot from the sky

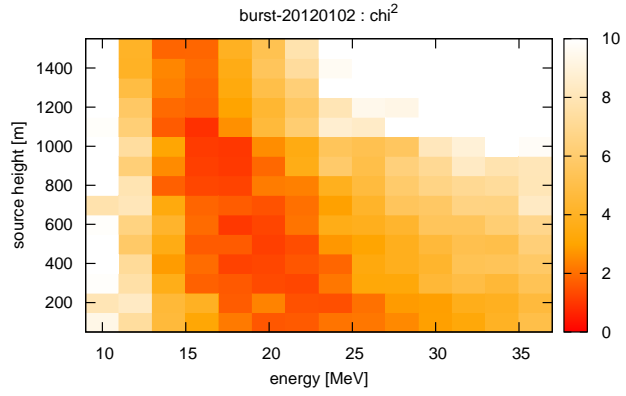


Figure 4.24: burst-20120102: Same as Figure 4.23

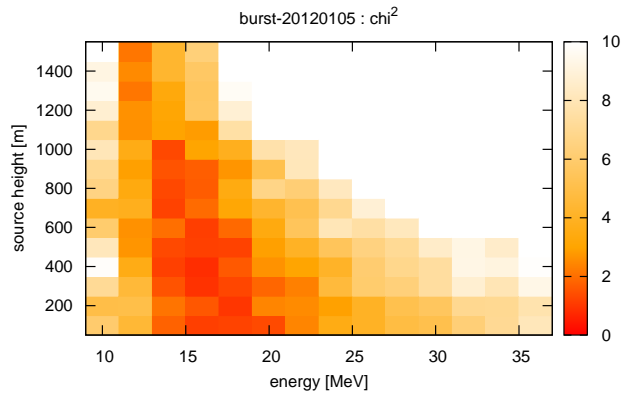


Figure 4.25: burst-20120105: Same as Figure 4.23

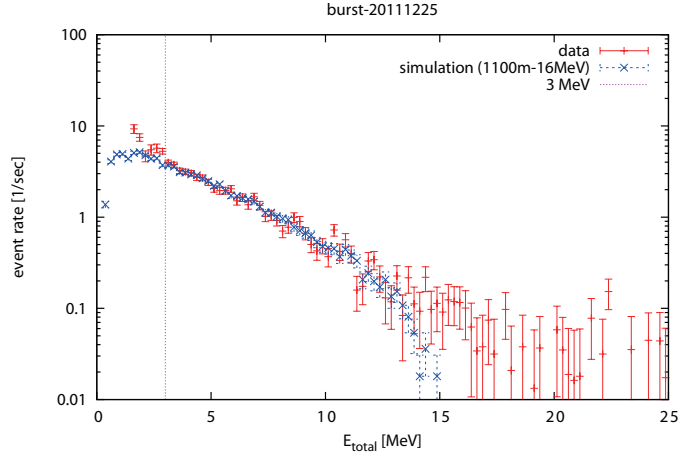


Figure 4.26: Simulated spectrum of E_{total} by electron shot from 1100 m with 16 MeV, which matches the burst-20111225 spectrum the best. For both simulated and measured spectra, the error bars show the statistical error.

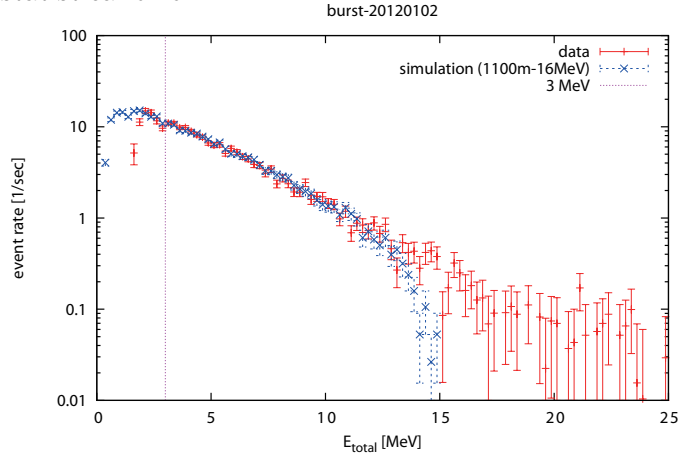


Figure 4.27: Same as Figure 4.26, but for E_{total} by electron shot from 1100 m with 16 MeV, which matches the burst-20120102 spectrum the best

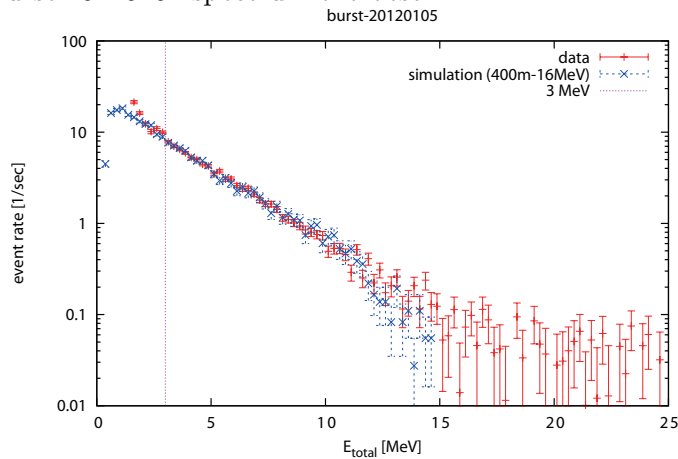


Figure 4.28: Same as Figure 4.26, but for E_{total} by electron shot from 400 m with 16 MeV, which matches the burst-20120102 spectrum the best

The simulation spectra of bremsstrahlung γ -rays from mono-energetic electrons shown in Figure 4.26–4.28 fit well with the observation results. However, there are some difference in the high-energy region. To address this problem, we introduced models with which accelerated electrons in the sky have certain energy distributions.

At first, we simulated the numbers and spectra of bremsstrahlung photons at the ground level from mono-energetic electrons projected vertically downward from the sky with the same setup and procedure described previously. Height was changed among 100 m, 500 m, 900 m and 1300 m and energy was changed among 17 MeV, 23 MeV, 29 MeV and 35 MeV. The altitude of the detector was assumed to be 0 m. Then we calculated the detector response to those γ -rays. Low-energy electron components were ignored because attenuation of low-energy electrons and bremsstrahlung γ -ray was too large in the air and would be inappropriate to the quantitative discussion.

Next, we calculated the weighted sum of E_{1st} spectra of the detector responses to the simulated bremsstrahlung γ -rays from four energies of electrons projected from the same height ($S_{sim,17MeV}(E)$, $S_{sim,23MeV}(E)$, $S_{sim,29MeV}(E)$ and $S_{sim,35MeV}(E)$) as following equation.

$$\begin{aligned} S_{sim}(E) \equiv & a_{17MeV} S_{sim,17MeV}(E) + a_{23MeV} S_{sim,23MeV}(E) \\ & + a_{29MeV} S_{sim,29MeV}(E) + a_{35MeV} S_{sim,35MeV}(E) \end{aligned} \quad (4.1)$$

Here, a_{17MeV} , a_{23MeV} , a_{29MeV} and a_{35MeV} are the contribution factors of each energy of electron.

The spectra calculated by equation 4.1 were compared to the background subtracted energy spectra of each burst and we fitted the contribution factors to minimize the χ^2 for each projection height. Same analysis were done for all the three bursts and the fit results with the contribution factors and height which minimize χ^2/dof are shown in Figure 4.29–4.31.

Using the factor $a_{17MeV} \sim a_{35MeV}$ and the simulated number of bremsstrahlung γ -ray photons for each electron energy, electron spectra at the projection heights were estimated. Those are shown in Figure 4.32–4.34 with the fitted E_{total} spectra showing the fraction of the contribution of each electron energy bin.

The result shows that the differences at high-energy regions were reduced only slightly by this approach and still remains. But the Figure 4.32–4.34 indicate that the E_{total} spectra at the burst on the ground can be explained by accelerated electrons in small energy range at the projection height and the assumption that the projected electron has mono-energy was not so unreasonable.

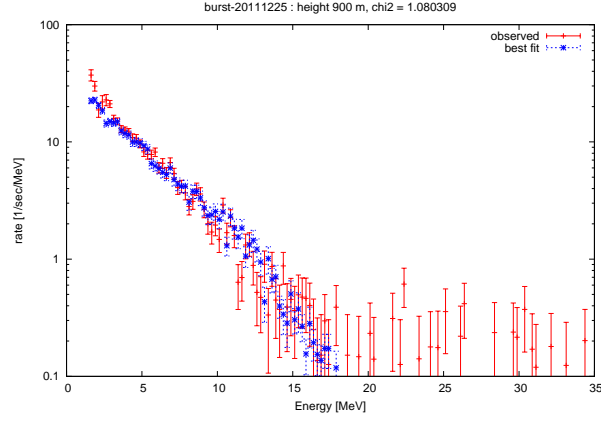


Figure 4.29: Simulated spectrum of E_{total} from electrons shot from 900 m with energy spectrum which matches the burst-20111225 spectrum the best. The spectrum of the electron at the shot height was divided into four bins (17 MeV, 23 MeV, 29 MeV and 35 MeV). For both simulated and measured spectra, the error bars show the statistical error

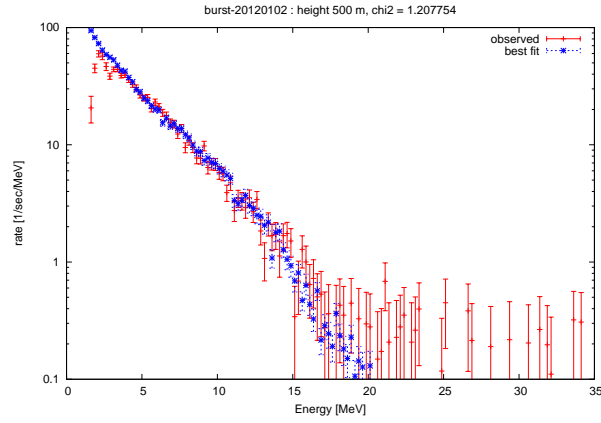


Figure 4.30: The same plot as Figure 4.29 but for burst-20120102 (electrons were shot from 500m height)

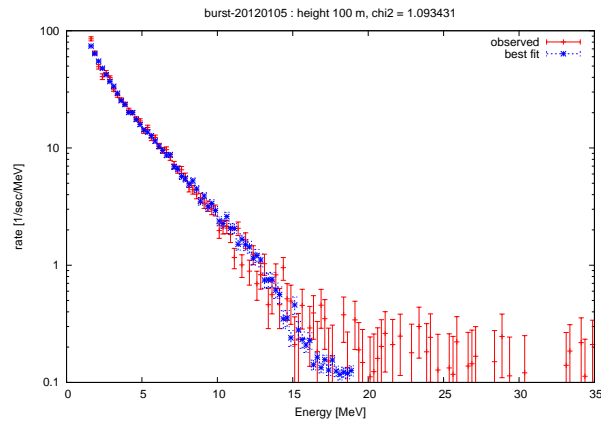


Figure 4.31: The same plot as Figure 4.29 but for burst-20120105 (electron were shot from 100m height)

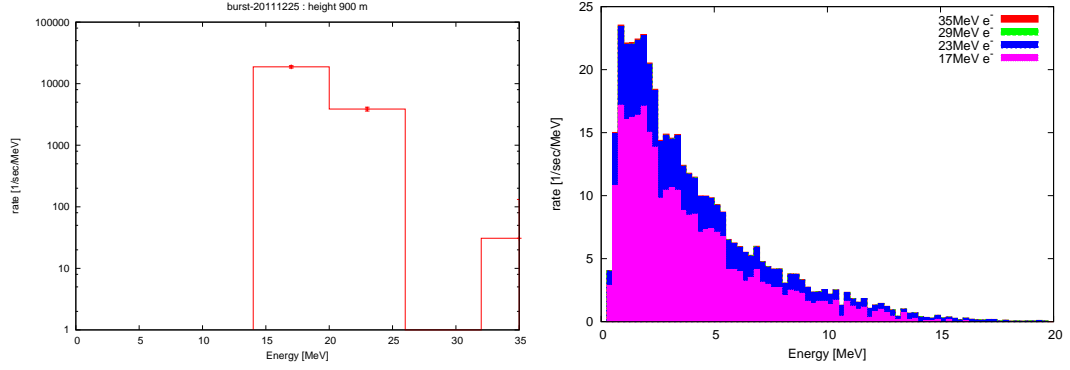


Figure 4.32: (left) Estimated electron spectrum at the projection height with statistical errors (right) Fitted energy spectra showing the fraction of the contribution of each electron energy bin by colors

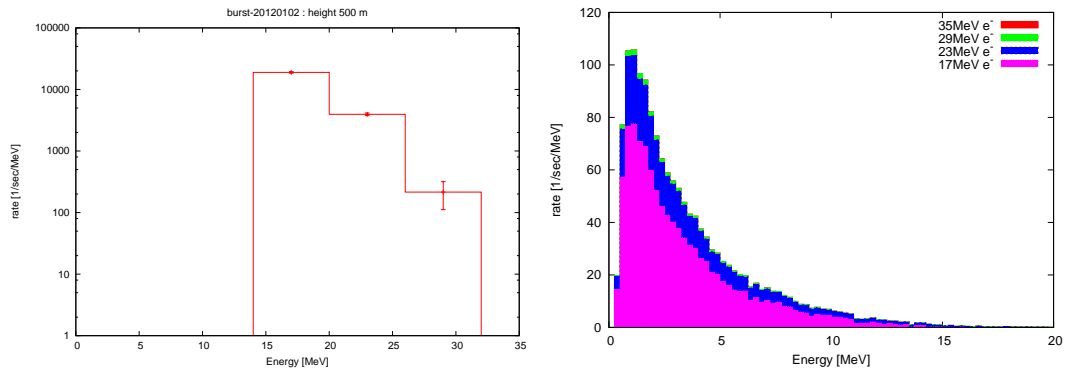


Figure 4.33: The same plot as Figure 4.32 but for burst-20120102

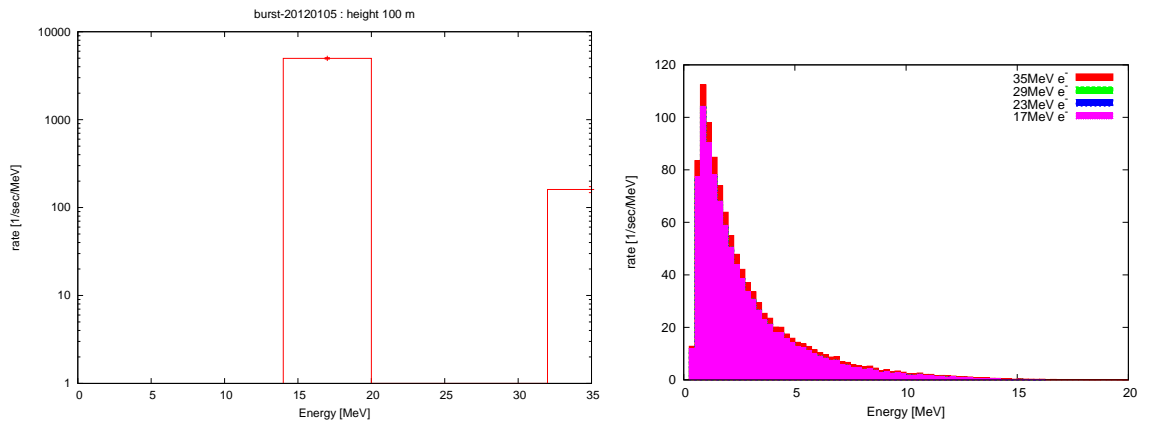


Figure 4.34: The same plot as Figure 4.32 but for burst-20120105

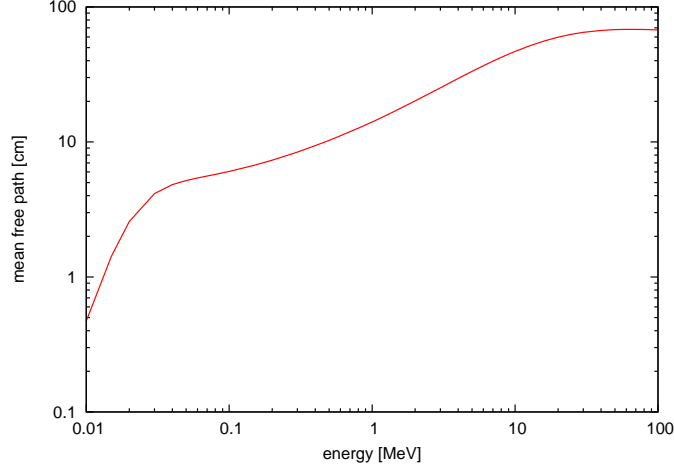


Figure 4.35: Mean free path of γ -ray in the plastic scintillator [62]

4.6 Arrival direction of γ -rays

The PANDA36 detector has the segmented structure and as mentioned in Section 3.5, the light intensity ratio seen by two PMTs on both ends of the module allows one to estimate the position of the energy deposit along the module. We took advantage of this position information to investigate arrival direction of γ -rays during the burst periods.

4.6.1 Arrival direction analysis by maximum energy-deposit position

Mean free path of γ -rays in the plastic scintillator is shown in Figure 4.35. Since it is in order of 10 cm for $O(1) - O(10)$ MeV, if γ -rays arrived at the detector from particular direction, it is highly probable that the positions of energy deposit by those γ -rays on the detector distribute on the modules facing the γ -ray arrival direction.

At first, we made Monte Carlo simulations to know the detector response for γ -rays isotropically incident on the detector. The energy spectra of the incident γ -rays were the spectra of bremsstrahlung photons at the ground level whose χ^2/dof were smallest in the analysis of Section 4.5 for each burst.

Then we investigated energy deposit on each module for each triggered event and recorded the module on which energy deposit was the largest of all the modules ($E_{1\text{st}}$). The frequency of the energy deposit to be $E_{1\text{st}}$ for each module is calculated using events with $E_{\text{total}} \geq 1.5$ MeV for the observed data in the burst periods and background periods, and the simulation.

At last, following calculation was made for each module

$$N_i = (N_{i,\text{burst}} - N_{i,\text{bg}})/(N_{i,\text{sim}}). \quad (4.2)$$

Here i is the module number, $N_{i,\text{burst}}$, $N_{i,\text{bg}}$ and $N_{i,\text{sim}}$ are the rates to be $E_{1\text{st}}$ in the burst period, the background period and the simulation respectively. $N_{i,\text{sim}}$ is normalized by average rate of 16 modules in center to be 1. Used $N_{i,\text{sim}}$ s are shown in Figure 4.36–4.38. Inner sixteen modules were more likely to get $E_{1\text{st}}$ than outer twenty modules because the trigger condition uses only inner modules. N_i values for each burst are shown in Figure 4.39–4.41. And its temporal variations are shown in Figure 4.42–4.44.

As a result, we found for all the three bursts, the γ -rays were incident on the detector from upside of the detector obviously.

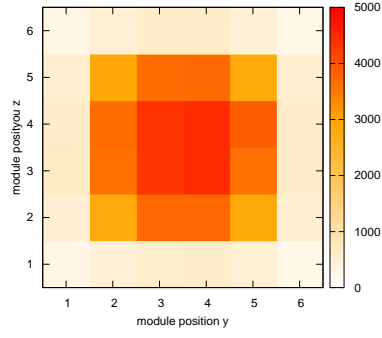


Figure 4.36: Simulated E_{1st} distribution by γ -rays isotropically incident on the detector. Simulated energy spectrum of bremsstrahlung γ -rays of burst-2011225 calculated in Section 4.5 was used.

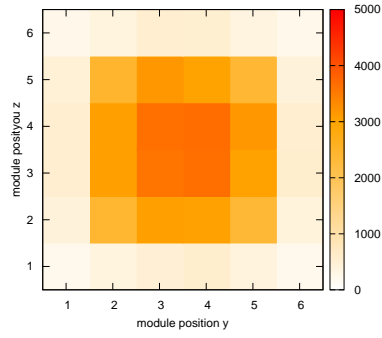


Figure 4.37: Same as Figure 4.36, but used γ -ray spectrum was bremsstrahlung spectrum of burst-20120102

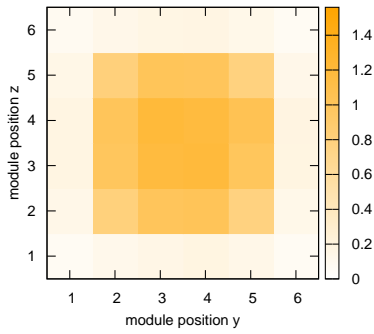


Figure 4.38: Same as Figure 4.36, but used γ -ray spectrum was bremsstrahlung spectrum of burst-20120105

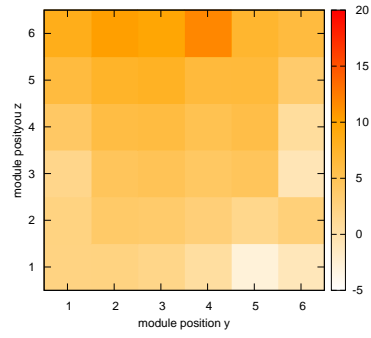


Figure 4.39: burst-20111225: E_{1st} distribution

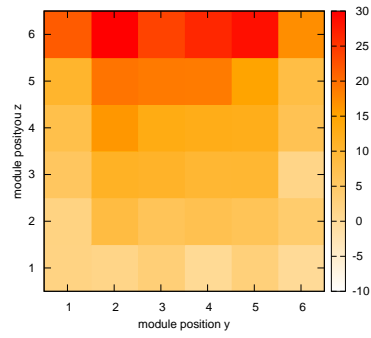


Figure 4.40: burst-20120102: E_{1st} distribution

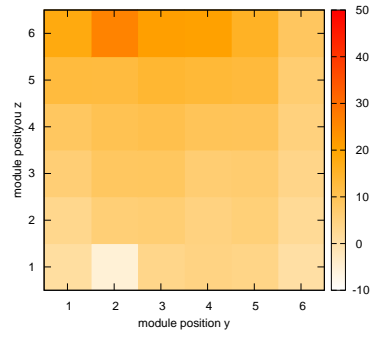


Figure 4.41: burst-20120105: E_{1st} distribution

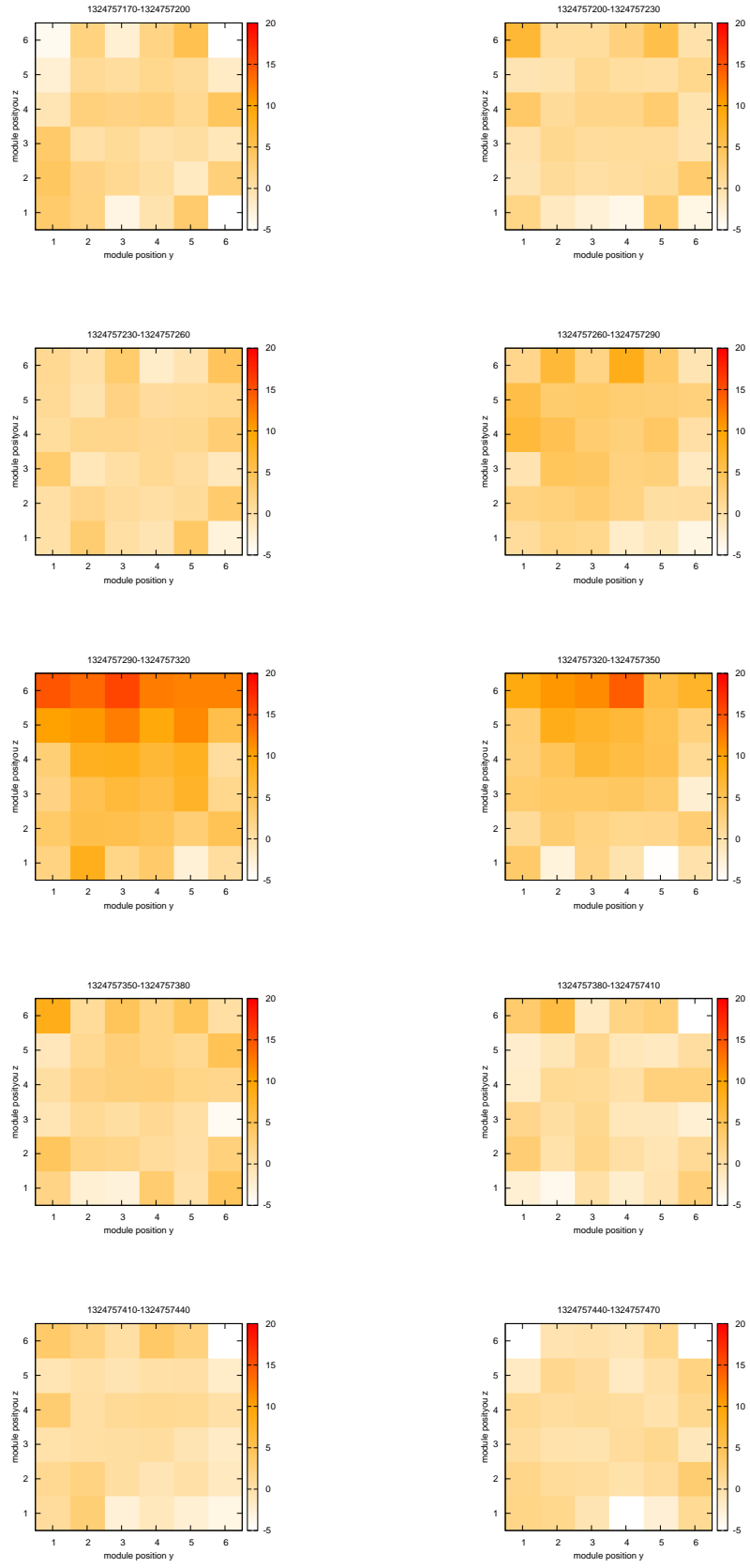


Figure 4.42: Temporal variation of E_{1st} distribution around burst-20111225

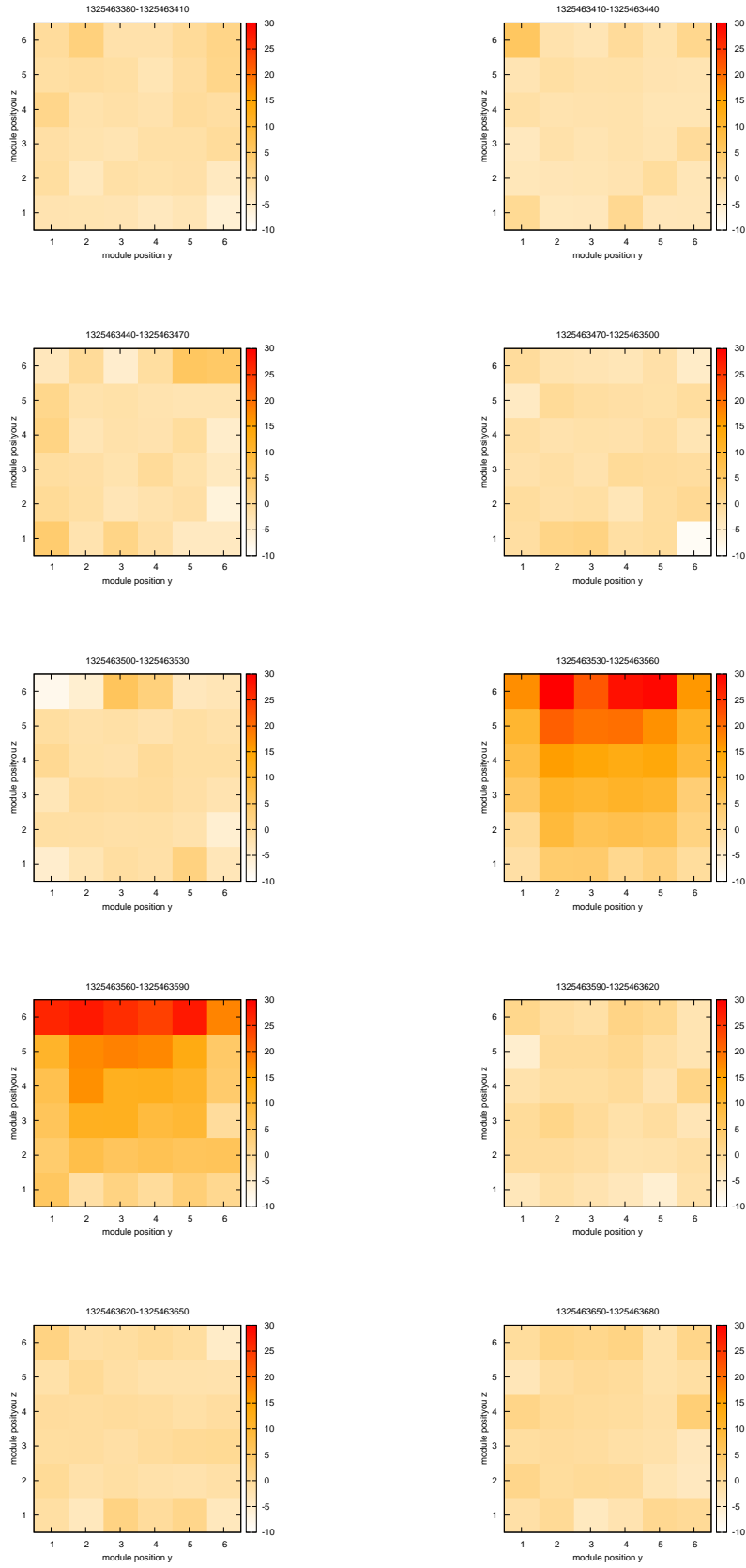


Figure 4.43: Temporal variation of E_{1st} distribution around burst-20120102

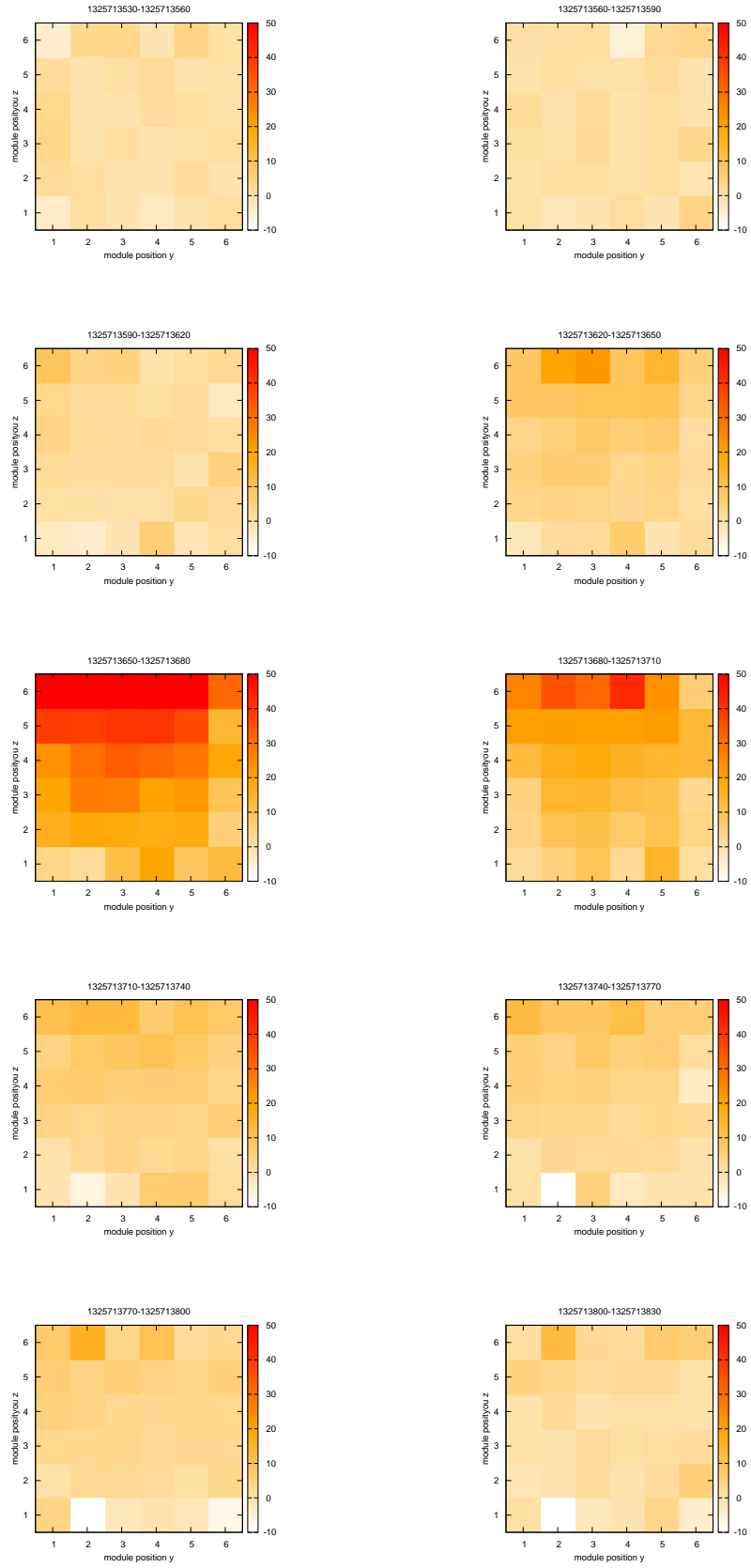


Figure 4.44: Temporal variation of E_{1st} distribution around burst-20120105

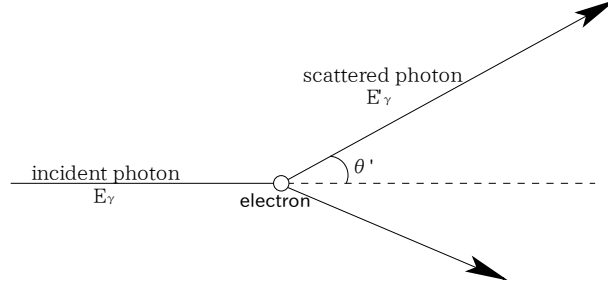


Figure 4.45: Compton scattering

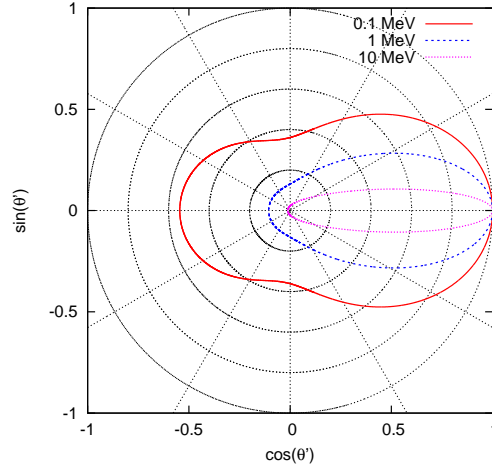


Figure 4.46: The cross-sections of Compton scattering for unpolarized photons

4.6.2 Arrival direction analysis using Compton scattering angle

Compton scattering is one of the interaction between γ -rays and matter. It is the scattering of photons off electrons (Figure 4.45). An incident photon with energy E_γ is scattered by an electron with a scattering angle of θ' . A part of energy is transferred from the photon to the recoil electron.

The differential scattering cross-section is given by Klein-Nishina formula;

$$\frac{d\sigma}{d\Omega} = \frac{r_0^2}{2} \frac{E_\gamma'^2}{E_\gamma^2} \left(\frac{E_\gamma}{E_\gamma'} + \frac{E_\gamma'}{E_\gamma} - 2 \sin^2 \theta' \cos^2 \eta \right). \quad (4.3)$$

Here r_0 is the classical electron radius and η is the angle between the electric field vector and the scattering direction of the photon. For unpolarized photon, equation (4.3) can be integrated for η and the cross-section is

$$\frac{d\sigma}{d\Omega} = \frac{r_0^2}{2} \frac{E_\gamma'^2}{E_\gamma^2} \left(\frac{E_\gamma}{E_\gamma'} + \frac{E_\gamma'}{E_\gamma} - \sin^2 \theta' \right). \quad (4.4)$$

The angular dependence of the cross-sections for 0.1 MeV, 1 MeV and 10 MeV photons are shown in Figure 4.46. Forward scattering becomes dominant for high energy γ -rays.

The energy of the scattered photon can be calculated from energy momentum conservation law as following.

$$E_\gamma' = \frac{E_\gamma}{1 + \frac{E_\gamma}{m_e c^2} (1 - \cos \theta')}, \quad (4.5)$$

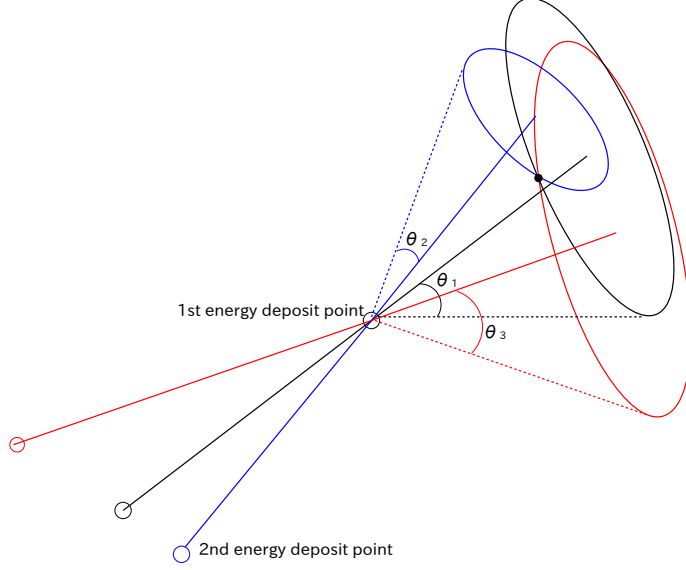


Figure 4.47: Restrict γ -ray incoming direction using multiple Compton cones

where E_γ is the energy of the incident photon and E'_γ is the energy of the scattered photon.

One can calculate θ' from the energy of the incident photon E_γ and the energy of the scattered photon E'_γ using equation (4.5). The arrival direction of γ -rays can be restricted by doing the calculation for the multiple γ -rays and superimposing circular cones (Compton cones) defined by θ' of each scattering if one knows the first and the second interaction points as well as the deposit energy at each point (Figure 4.47).

We made similar analysis to investigate the arrival direction of the burst γ -rays using position information acquired by the PANDA36 detector. We should take care of following problems.

1. Energy of the incident γ -ray was not known
2. A photon could be scattered twice in one module and it can not be discriminated from a single scattering case
3. We do not know which module corresponds to the first Compton scattering interaction point and which module corresponds to the second interaction point, when there are many PANDA modules with energy deposit in them.

At first, we chose the event with $5 \text{ MeV} \leq E_{\text{total}} \leq 12 \text{ MeV}$. This selection removes the effect of ordinary environmental γ -rays and take γ -rays with energies convenient for the analysis. Those γ -rays deposit enough energy on each module to ensure sufficient position resolution.

For the first problem, we assumed E_{total} to be the incident γ -ray energy. To minimize the effect of the energy carried away by γ -rays which escape from the detector, we introduced the following selection criterion.

$$\frac{E_{1\text{st}}}{2} \leq E_{2\text{nd}}, \quad (4.6)$$

where the $E_{1\text{st}}$ and $E_{2\text{nd}}$ is the highest and the second highest energy deposit of all the modules. We show an example of the effect of the γ -ray escape to the $\cos \theta'$ calculation in Figure 4.48. The effect of E_{total} error to $\cos \theta'$ is large near the Compton edge. We can at least cut the right hand side region of the light blue dashed line in Figure 4.48 by selection (4.6).

Selection (4.6) is also a good answer to the second problem. The event with large $E_{1\text{st}}$ relative to $E_{2\text{nd}}$ tend to have two scatterings in one module. We made Monte Carlo simulations to estimate the effect of the selection. γ -rays with energy spectrum estimated in Section 4.5

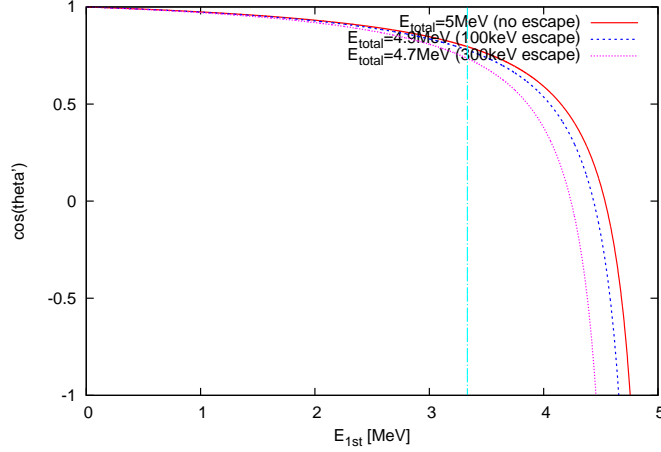


Figure 4.48: An example of the effect of γ -ray escape to the $\cos \theta'$ calculation when incident γ -ray energy is 5 MeV. We assume E_{total} to be the energy of the incident γ -ray and the red solid line shows the cases with no γ -ray escape (correct value), and the blue dotted line and pink line show the case when a 100 keV γ -ray has escaped and when a 300 keV γ -ray has escaped, respectively. The effect of γ -ray escape is large near the Compton edge.

Table 4.4: Fraction of events whose first and second scatterings occur in one module calculated by Monte Carlo method. The errors are only statistical.

	γ -rays by 16 MeV e^- at 1100 m	γ -rays by 16 MeV e^- at 400 m
without selection (4.6)	$39 \pm 0.9\%$	$39 \pm 1.3\%$
with selection (4.6)	$27 \pm 1.8\%$	$28 \pm 2.7\%$

were shot incident on the PANDA36 detector and the events whose first and second scatterings occurred in one module were counted. The results are shown in Table 4.4.

To manage the third problem, we estimated the fraction of the events in which the first interaction deposited the highest energy $E_{1\text{st}}$ and the second interaction deposited the second highest energy $E_{2\text{nd}}$ by a Monte Carlo simulation. We found that the fractions are $47 \pm 3\%$ for γ -rays emitted by 16 MeV electrons at 1100 m and $49 \pm 4\%$ for γ -rays emitted by 16 MeV electrons at 400 m. We also estimated the fraction of the other way around; the first interaction deposited $E_{2\text{nd}}$ and the second interaction deposited $E_{1\text{st}}$. $38 \pm 2\%$ for γ -rays emitted by 16 MeV electrons at 1100 m and $37 \pm 3\%$ for γ -rays emitted by 16 MeV electrons at 400 m. We found that these two cases dominate the burst events and the third highest energy deposit $E_{3\text{rd}}$ or still lower energy deposits need not be taken into account in the Compton scattering direction analysis.

In order to resolve the remaining ambiguity of two cases, we simply assumed that the gamma rays came from the upper hemisphere centered at the detector as is suggested by the analysis of Section 4.6.1.

Table 4.5: The selection criteria of the events for $\cos \theta'$ calculation	
E_{total} selection to cut the noisy region	$5 \text{ MeV} \leq E_{\text{total}} \leq 12 \text{ MeV}$
$E_{1\text{st}}, E_{2\text{nd}}$ ratio selection	$E_{1\text{st}}/2 \leq E_{2\text{nd}}$
distance selection	$ y(E_{1\text{st}}) - y(E_{2\text{nd}}) > 2 \text{ modules}$ or $ z(E_{1\text{st}}) - z(E_{2\text{nd}}) > 2 \text{ modules}$

In addition, we required that the position of E_{1st} was distant enough from the position of E_{2nd} along the stacking direction of the modules (y and z direction in the Figure 4.49). The positions of E_{1st} and E_{2nd} were required to be interleaved with more than two modules in y or z direction. This selection reduces the effect of the periodical structure of the detector which may discretize the result of the scattering angle calculation. All selection criteria of the events for $\cos\theta'$ calculation are listed in Table 4.5.

After above preparations, we calculated arrival direction of γ -ray of the bursts. Scattering angle θ' was calculated for each event which satisfied the selection criteria and corresponding Compton cone was defined as a circle on the unit sphere centered at the detector. Then the circumference of each circle was divided into a thousand pieces of equal lengths and the number of pieces was counted in the predefined grids in the $(\cos\theta, \phi)$ space with a weight of 1/1000 events per entry. The coordinate are illustrated in Figure 4.49. Then we normalized the number of events in each grid by the live time so that it represents the arrival rate of the selected event from the direction.

At first, we made Monte Carlo simulations to know the detector response for γ -rays isotropically incident on the detector. Then the arrival-direction analysis was made for the observed data and we made the following calculation

$$M_i = (M_{i,burst} - M_{i,bg}) / (M_{i,sim}). \quad (4.7)$$

Here i represents the grid number, $M_{i,burst}$, $M_{i,bg}$ are the calculated arrival rate of each grid in the burst period and the background period, respectively. $M_{i,sim}$ is the arrival rate calculated by the Monte Carlo simulation, which is normalized so as to get the average value of all the grids to be 1. Used $M_{i,sim}$ are shown in Figure 4.50–4.52.

We then made Monte Carlo simulations using Geant4 to know the availability of the arrival direction analysis. We simulated the detector response to the γ -ray incoming to the PANDA36 detector from $(\theta, \phi) = (\pi/6, \pi/2), (\pi/3, \pi/2), (\pi/2, \pi/2), (\pi/2, \pi/6), (\pi/2, \pi/3)$. Energy spectrum of bremsstrahlung γ -rays emitted by 16 MeV electrons shot from 1100 m, which are described in Section 4.5, were used. We applied Equation 4.7 to each simulated detector responses and analyzed the arrival direction of γ -rays. The result is shown in Figure 4.53–4.55 and Figure 4.56–4.57.

Same analysis was applied to the observed bursts and calculated arrival rate from each direction for the three bursts are shown in Figure 4.58–4.60. And for each figure, we sliced the map along the ϕ and $\cos\theta$ direction at the maximum bin and plotted ϕ distributions and $\cos\theta$ distributions of the arrival directions (Figure 4.61–4.64). The error bars in those plots only represent statistical errors and systematic errors mainly due to the energy and position resolutions of modules are not considered. We found from the figures that the γ -rays came from the direction close to the zenith in to the detector for all the three bursts.

Temporal variations of arrival directions are shown in Figure 4.67–4.69 and Figure 4.70–4.75. The maximum variation of arrival direction during each burst was estimated from those figures. For ϕ , they were 0.4 ± 0.5 [rad/30sec], 0.3 ± 0.6 [rad/30sec] and 0.2 ± 0.9 [rad/30sec] for burst-20111225, burst-20120102 and burst-20120105 respectively. And for $\cos\theta$, they were 0.2 ± 0.5 [30sec], 0.1 ± 0.5 [30sec] and 0.08 ± 0.5 [30sec]. The errors were estimated from standard deviations of each distribution. We conclude that arrival direction stayed constant during the periods of all three bursts within errors.

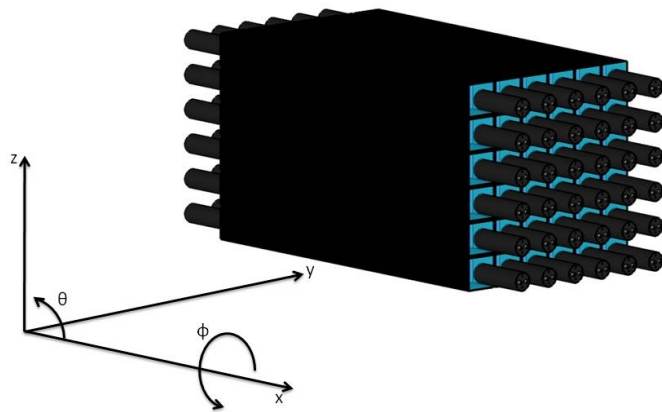


Figure 4.49: The coordinate used for the arrival direction analysis

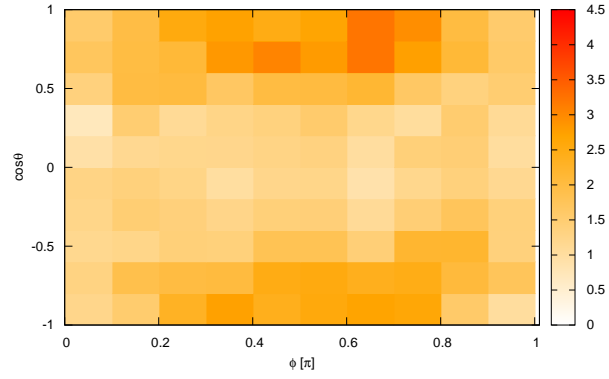


Figure 4.50: Simulated arrival direction distribution by γ -rays isotropically incident on the detectors. The energy spectrum of bremsstrahlung γ -rays of burst-20111225 which is calculated in Section 4.5 was used.

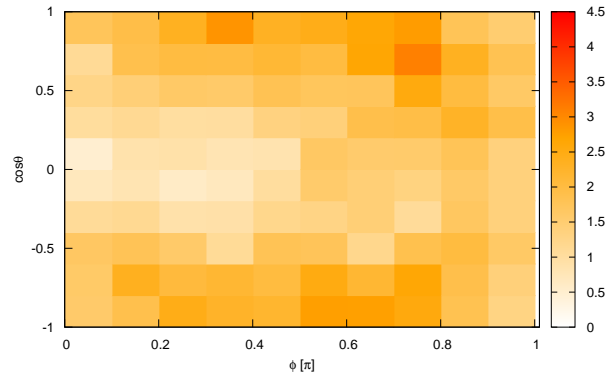


Figure 4.51: Same as Figure 4.50, but used γ -ray spectrum was the spectrum of bremsstrahlung γ -rays of burst-20120102

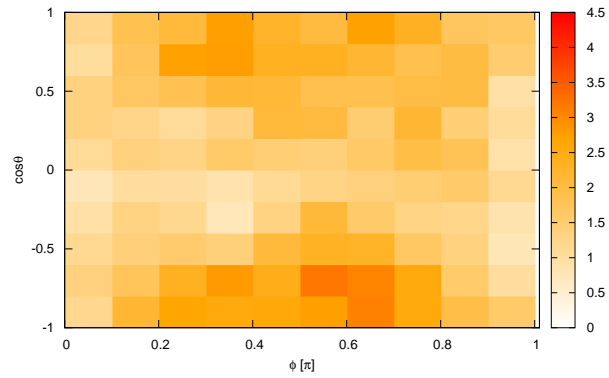


Figure 4.52: Same as Figure 4.50, but used γ -ray spectrum was the spectrum of bremsstrahlung γ -rays of burst-20120105

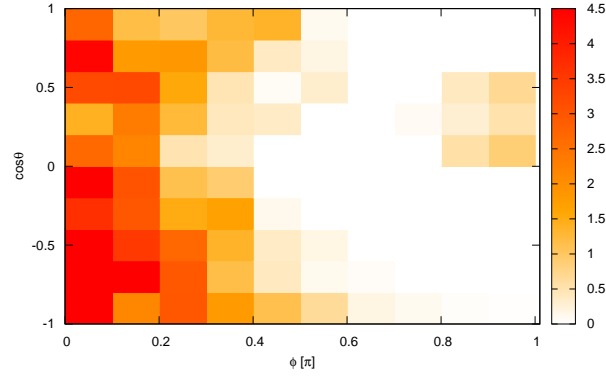


Figure 4.53: The result of arrival direction analysis to the simulated detector response to the γ -rays incoming from $(\theta, \phi) = (\pi/2, \pi/6)$

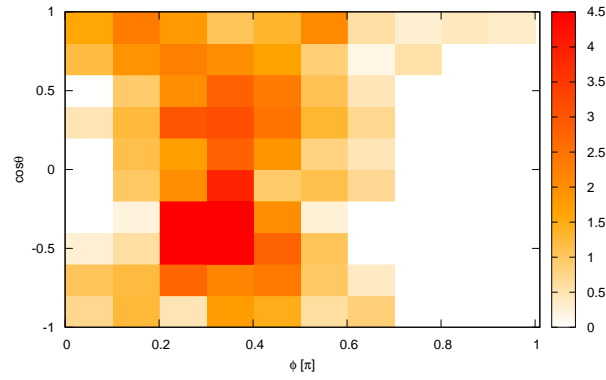


Figure 4.54: Same as Figure 4.53 but for γ -rays incoming from $(\theta, \phi) = (\pi/2, \pi/3)$

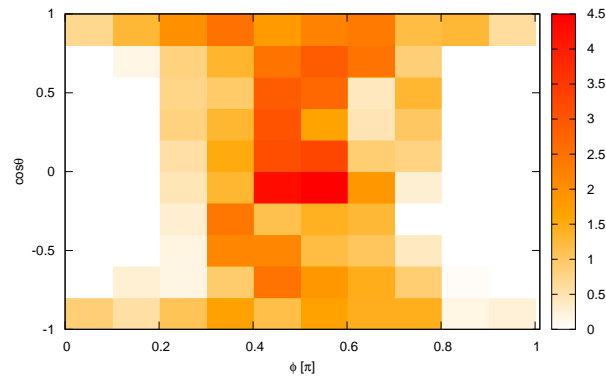


Figure 4.55: Same as Figure 4.53 but for γ -rays incoming from $(\theta, \phi) = (\pi/2, \pi/2)$

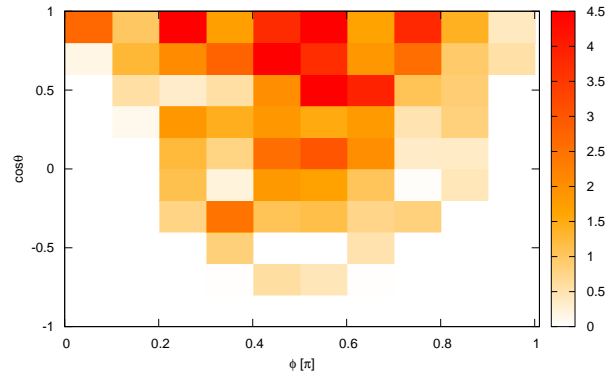


Figure 4.56: Same as Figure 4.53 but for γ -rays incoming from $(\theta, \phi) = (\pi/6, \pi/2)$

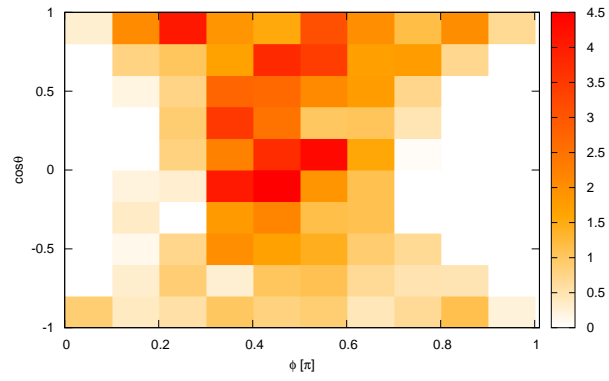


Figure 4.57: Same as Figure 4.53 but for γ -rays incoming from $(\theta, \phi) = (\pi/3, \pi/2)$

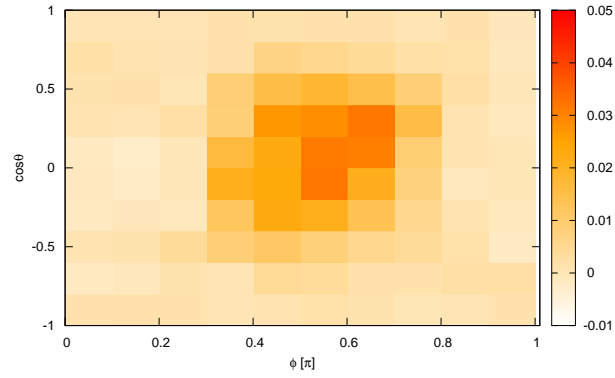


Figure 4.58: burst-20111225: arrival direction distribution of γ -rays. The coordinate is defined in Figure 4.49 and only the upper hemisphere of the detector is shown ($\cos\theta = 0, \phi = 1.57$ is vertically upward of the detector).

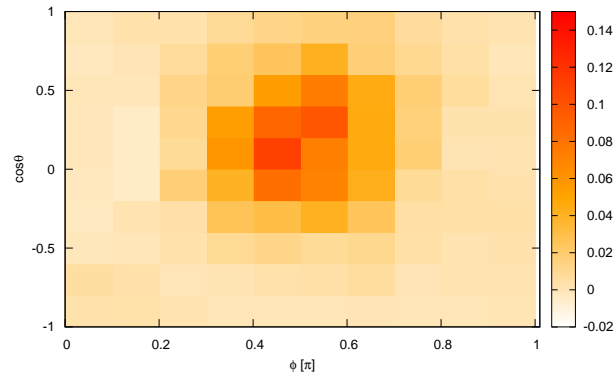


Figure 4.59: burst-20120102: arrival direction distribution of γ -rays

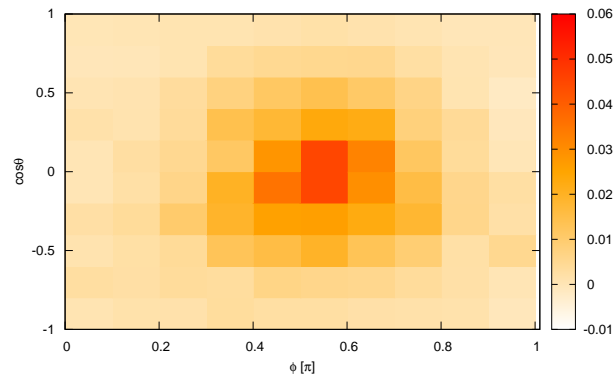


Figure 4.60: burst-20110105: arrival direction distribution of γ -rays

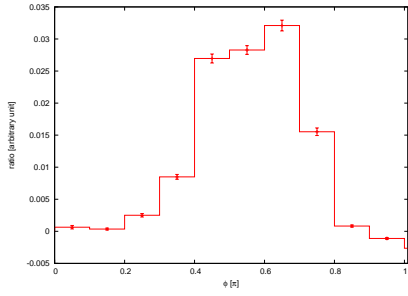


Figure 4.61: burst-20111225: ϕ distribution of arrival direction of incoming γ -rays during the burst. The error bars represent the statistical error.

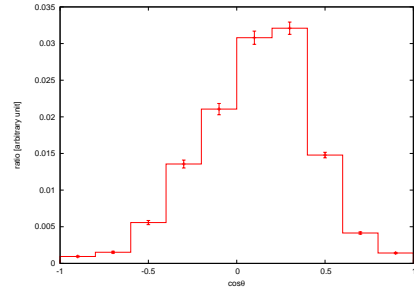


Figure 4.62: burst-20111225: $\cos\theta$ distribution of arrival direction of incoming γ -rays during the burst. The error bars represent the statistical error.

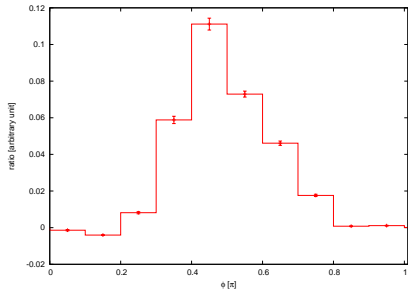


Figure 4.63: burst-20120102: Same as Figure 4.61

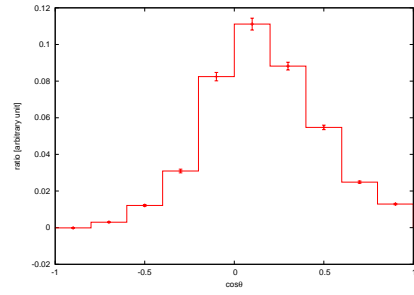


Figure 4.64: burst-20120102: Same as Figure 4.62

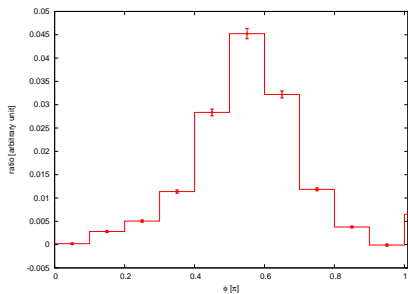


Figure 4.65: burst-20120105: Same as Figure 4.61

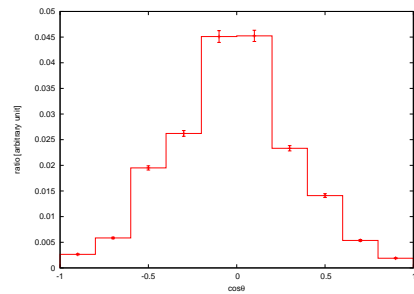


Figure 4.66: burst-20120105: Same as Figure 4.62

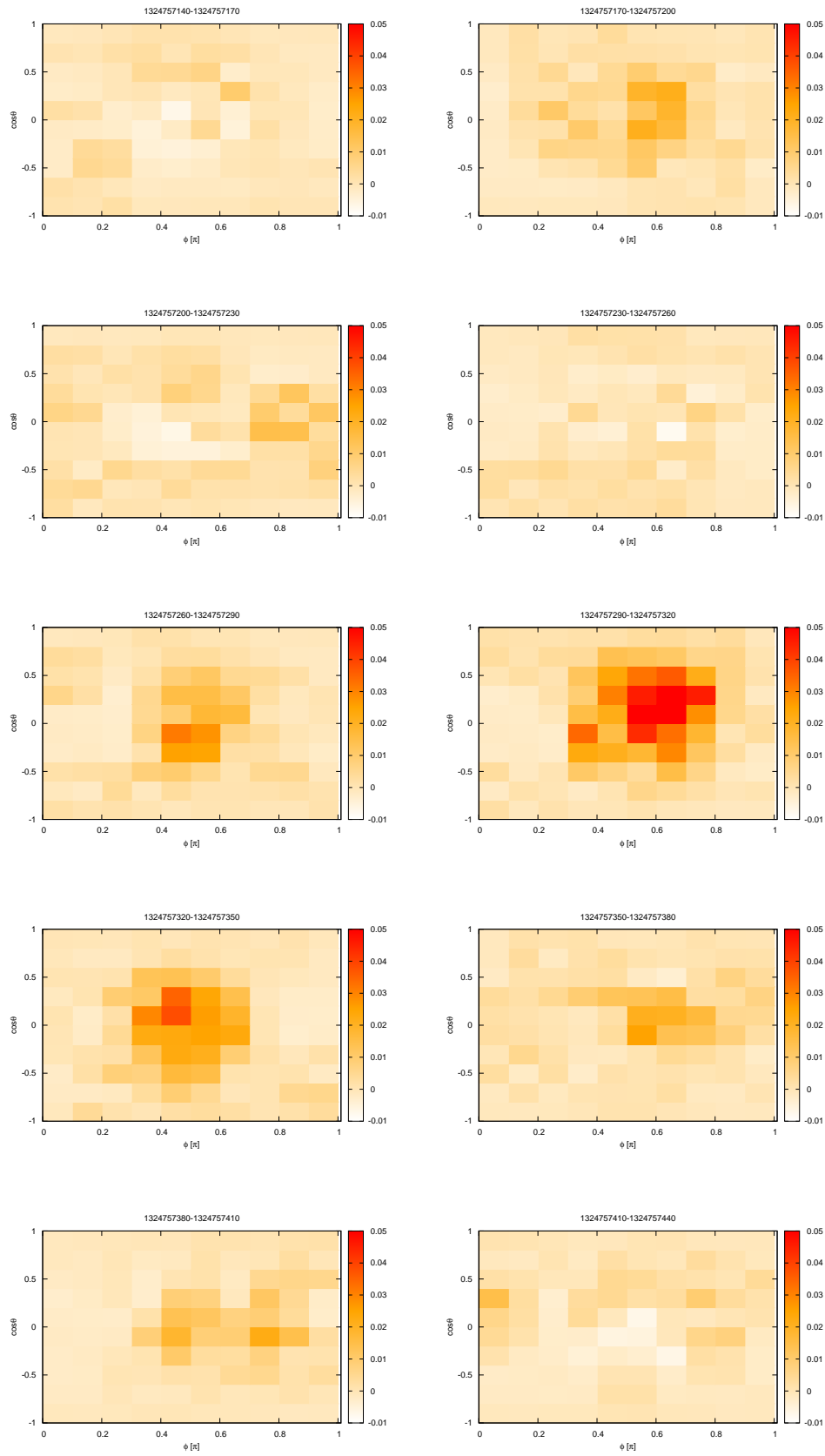


Figure 4.67: Temporal variation of the arrival direction distribution around burst-20111225

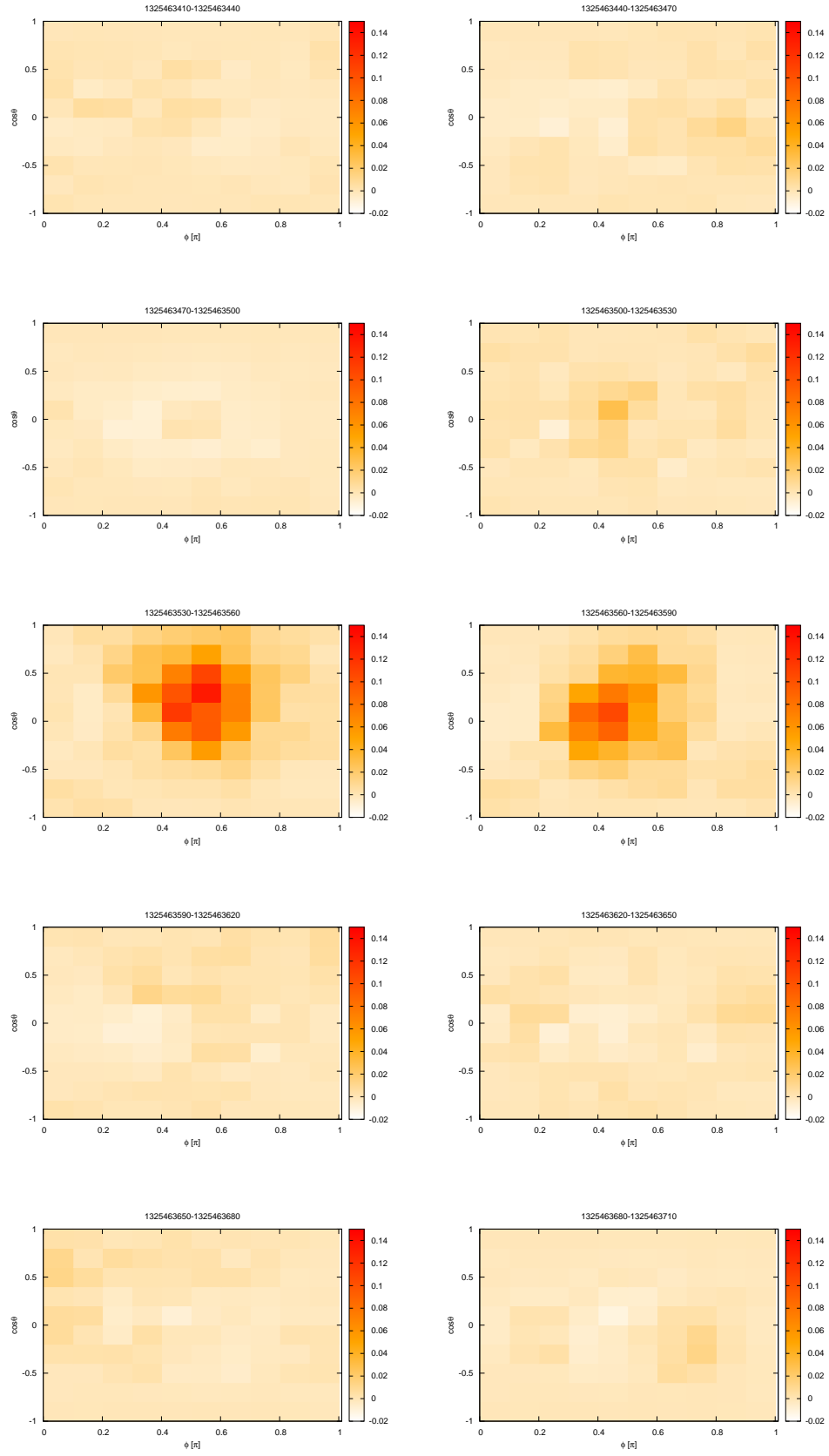


Figure 4.68: Temporal variation of the arrival direction distribution around burst-20120102

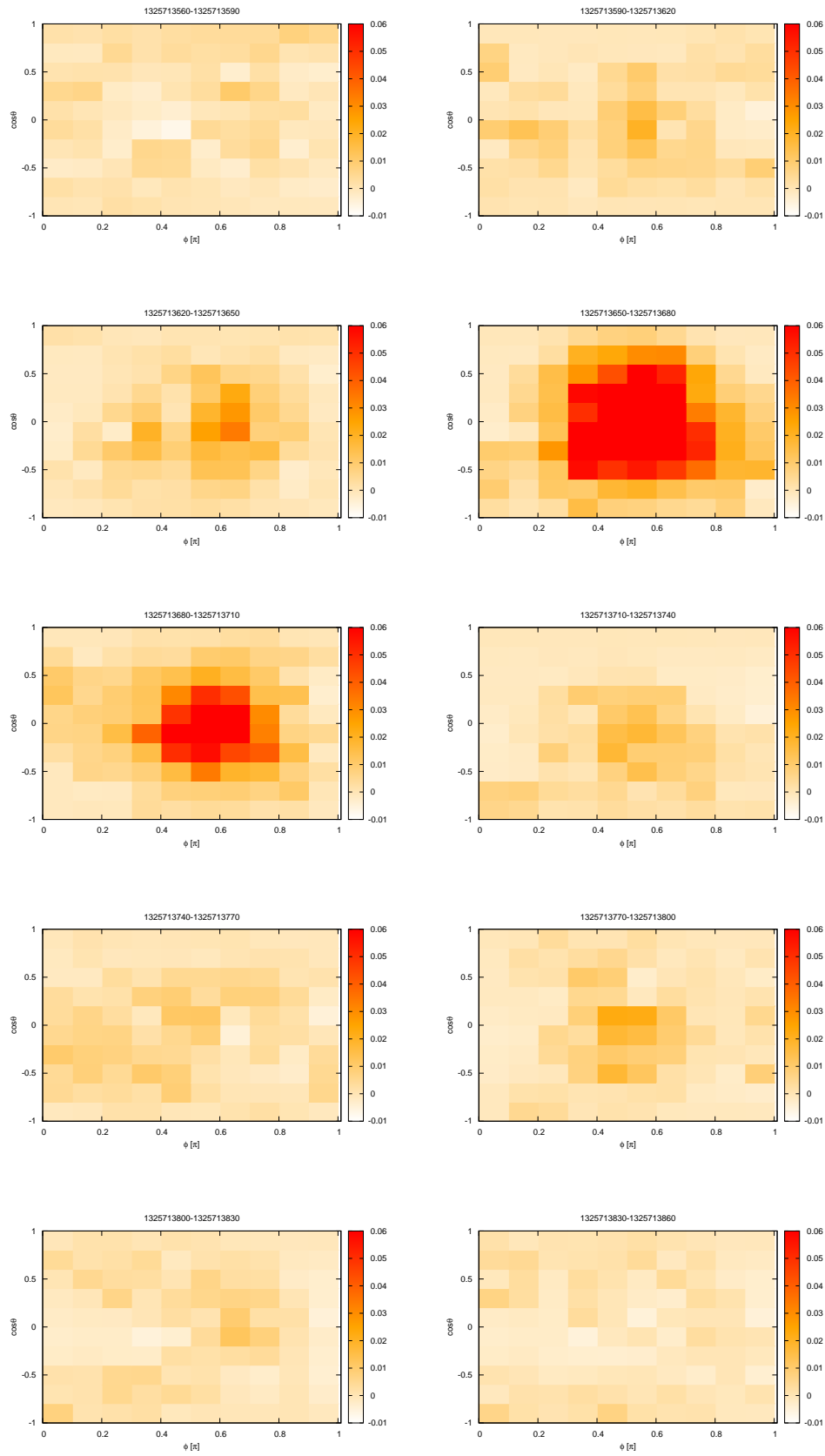


Figure 4.69: Temporal variation of the arrival direction distribution around burst-20120105

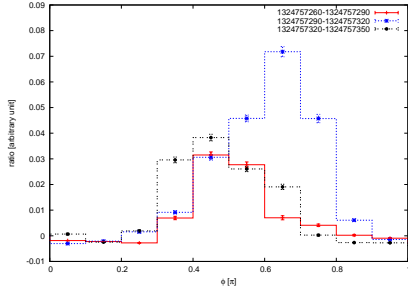


Figure 4.70: Temporal variation of the ϕ distribution around burst-20111225

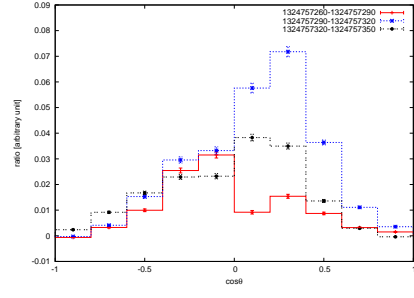


Figure 4.71: Temporal variation of the $\cos \theta$ distribution around burst-20111225

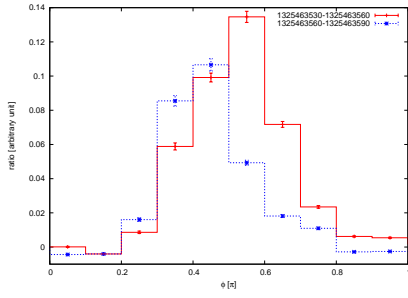


Figure 4.72: Temporal variation of the ϕ distribution around burst-20120102

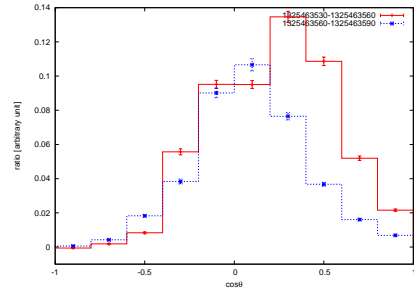


Figure 4.73: Temporal variation of the $\cos \theta$ distribution around burst-20120102

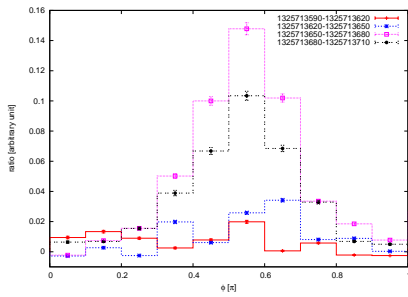


Figure 4.74: Temporal variation of the ϕ distribution around burst-20120105

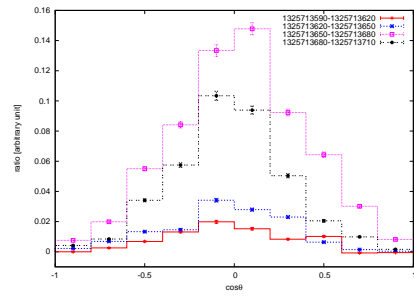


Figure 4.75: Temporal variation of the $\cos \theta$ distribution around burst-20120105

Table 4.6: Selection criteria for neutrons		
	correlated	accidental
prompt event	$1.5 \text{ MeV} \leq E_{\text{total}} \leq 10.0 \text{ MeV}$	
delayed event	$1.5 \text{ MeV} \leq E_{\text{total}} \leq 10.0 \text{ MeV}$	
time window	$8\mu\text{sec} - 150\mu\text{sec}$	$1008\mu\text{sec} - 1150\mu\text{sec}$

4.7 Neutron event-rate increase

As we described in Chapter 3, the PANDA36 detector is originally designed to detect the inverse beta decay event of the anti-electron neutrino by delayed coincidence method. This time, we took advantage of the ability of the detector to get delayed coincidence of two signals to detect the temporal event-rate variation of the neutrons.

Neutrons entering the detector interact with protons in the plastic scintillators. The neutrons transfer up to all of their energy to recoil-protons by an elastic collision. Then, typically after $O(10)\mu\text{sec}$, neutrons which lose their energy are captured by gadolinium (Gd) nuclei in the Gd coated Mylar films wrapped around the scintillators. The Neutron capture on Gd results in a gamma cascade emission with total energy 7.9 MeV for ^{157}Gd and 8.5 MeV for ^{155}Gd .

Since neutrons likely to be detected as sets of events with $O(10)\mu\text{sec}$ intervals, if there were a certain amount of neutrons around the detector, the distribution of intervals between triggered event may contain correlated, non-random component. We compared the observed distribution of intervals between triggered events and simulated intervals assuming that each event has no temporal correlation to each other. The results were shown in Figure 4.76–4.78. There was no significant difference in the observed distributions and simulated random distributions.

Those figures are about all triggered event without event selection and very small number of correlated events could be buried in huge number of random events. To investigate such small events, we selected two kinds of delayed coincidence events, correlated events and accidental events, with selection criteria summarized in Table 4.6. The total energy is required to be $1.5 \text{ MeV} \leq E_{\text{total}} \leq 10.0 \text{ MeV}$ for both the selections but the time window of $8 - 150\mu\text{sec}$ for the correlated events and $1008 - 1150\mu\text{sec}$ for the accidental events. We calculated the number of the neutron events by subtracting the accidental event rate from the correlated event.

The result is shown in Figure 4.79–4.81. We found event-rate increase which is synchronized with the γ -ray burst with maximum rate of $14 \pm 5 \text{ (stat.) /sec}$ in burst-20120105.

The numbers of detected correlated events and accidental events in the burst period of 180 sec (86% livetime) are 3407 and 3232 respectively. The background subtracted E_{total} spectra of the prompt events and the delayed events are shown in Figure 4.82 with the same spectra for 10 MeV neutrons isotropically incident on the detector, which is calculated by a Monte Carlo simulation by Geant4. We normalized the Monte Carlo histograms to the total number of the observed data. The shape of the observed spectra were consistent with the Monte Carlo simulation of the neutrons within the limited statistics.

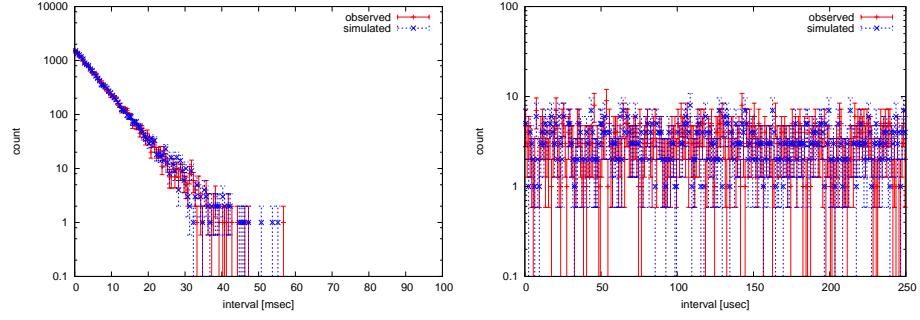


Figure 4.76: Observed distribution of intervals between triggered events and simulated intervals assuming that each event has no temporal correlation to each other. (left) The distribution shown in wide range (0-100 msec). (right) small region is magnified (0-200 μ sec).

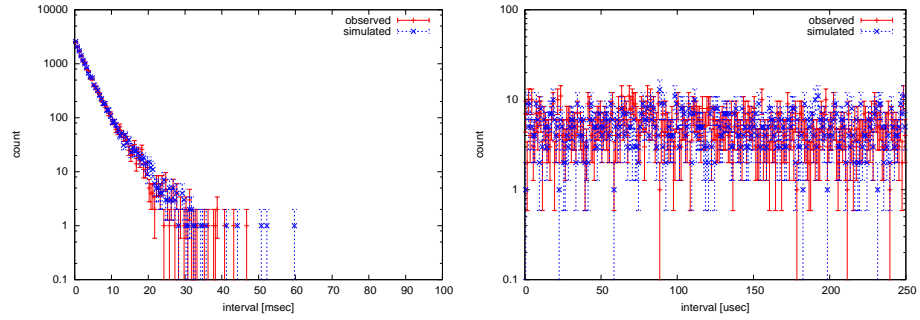


Figure 4.77: burst-20120102: Same as Figure 4.76

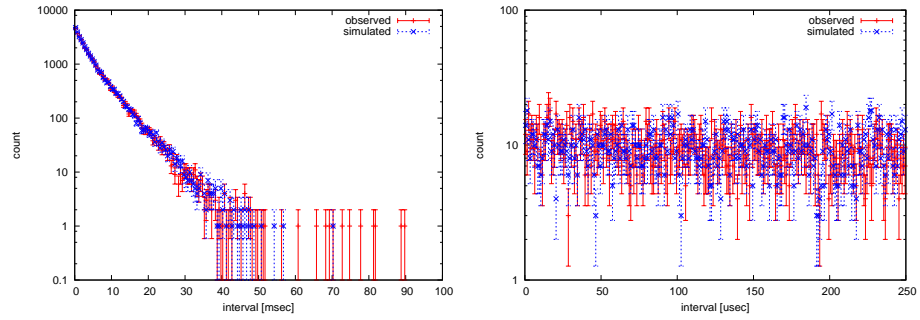


Figure 4.78: burst-20120105: Same as Figure 4.76

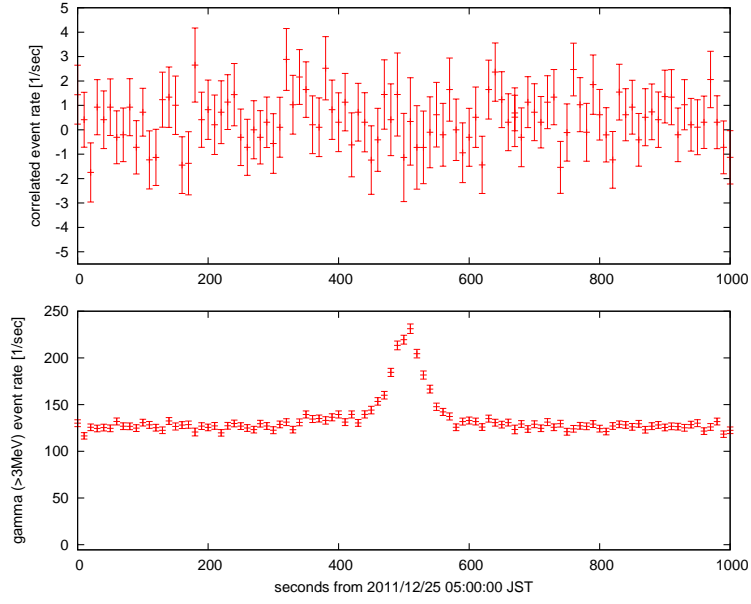


Figure 4.79: Temporal variation of the number of correlated events in the burst-20111225

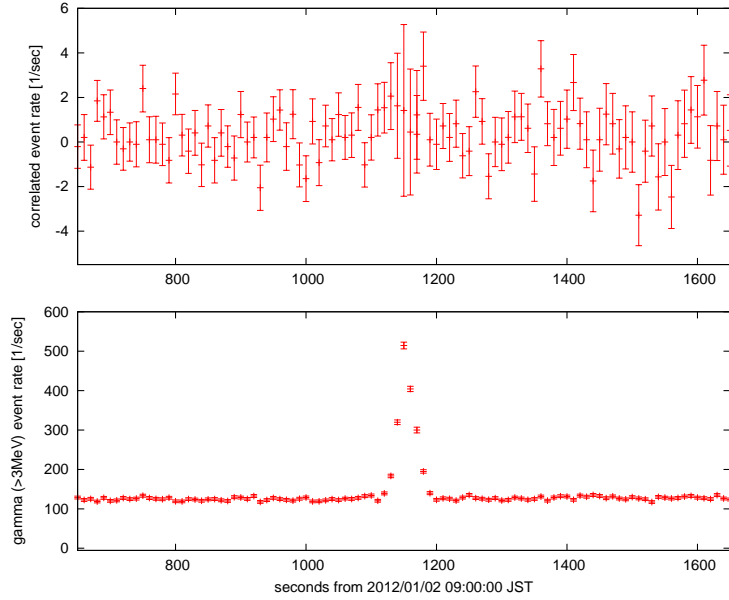


Figure 4.80: Temporal variation of the number of correlated events in the burst-20120102

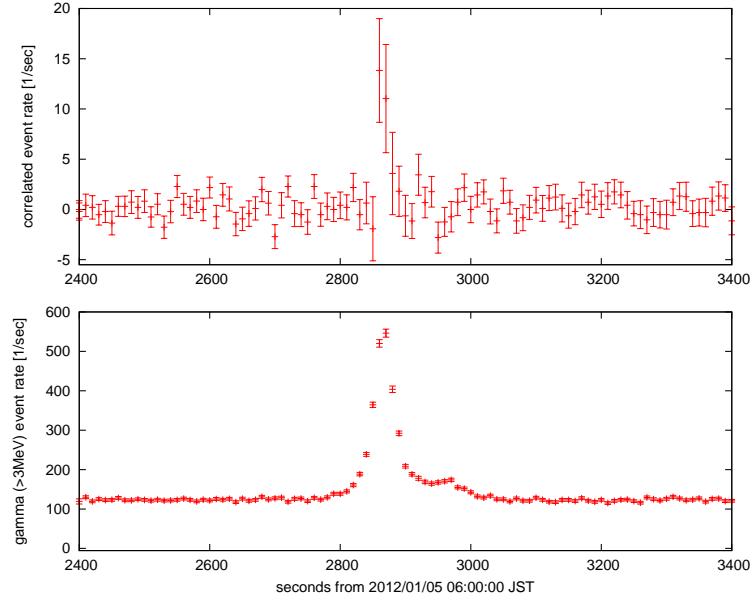


Figure 4.81: Temporal variation of the number of correlated events in the burst-20120105

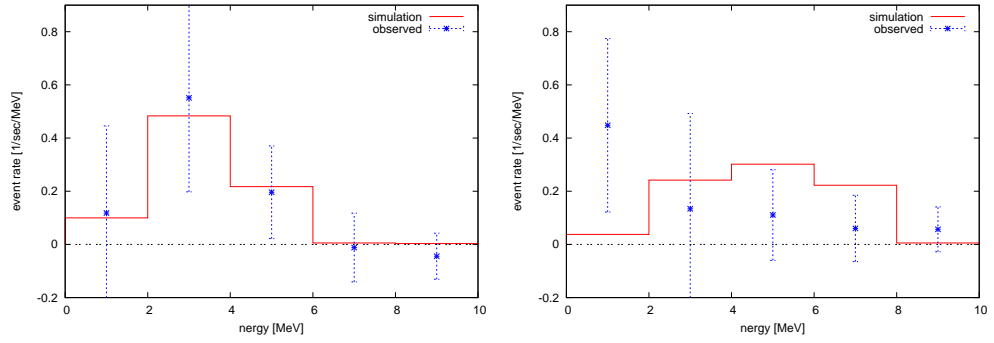


Figure 4.82: The E_{total} spectra of the prompt event (left) and the delayed event (right) of the correlated event in burst-20120105. The error bars represent the statistical error. Solid lines represent the spectra by 10 MeV neutrons isotropically incident on the detector calculated by the Geant4 simulation. The simulation histograms were normalized to the total number of the real data.

Chapter 5

Discussion about the model of γ -ray burst related to the thunder clouds

With the results described in Chapter 4, we investigated the electron flux in the lower parts of the thunderclouds and the electron amplification in the electric field of the thunderclouds.

At first, we calculated the detection efficiencies of the PANDA36 detector for the bremsstrahlung γ -rays of each burst which is calculated in Section 4.5 by Monte Carlo simulations via Geant4 toolkit. The efficiencies were calculated by dividing the rate of triggered events with $E_{\text{total}} \geq 3 \text{ MeV}$ by the flux of γ -rays with energy higher than 3 MeV just above the detector. As a result, the efficiencies were $(1.03 \pm 0.05) \times 10^{-1} [\text{m}^2]$ for simulated bremsstrahlung γ -rays of burst-20111225, $(0.99 \pm 0.03) \times 10^{-1} [\text{m}^2]$ for burst-20120102 and $(0.98 \pm 0.04) \times 10^{-1} [\text{m}^2]$ for burst-20120105. The errors are the statistical errors obtained from individual Monte Carlo runs.

Using the γ -ray detection efficiencies, we estimated the incident γ -ray flux on the detector at the peak of the three bursts. Then using the ratio of the number of the photons which reached the ground to the projected electrons in the sky (Table 5.1), we calculated the flux of the electrons required to get the maximum γ -ray flux of each burst. We used the energy spectra of the electrons and the heights of the shot which describes the observed result the best estimated in Section 4.5. The results are shown in Table 5.2. We assumed that the area of electron acceleration regions in the thunder clouds were large enough.

The integral intensity of cosmic ray electrons above 1 MeV at sea level is calculated from spectrum presented in [63] and it is about $40 \text{ /sec/m}^2/\text{sr}$. The radio isotope density is typically $O(10) \text{ Bq/m}^3$ in the building and it is supposed to be much lower outdoor in the sky. Therefore, most high-energy electrons in the atmosphere are secondary cosmic rays. So we only consider the flux of secondary cosmic-ray electrons.

For simplicity, we assumed that the solid angles of the cosmic ray electrons were simply assumed to be $2\pi \text{ sr}$. Then, the number of seed cosmic-ray electrons were estimated as $2.5 \times 10^2 \text{ /sec/m}^2$. Using the seed electron flux and the estimated e^- flux in Table 5.2, electron amplification factor in the electric field of thunderclouds were calculated as 7.5×10^2 , 8.0×10^2 and 3.5×10^2 for burst-20111225, burst-20120102 and burst-20120105 respectively.

Table 5.1: Ratio of bremsstrahlung photons which reached the ground with the energy higher than 3 MeV calculated by the Monte Carlo simulation. The errors are statistical.

burst	height of projection [m]	(number of γ -rays at 0 m) / (number of source e^-)
burst-20111225	900	$(7.1 \pm 0.3) \times 10^{-3}$
burst-20120102	500	$(2.1 \pm 0.1) \times 10^{-2}$
burst-20120105	100	$(5.3 \pm 0.2) \times 10^{-2}$

Table 5.2: The estimated electron flux of the three bursts. The errors are statistical.

burst	γ -ray flux [$1/(\text{sec} \cdot \text{m}^2)$]	required e^- flux [$1/(\text{sec} \cdot \text{m}^2)$]
burst-20111225	$(1.3 \pm 0.1) \times 10^3$	$(1.9 \pm 0.1) \times 10^5$
burst-20120102	$(4.2 \pm 0.2) \times 10^3$	$(2.0 \pm 0.1) \times 10^5$
burst-20120105	$(4.7 \pm 0.2) \times 10^3$	$(8.8 \pm 0.5) \times 10^4$

These amplification factors were calculated under relativistic runaway electron avalanche (RREA) hypothesis and have large systematic errors for individual bursts mainly due to the following reasons.

First, the calculation of the intensity of seed electrons has the error of factor of two or more.

Second, we used the electron projection height obtained from the best fit spectrum of each burst to calculate the amplification factors. As we can see in Figure 4.23–4.25 in Section 4.5, however, there are ambiguities of about 1000 m in the determination of the projection heights.

To estimate the effect of the height ambiguity, we did additional analysis with varying the height of the electron projection. As we described in Section 4.5, the spectra of the bursts can be explained by accelerated electrons in small energy range at its projection height. Therefore, we supposed in the analysis that the electron emissions in the sky were monochromatic. Since we got the best fit in the monochromatic electron analysis in Section 4.5 with 16 MeV electrons for all of the three bursts, we used 16 MeV electrons for calculating the amplification factor.

We calculated the amplification factor using the ratio of the number of the photons which reached the ground to the number of the projected electrons from each height. The result was shown in Figure 5.1–5.3. About 1000 m ambiguity of height leads to one order of magnitude difference in the amplification factors.

In the past, the behavior of electrons in thunder clouds were calculated by Torii *et al.* [40, 64] by Monte Carlo simulation. In their analysis, they calculated the electron flux in the strong electric fields, which accompanies tripole winter thunder clouds in comparison with the case with no electric field. They introduced the simulation results that assuming the secondary cosmic ray electrons as the seed particles, the maximum flux of the electron is about a hundred times larger than the no electric field case.

The amplification factors calculated by our result are several times larger than their estimation. The difference could be due to the height, the position and the ambiguity of the electric field model of the thunder clouds.

As we described in Section 4.6.2, the arrival direction of γ -rays during the bursts entered into the detector were close to the zenith and stayed constant during the bursts within our detector resolution.

From our observation, we can make an assumption that the seed electron are provided to the thunder clouds continuously by cosmic rays, which describes the long duration of the burst by RREA electron multiplication process despite of the too low event rate. The duration of the bursts may depend on the movement or the development stage of the clouds. For example, the duration of the burst-20120105, ~ 180 sec can be explained by the thunder cloud which have typical velocity of 50 km/h and diameter of 2.5 km, which is smaller than typical echo size of thunder clouds (which is 4–6 km [65]). The fact that there were many cases that the thunder cloud above the detector did not create the burst (Section 4.2) indicates that the area of the acceleration region is small or the lifetime of the acceleration region is short in comparison with the lifetime of the thunder clouds.

In addition, due to the low temperature, the altitude of the thunder clouds at midwinter is low [65], which explains the result that the observed energy spectra implies the low altitude electron source and the fact that we could not observe any burst in summer.

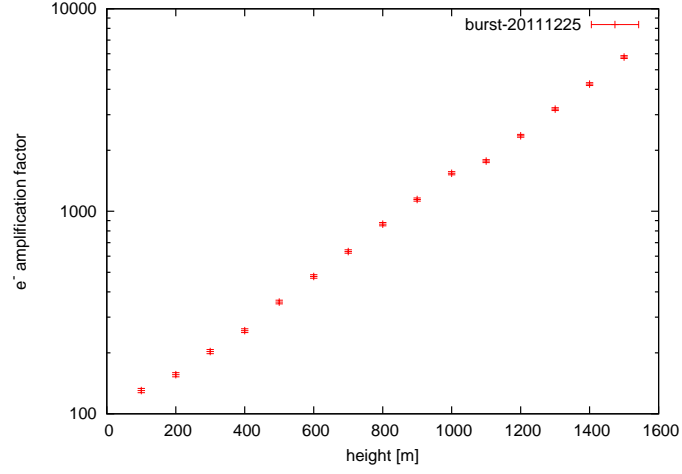


Figure 5.1: Estimated electron amplification factors for each electron projection heights. Assuming that the energy of the projected electrons was monochromatic (16 MeV). Error bars are only statistical.

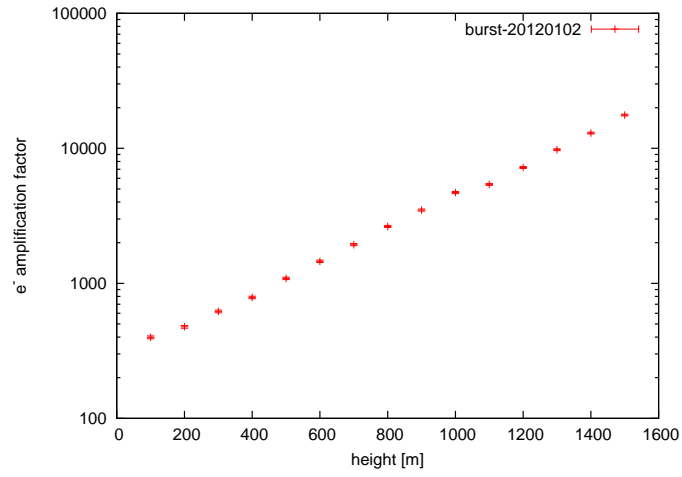


Figure 5.2: Same as Figure 5.1 but for burst-20120102

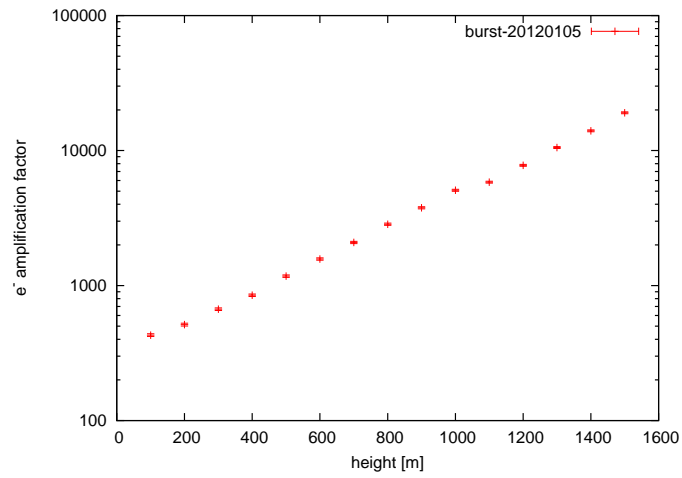


Figure 5.3: Same as Figure 5.1 but for burst-20120105

Chapter 6

Conclusion

We observed three γ -ray bursts with the prototype of anti-neutrino detector PANDA at Ohi Power Station which stands on the southeastern coastal area of the Japan Sea. Table. 6.1 summarizes the features of the observed bursts. The maximum rate of the events with $E_{\text{total}} \geq 3$ MeV was $(5.5 \pm 0.1 \text{ (stat.)}) \times 10^2/\text{sec}$ of burst-20120105 (Section 4.1).

We found that for all the bursts periods, there were thunder clouds near the detector (Section 4.2).

In addition, we investigated the arrival direction of γ -rays during the burst period taking advantage of the position information of energy deposits. From $E_{1\text{st}}$ distributions which are shown in Figure 4.39–4.41 (Section 4.6.1) and the results of Compton scattering-angle calculation which are shown in Figure 4.58–4.60 (Section 4.6.2), we found that γ -rays of the bursts entered into the detector from the sky and from the direction close to the zenith. The arrival direction stayed constant during the burst within our detector resolution.

These results indicated that the bursts originated from thunder clouds. We made simple Monte Carlo simulations to calculate bremsstrahlung γ -ray spectra from electrons projected vertically downward from the sky and investigated the detector response.

The result of the simulation showed that the simulated spectra of bremsstrahlung γ -rays by electrons with energy spectra shown in Figure 4.32–4.34 from 900 m (burst-20111225), 500 m (burst-20120102) and 100 m (burst-20120105) well describe the observed E_{total} spectra of the bursts (Section 4.5).

The result of the electron spectra estimation indicates that the energy of the accelerated electrons just below the thunder cloud likely to have nearly monochromatic energy.

The arrival direction of the γ -rays and the estimated energy of the projected electrons of over 10 MeV can be described by relativistic runaway electron avalanche (RREA). Namely, the secondary cosmic-ray electrons, which act as seed, were accelerated and amplified in electric field of thunderclouds.

We estimated the electron amplification factor in the electric field in the thunder clouds from our observation results. The estimated amplification factors are 7.5×10^2 , 8.0×10^2 and 3.5×10^2 for burst-20111225, burst-20120102 and burst-20120105 respectively with an order of magnitude ambiguity arising from the uncertainty of the number of the seed electrons and the height of the electron projection.

Additionally, time correlated events, the feature of which is consistent with the neutron absorption in the Gadolinium, were detected at the maximum rate of $\sim 14 \pm 5 \text{ (stat.)}/\text{sec}$. There is probability those event rate increase could include neutrons emitted by the photonuclear reactions on the nitrogen atoms in the air. In our observation, the delayed coincidence events were only found in burst-20120105, in which the electrons were expected to be accelerated at very low altitude (100 m). It could be due to the large flux of bremsstrahlung γ -ray with energy greater than the photonuclear reaction threshold for nitrogen. More observations are needed to strengthen the detection of neutron events and to understand its origin.

Table 6.1: Features of the three γ -ray bursts

burst name	burst-20111225	burst-20120102	burst-20120105
date and time of the burst	2011 12/25 05:07 JST	2012 01/02 09:19 JST	2012 01/05 06:46 JST
duration [sec]	90	60	180
peak event rate ($E_{\text{tot}} > 3\text{MeV}$) [1/sec]	$(2.3 \pm 0.1(\text{stat.})) \times 10^2$	$(5.1 \pm 0.1(\text{stat.})) \times 10^2$	$(5.5 \pm 0.1(\text{stat.})) \times 10^2$
average E_{tot} [MeV]	$4.7 \pm 0.2(\text{stat.})$	$5.0 \pm 0.1(\text{stat.})$	$4.2 \pm 0.1(\text{stat.})$
estimated average energy of the source electrons [MeV]	$18.0 \pm 0.7(\text{stat.})$	$18.1 \pm 0.5(\text{stat.})$	$17.9 \pm 0.4(\text{stat.})$
estimated height of the source electrons [m]	900 m	500 m	100 m
estimated amplification factor of RREA	7.5×10^2	8.0×10^2	3.5×10^2
correlated event detection	not-detected	not-detected	detected

Chapter 7

Acknowledgments

I would like to show my greatest appreciation to Professor M. Minowa. His comments and suggestions were innumerable valuable throughout the course of my study. Especially, I was greatly helped by his guidance after the 2011 off the Pacific coast of Tohoku Earthquake which sent almost all of Japan's nuclear reactors offline. Without his guidance and persistent help, this thesis would not have been possible.

I would like to thank Y. Inoue whose comments with broad knowledge and insight made much contribution to my work.

I appreciate the feedbacks and advices offered by Dr. C. Ito, Dr. S. Oguri, R. Nakata, Y. Kato and N. Tomita.

I also received generous support from all members of Minowa group.

Thanks are also due to Division of Environment, Health and Safety of the University of Tokyo, especially to Professor T. Imoto. They provided us with the logs of air dose rate monitors of the University of Tokyo.

I thank A. Shimokobe who gave me technical advice on managing meteorological data which was unfamiliar to me.

I thank Kansai Electric Power Co.,Inc and Chubu Electric Power Co.,Inc for their cooperation for our experiment on site of Ohi Power Station and Hamaoka Nuclear Power Plant.

This research was partially supported by the Japanese Ministry of Education, Science, Sports and Culture, Grant-in-Aid for COE Research, Grant-in-Aid for Scientific Research (B), and Grant-in-Aid for JSPS Fellows and also by the Mitsubishi Foundation.

References

- [1] C. T. R. Wilson. The electric field of a thundercloud and some of its effects. Proc. Phys. Soc. London, Vol. 37, No. 1, pp. 32D–37D, January 1924.
- [2] G. E. Shaw. Background cosmic count increase associated with thunderstorms. J. Geophys. Res., Vol. 72, No. 18, pp. 4623–4626, September 1967.
- [3] M. Brunetti *et al.* Gamma-ray bursts of atmospheric origin in the MeV energy range. Geophys. Res. Lett., Vol. 27, No. 11, pp. 1599–1602, June 2000.
- [4] M. Aglietta *et al.* The EAS-TOP array at : Stability and resolutions. Nucl. Instruments Methods Phys. Res. Sect. A Accel. Spectrometers, Detect. Assoc. Equip., Vol. 277, No. 1, pp. 23–28, April 1989.
- [5] S. Vernetto, the EAS-TOP Collaboration. The EAS counting rate during thunderstorms. Int. Cosm. Ray Conf., pp. 4165–4168, 2001.
- [6] T. Takami *et al.* Particle acceleration in thunderstorms. In Proc. ICRC 2001, pp. 4027–4030, 2001.
- [7] Y. Muraki *et al.* Effects of atmospheric electric fields on cosmic rays. Phys. Rev. D, Vol. 69, No. 12, p. 123010, June 2004.
- [8] H. Tsuchiya *et al.* Observation of an Energetic Radiation Burst from Mountain-Top Thunderclouds. Phys. Rev. Lett., Vol. 102, No. 25, p. 255003, June 2009.
- [9] T. Torii *et al.* Gradual increase of energetic radiation associated with thunderstorm activity at the top of Mt. Fuji. Geophys. Res. Lett., Vol. 36, No. 13, p. L13804, July 2009.
- [10] A. Chubenko *et al.* Intensive X-ray emission bursts during thunderstorms. Phys. Lett. A, Vol. 275, No. 1-2, pp. 90–100, October 2000.
- [11] a.V. Gurevich *et al.* An intracloud discharge caused by extensive atmospheric shower. Phys. Lett. A, Vol. 373, No. 39, pp. 3550–3553, September 2009.
- [12] D. M. Suszcynsky, R. Roussel-Dupre, G. Shaw. Ground-based search for X rays generated by thunderstorms and lightning. J. Geophys. Res., Vol. 101, No. D18, p. 23505, October 1996.
- [13] C. B. Moore *et al.* Energetic radiation associated with lightning stepped-leaders. Geophys. Res. Lett., Vol. 28, No. 11, pp. 2141–2144, June 2001.
- [14] V. Alexeenko *et al.* Transient variations of secondary cosmic rays due to atmospheric electric field and evidence for pre-lightning particle acceleration. Phys. Lett. A, Vol. 301, No. 3-4, pp. 299–306, August 2002.
- [15] A. Chilingarian *et al.* Ground-based observations of thunderstorm-correlated fluxes of high-energy electrons, gamma rays, and neutrons. Phys. Rev. D, Vol. 82, No. 4, p. 043009, August 2010.

- [16] A. Chilingarian, G. Hovsepyan, A. Hovhannisyan. Particle bursts from thunderclouds: Natural particle accelerators above our heads. Phys. Rev. D, Vol. 83, No. 6, p. 062001, March 2011.
- [17] A. Chilingarian, B. Mailyan, L. Vanyan. Recovering of the energy spectra of electrons and gamma rays coming from the thunderclouds. Atmos. Res., Vol. 114-115, pp. 1–16, October 2012.
- [18] H. Tsuchiya *et al.* Observation of thundercloud-related gamma rays and neutrons in Tibet. Phys. Rev. D, Vol. 85, No. 9, p. 092006, May 2012.
- [19] K. Yamazaki *et al.* Vertical Profile of the Environmental Gamma-ray in Kashiwazaki Kariwa Area –Detection of Bremsstrahlung X-ray Generated by Winter Thunderstorms–. Annual report of Niigata Prefectural Institute of Public Health and Environment Science, Vol. 17, pp. 94–98, 2002.
- [20] T. Torii, M. Takeishi, T. Hosono. Observation of gamma-ray dose increase associated with winter thunderstorm and lightning activity. J. Geophys. Res., Vol. 107, No. D17, p. 4324, 2002.
- [21] T. Enoto *et al.* Detection of gamma-rays from winter thunderclouds along the coast of Japan Sea. In ICRC 2007 Proc. - Pre-Conference Ed., Vol. 1, pp. 1–4, 2007.
- [22] H. Tsuchiya *et al.* Detection of High-Energy Gamma Rays from Winter Thunderclouds. Phys. Rev. Lett., Vol. 99, No. 16, p. 165002, October 2007.
- [23] H. Tsuchiya *et al.* Long-duration γ ray emissions from 2007 and 2008 winter thunderstorms. J. Geophys. Res., Vol. 116, No. D9, p. D09113, May 2011.
- [24] H. Tsuchiya *et al.* Hardening and Termination of Long-Duration γ Rays Detected Prior to Lightning. Phys. Rev. Lett., Vol. 111, No. 1, p. 015001, July 2013.
- [25] T. Torii *et al.* Migrating source of energetic radiation generated by thunderstorm activity. Geophys. Res. Lett., Vol. 38, No. 24, pp. n/a–n/a, December 2011.
- [26] G. Parks *et al.* X-ray enhancements detected during thunderstorm and lightning activities. Geophys. Res. Lett., Vol. 8, No. 11, pp. 1176–1179, 1981.
- [27] M. McCarthy, G. Parks. Further observations of X-rays inside thunderstorms. Geophys. Res. Lett., Vol. 12, No. 6, pp. 393–396, 1985.
- [28] K. Eack, W. Beasley, W. Rust. Initial results from simultaneous observation of X rays and electric fields in a thunderstorm. J. Geophys. ..., Vol. 101, pp. 637–640, 1996.
- [29] K. Eack, D. Suszcynsky. Gamma-ray emissions observed in a thunderstorm anvil. Geophys. ..., Vol. 27, No. 2, pp. 185–188, 2000.
- [30] G. J. Fishman *et al.* Discovery of intense gamma-ray flashes of atmospheric origin. Science, Vol. 264, No. 5163, pp. 1313–6, May 1994.
- [31] A. Gurevich, G. Milikh, R. Roussel-Dupre. Runaway electron mechanism of air breakdown and preconditioning during a thunderstorm. Phys. Lett. A, Vol. 165, No. 5-6, pp. 463–468, June 1992.
- [32] D. M. Smith *et al.* Terrestrial gamma-ray flashes observed up to 20 MeV. Science, Vol. 307, No. 5712, pp. 1085–8, February 2005.

- [33] B. W. Grefenstette *et al.* First RHESSI terrestrial gamma ray flash catalog. J. Geophys. Res., Vol. 114, No. A2, p. A02314, February 2009.
- [34] M. Marisaldi *et al.* Gamma-Ray Localization of Terrestrial Gamma-Ray Flashes. Phys. Rev. Lett., Vol. 105, No. 12, p. 128501, September 2010.
- [35] M. Marisaldi *et al.* Detection of terrestrial gamma ray flashes up to 40 MeV by the AGILE satellite. J. Geophys. Res., Vol. 115, p. A00E13, March 2010.
- [36] M. S. Briggs *et al.* First results on terrestrial gamma ray flashes from the Fermi Gamma-ray Burst Monitor. J. Geophys. Res., Vol. 115, No. A7, p. A07323, July 2010.
- [37] V. Connaughton *et al.* Associations between Fermi Gamma-ray Burst Monitor terrestrial gamma ray flashes and sferics from the World Wide Lightning Location Network. J. Geophys. Res., Vol. 115, No. A12, p. A12307, December 2010.
- [38] A. V. Gurevich, K. P. Zybin. Runaway Breakdown and the Mysteries of Lightning. Phys. Today, Vol. 58, No. 5, p. 37, 2005.
- [39] J. Beringer *et al.* Review of Particle Physics and 2013 partial update for the 2014 edition. Phys. Rev. D, Vol. 86, No. 1, p. 010001, July 2013.
- [40] T. Torii *et al.* Downward emission of runaway electrons and bremsstrahlung photons in thunderstorm electric fields. Geophys. Res. Lett., Vol. 31, No. 5, pp. n/a–n/a, March 2004.
- [41] L. P. Babich *et al.* Source of prolonged bursts of high-energy gamma rays detected in thunderstorm atmosphere in Japan at the coastal area of the Sea of Japan and on high mountaintop. J. Geophys. Res., Vol. 115, No. A9, p. A09317, September 2010.
- [42] L. M. Libby, H. R. Lukens. Production of radiocarbon in tree rings by lightning bolts. J. Geophys. Res., Vol. 78, No. 26, pp. 5902–5903, October 1973.
- [43] R. L. Fleischer, J. A. Plumer, K. Crouch. Are neutrons generated by lightning? J. Geophys. Res., Vol. 79, No. 33, pp. 5013–5017, November 1974.
- [44] G. N. Shah *et al.* Neutron generation in lightning bolts. Nature, Vol. 313, No. 6005, pp. 773–775, February 1985.
- [45] L. P. Babich, R. A. Roussel-Dupré. Origin of neutron flux increases observed in correlation with lightning. J. Geophys. Res., Vol. 112, No. D13, p. D13303, July 2007.
- [46] L. P. Babich *et al.* Localization of the source of terrestrial neutron bursts detected in thunderstorm atmosphere. J. Geophys. Res., Vol. 115, p. A00E28, May 2010.
- [47] A. Shyam, T. C. Kaushik. Observation of neutron bursts associated with atmospheric lightning discharge. J. Geophys. Res., Vol. 104, No. A4, p. 6867, 1999.
- [48] I. M. Martin, M. A. Alves. Observation of a possible neutron burst associated with a lightning discharge? J. Geophys. Res., Vol. 115, p. A00E11, February 2010.
- [49] A. V. Gurevich *et al.* Strong Flux of Low-Energy Neutrons Produced by Thunderstorms. Phys. Rev. Lett., Vol. 108, No. 12, p. 125001, March 2012.
- [50] S. A. Starodubtsev *et al.* First experimental observations of neutron bursts under thunderstorm clouds near sea level. JETP Lett., Vol. 96, No. 3, pp. 188–191, October 2012.
- [51] Y. Kuroda *et al.* A mobile antineutrino detector with plastic scintillators. Nucl. Instruments Methods Phys. Res. Sect. A Accel. Spectrometers, Detect. Assoc. Equip., Vol. 690, pp. 41–47, October 2012.

- [52] S. Oguri. Result of PANDA36 measurement (to be published).
- [53] A. Chilingarian *et al.* Aragats space-environmental centre: status and SEP forecasting possibilities. J. Phys. G Nucl. Part. Phys., Vol. 29, No. 5, pp. 939–951, May 2003.
- [54] A. Chilingarian *et al.* Correlated measurements of secondary cosmic ray fluxes by the Aragats Space-Environmental Center monitors. Nucl. Instruments Methods Phys. Res. Sect. A Accel. Spectrometers, Detect. Assoc. Equip., Vol. 543, No. 2-3, pp. 483–496, May 2005.
- [55] P. Vogel, J. Engel. Neutrino electromagnetic form factors. Phys. Rev. D, Vol. 39, No. 11, pp. 3378–3383, June 1989.
- [56] T. A. Mueller *et al.* Improved predictions of reactor antineutrino spectra. Phys. Rev. C, Vol. 83, No. 5, p. 054615, May 2011.
- [57] P. Huber. Determination of antineutrino spectra from nuclear reactors. Phys. Rev. C, Vol. 84, No. 2, p. 024617, August 2011.
- [58] IAEA Headquarters. Final Report: Focused Workshop on Antineutrino Detection for safeguards Applications, 2008.
- [59] S. Agostinelli *et al.* Geant4 a simulation toolkit. Nucl. Instruments Methods Phys. Res. Sect. A Accel. Spectrometers, Detect. Assoc. Equip., Vol. 506, No. 3, pp. 250–303, July 2003.
- [60] Goddard Space Flight Center. GRB Coordinates Network.
- [61] Japan Meteorological Agency.
About kaminari nowcast - <http://www.jma.go.jp/jma/kishou/nowcast/toppuu/thunder2-1.html>.
- [62] The National Institute of Standards and Technology. XCOM: Photon Cross Sections Database.
- [63] R. R. Daniel, S. A. Stephens. Cosmic-Ray-Produced Electrons and Gamma Rays in the Atmosphere. Rev. Geophys., Vol. 12, No. 2, pp. 233–258, 1974.
- [64] T. Torii. Study about mechanism of radiation in thunderclouds. doctor thesis, Osaka University, 2003.
- [65] N. Kitagawa. Atomospheric Electricity. 1996.